Lift Estimation from Wind Tunnel Wall Pressure

An experimental approach carried out at the Research & Development department of Econowind

Jasper Tillie



Delft University of Technology

TU Delft

ECONOWIND

Lift Estimation from Wind Tunnel Wall Pressure

An experimental approach carried out at the Research & Development department of Econowind

by

Jasper Tillie

Supervisors TU Delft	Prof. dr. F. Scarano & Dr. A. Daliri
Supervisor Company	G. Zwart
Project Duration:	March 2026 - November 2026
Company:	Econowind
Location:	Zeewolde, Netherlands

Cover Image: The NACA0015 model inside the Econowind wind tunnel.

TU Delft

ECONOWIND

Preface

During my internship at Econowind, prior to starting this thesis, I was working on a completely different project when the wind tunnel in the factory caught my eye. So did one particular man, whom the people on the work floor jokingly referred to as ”the Professor” because of his long white lab coat. Being the aerodynamics engineer that I was, we soon got talking, and one thing led to another. The wind tunnel facility was in need of some additional validation checks, and before I knew it, a graduation topic was on the table: validating the wall-pressure-based lift estimation method used in the Econowind wind tunnel.

And so began a nine-month journey. The project not only taught me how to conduct my own research and carry out my own experiments, but also gave me a taste of working in a dynamic company environment, where things constantly change, people come and go, and objectives are regularly adjusted along the way.

Luckily, I was not on my own throughout this journey, and I want to thank a few people in particular. First, I want to thank Guido for teaching me the ins and outs of operating the wind tunnel. If it were not for him, I would not have gained nearly as many hours of wind tunnel operating experience as I have by now (he built the thing). Also, a special thanks to Abbas for supervising me throughout the project and teaching me to think ambitiously and creatively when tackling problems. Finally, I want to thank Fulvio for the time and effort he put into supervising me, teaching me to think critically and assess the feasibility of each step along the way. Your different approaches complemented each other well and made you a great supervisory duo.

Jasper Tillie
Delft, October 2026

Abstract

Wind-assisted ship propulsion (WASP) systems employ aerodynamic forces to reduce the engine power required for vessel propulsion. At Econowind, wind-tunnel testing is used to evaluate the aerodynamic performance of boundary-layer suction wings, with lift primarily determined through wall pressure measurements (WPM). However, discrepancies between experimental results and numerical predictions have raised questions regarding the accuracy and limitations of this measurement technique.

To investigate these limitations, a baseline experiment was conducted using a NACA0015 airfoil without suction. Lift coefficients obtained from WPM were compared with those derived independently from surface-pressure measurements (SPM) at Reynolds numbers of $Re = 200{,}000$, $Re = 400{,}000$, and $Re = 600{,}000$. Measurements were performed across the pre-stall, stall, and post-stall regimes, including increasing and decreasing angle-of-attack sweeps. Established corrections for finite wall-pressure integration and wind-tunnel interference were applied, and the resulting lift curves were compared with available literature and XFOIL predictions.

WPM and SPM agree more closely in the pre-stall and stall regimes than in the post-stall regime, where WPM consistently overpredicts lift relative to SPM. Nevertheless, WPM captures key features of the lift response, including stall, hysteresis and stall recovery. At $Re = 400{,}000$ and $Re = 600{,}000$, both methods yield lower lift coefficients than several published datasets over part of the pre-stall range. This shared discrepancy suggests that factors other than the WPM method may influence the comparison. Relative to these datasets, WPM provides conservative lift estimates over that part of the pre-stall range.

To investigate the post-stall discrepancies, the measured wall-pressure footprint and the influence of the existing corrections were examined. The shape of the pressure footprint was compared between the pre-stall and post-stall regimes, and alternative empirical extrapolation methods were evaluated. These provided a simpler approach to lift estimation, achieving accuracy comparable to that of the established potential-flow-based corrections in the pre-stall regime.

Further analysis revealed that the measured wall-pressure footprint alone yields lift estimates close to those obtained from SPM in the post-stall regime, whereas the existing corrections and empirical extrapolations generally lead to overprediction. A separated-wake model based on Wu's formulation was subsequently investigated to better understand the downstream pressure distribution. However, the model did not predict a reversal of the differential wall-pressure contribution under the experimental conditions, and no reliable alternative correction could be established.

Overall, these findings demonstrate the potential of WPM for lift estimation under predominantly attached-flow conditions while identifying strongly separated flow as a major limitation of the current approach. Further investigation is required to understand the underlying mechanisms and assess the applicability of WPM to high-lift, suction-controlled configurations.

Contents

Preface i

Abstract ii

Nomenclature viii

I Research and Results 1

1 An introduction to wind-assisted ship propulsion 2
1.1 Origin of wind-assisted ship propulsion . . . 2
1.2 Renewed relevance of wind-assisted ship propulsion . . . 4
1.3 Operation of WASP systems . . . 5
1.4 Current WASP concepts and configurations . . . 8
1.5 Performance assessment of WASP systems . . . 10

2 Econowind's aerodynamic performance assessment methodology 11
2.1 Facility description . . . 11
2.2 Instrumentation . . . 12
2.3 WPM: theoretical basis and known limitations . . . 13
2.4 Obtaining performance parameters . . . 13
2.4.1 Lift coefficient . . . 14
2.4.2 Drag coefficient . . . 16
2.4.3 Suction coefficient . . . 17
2.4.4 Power coefficient . . . 17
2.5 Preliminary validation and discrepancies . . . 18
2.6 Research gap and objectives . . . 18

3 Experimental assessment of wall-pressure-based lift estimation 20
3.1 Experimental objective . . . 20
3.2 Test conditions . . . 20
3.3 Experimental setup . . . 21
3.4 Data reduction . . . 23
3.5 Results . . . 24
3.6 Discussion . . . 28
3.6.1 Common trends in WPM versus SPM . . . 28
3.6.2 Additional observed phenomena . . . 29
3.6.3 Comparison with reference curves . . . 30
3.7 Summary of experimental findings . . . 31

4 Limitations of WPM in separated flow 32
4.1 Motivation and approach . . . 32
4.2 Evolution of the wall-pressure footprint . . . 32
4.3 Empirical extrapolation of the wall-pressure footprint . . . 34
4.4 Physical interpretation of the post-stall discrepancy . . . 36
4.5 Investigation using a separated-wake model . . . 38
4.5.1 Wu wake model . . . 38
4.5.2 Predicted wall-pressure response . . . 39
4.5.3 Comparison with experimental conditions . . . 41
4.5.4 Obtaining lift values using Wu's pressure distributions . . . 42
4.5.5 Model limitations . . . 44

5 Conclusions **46**

6 Recommendations **48**
6.1 Application to suction-controlled bluff-body airfoils 48
6.2 Further investigation of post-stall discrepancies 49

References **50**

II Appendix **53**

A Potential-flow correction **54**

B Wu separated-Wake model **56**

III Literature study **57**

C Fundamentals of wind tunnel testing **58**
C.1 Wind Tunnel Configurations 58
C.2 Main components of a wind tunnel 59
C.3 Flow similarity 61
C.3.1 Governing equations 61
C.3.2 Non-dimensionalization 62
C.4 Wind tunnel wall interference 63

D Instrumentation and measurement techniques **65**
D.1 Force and moment measurements 65
D.2 Velocity measurements 66
D.2.1 Pitot-static tubes 66
D.2.2 Hot-wire anemometry 66
D.2.3 Particle Image Velocimetry 67
D.2.4 Laser Doppler Velocimetry 69
D.3 Pressure measurements 69
D.3.1 Measurement principle and hardware 69
D.3.2 Applications in wind tunnel testing 70
D.4 Flow visualisation 70
D.4.1 Oil flow visualisation 71
D.4.2 Wall-tufts 71
D.4.3 Smoke and dye 71

E Airfoil aerodynamics **72**
E.1 Fundamentals of Airfoil Aerodynamics 72
E.2 Potential Flow and Lift Generation 74
E.3 Boundary layer behaviour 77
E.4 Boundary layer suction 78

List of Figures

1.1 The clipper ship *Three Brothers*, published by Currier & Ives in 1875 [14]. 3
1.2 The *Buckau* with its two Flettner rotors [8]. 3
1.3 The *Alcyone* equipped with two turbosails [42]. 3
1.4 Velocity and angular parameters defining the aerodynamic operating condition of a wing-based WASP system. 6
1.5 Lift-drag polar used to determine the aerodynamic operating point and corresponding propulsive-force component. Modified from [11]. 7
1.6 Overview of current WASP concepts. The freestream direction is indicated by V_∞. The vector R indicates the resultant aerodynamic force acting on the body. 9

2.1 Econowind wind tunnel facility. 12
2.2 Schematic of the suction circuit providing boundary-layer suction and blowing through the model. 12
2.3 Wind-tunnel wall equipped with 16 pressure taps used for lift measurements. 12
2.4 Centralised valve system. 13
2.5 Pitot tube downstream of the model used for drag measurements. 13
2.6 Wind-tunnel wall-pressure measurement setup. Modified from [25]. 15
2.7 Idealised airfoil wake velocity profiles in unbounded flow [31]. The dashed lines denote open control boundaries, not wind-tunnel walls. 16
2.8 Uncorrected and corrected C_l curves for NACA 0018 ($c = 0.165\,\mathrm{m}$, $Re = 500{,}000$) compared to force-balance measurements from [38]. 18

3.1 NACA 0015 model and pressure-tap arrangement in the wind-tunnel test section. 21
3.2 Pressure measurement acquisition chain. 21
3.3 Predicted NACA 0015 surface-pressure envelopes and selected scanner limits at $Re = 200{,}000$. 22
3.4 Predicted NACA 0015 surface-pressure envelopes and selected scanner limits at $Re = 400{,}000$. 22
3.5 Predicted NACA 0015 surface-pressure envelopes and selected scanner limits at $Re = 600{,}000$. 23
3.6 Effect of the successive correction steps on the measured lift curves at $Re = 400{,}000$. . 25
3.7 Measured lift curves and signed differences at $Re = 200{,}000$ [39, 37, 43]. 26
3.8 Measured lift curves and signed differences at $Re = 400{,}000$, first campaign [37, 34]. . . 26
3.9 Measured lift curves and signed differences at $Re = 400{,}000$, second campaign [37, 34]. 27
3.10 Measured lift curves and signed differences at $Re = 600{,}000$ [34, 21]. 27
3.11 RMSE between WPM and SPM across the pre-stall, stall and post-stall regimes. 28
3.12 Differences between WPM and SPM in stall angle and maximum lift coefficient across the four experimental campaigns. 29

4.1 Evolution of the wall-pressure footprint during the increasing-angle sweep at $Re = 200{,}000$. 33
4.2 Wall-pressure footprints before and after stall at $\alpha = 14^\circ$ and $\alpha = 15^\circ$, respectively, for $Re = 200{,}000$. 33
4.3 Empirical extrapolation functions for the pre-stall wall-pressure footprint at $\alpha = 12^\circ$ ($\alpha_{\mathrm{corr}} \approx 11.77^\circ$) and $Re = 200{,}000$. 34
4.4 Empirical extrapolation functions for the post-stall wall-pressure footprint at $\alpha = 20^\circ$ ($\alpha_{\mathrm{corr}} \approx 19.77^\circ$) and $Re = 200{,}000$. 35
4.5 Comparison of lift coefficients obtained using finite WPM integration, potential-flow correction and empirical extrapolation against raw SPM results at $Re = 200{,}000$. The lower panel shows the absolute lift-coefficient difference between each WPM method and SPM. 36

4.6 Schematic division of the differential wall-pressure distribution into the upstream (Region 1), measured (Region 2) and downstream (Region 3) regions. 37
4.7 Schematic representation of a possible downstream reversal of the differential wall-pressure footprint. 38
4.8 Evolution of the differential wall-pressure distribution predicted by Wu's separated-wake model at a constant wake underpressure coefficient of $\sigma_{\mathrm{Wu}} = 0.90$. 40
4.9 Minimum downstream differential wall-pressure coefficient predicted by [44], with SPM-derived experimental conditions overlaid. Negative values indicate pressure reversal. . 40
4.10 Suction-side pressure distribution at $\alpha = 22°$, illustrating the selection of pressure taps used to estimate $C_{p,c}$ and determine σ_{Wu}. 41
4.11 Construction of the hybrid wall-pressure distribution for $Re = 200{,}000$ at $\alpha = 20°$. 43
4.12 Comparison of lift coefficients obtained from SPM, finite WPM, empirical extrapolation and the Wu-based hybrid method for $Re = 200{,}000$. 43
4.13 Sensitivity of the hybrid lift prediction to the applied Wu angle offset for $Re = 200{,}000$. . 44

C.1 Schematic of an open-circuit wind tunnel [18] 58
C.2 TUDelft low turbulence wind tunnel [32] 59
C.3 Potential flow solution of a cylinder with wake [7]. 64

D.1 Balance platform with balance beneath [2] 65
D.2 Pitot-static tube [10] 66
D.3 Hot wire anemometer [36] 67
D.4 Typical PIV setup for a two-component velocity measurement [30]. 68
D.5 Laser Doppler Velocimetry setup for different aperture placements 69
D.6 Setup for surface pressure measurement on a wind tunnel model [9] 70
D.7 Oil-flow visualisation of a laminar separation bubble on an E387 airfoil. Point A indicates laminar separation, and point B indicates reattachment [41]. 71

E.1 Pressure and shear stress acting on an airfoil surface [6]. 72
E.2 Resultant aerodynamic force components acting on an airfoil [6]. 72
E.3 Surface-pressure distributions for a NACA 0012 airfoil at $Re = 30{,}000$. Adapted from [45]. 73
E.4 XFOIL-predicted lift and drag coefficients for a NACA 0015 airfoil at $Re = 50{,}000$. 73
E.5 Elementary flows used in potential-flow theory. 75
E.6 Superposition of uniform flow, doublet flow, and vortex flow to obtain lifting flow over a circular cylinder [12]. 76
E.7 Chord line vortex sheet [6] 76
E.8 Boundary layer propagation over an airfoil [31] 77
E.9 Impact of BLS on boundary layer velocity profile [19] 79
E.10 Effect of suction on stall behaviour of a NACA0012 for different suction lengths [46] . . 79

List of Tables

1.1 Wind-assisted propulsion reward factors based on the ratio of effective wind power to installed propulsion power [17]. 4

3.1 Selected pressure scanner ranges for each measurement region at the investigated Reynolds numbers. 23
3.2 Average relative increase in lift coefficient from the increasing- to decreasing-angle sweep at $\alpha = 11^\circ$ and 12°. 30

4.1 Fit quality and resulting lift correction for the candidate extrapolation functions at pre-stall and post-stall conditions. 35

Nomenclature

Abbreviations

Abbreviation	Definition
BLS	Boundary-layer suction
CCA	Constant-current anemometry
CFD	Computational fluid dynamics
CII	Carbon Intensity Indicator
CTA	Constant-temperature anemometry
EEXI	Energy Efficiency Existing Ship Index
EU ETS	European Union Emissions Trading System
GHG	Greenhouse gas
HWA	Hot-wire anemometry
IMO	International Maritime Organization
LDA	Laser Doppler anemometry
LDV	Laser Doppler velocimetry
MARPOL	International Convention for the Prevention of Pollution from Ships
NACA	National Advisory Committee for Aeronautics
Nd:YAG	Neodymium-doped yttrium aluminium garnet
PIV	Particle image velocimetry
RMSE	Root mean square error
SPM	Surface-pressure measurements
TU Delft	Delft University of Technology
WASP	Wind-assisted ship propulsion
WPM	Wall-pressure measurements

Symbols

Symbol	Definition	Unit
A	Cross-sectional or reference area	[m^2]
a	Speed of sound	[m/s]
a_0	Complex-coordinate offset in Wu's mapping	[m]
b	Active span over which suction is applied	[m]
c	Airfoil chord length	[m]
C	Wind-tunnel test-section cross-sectional area in the solid-blockage correction (Equation 2.7), or generic aerodynamic coefficient in Appendix C	[m^2] or [-]
$\mathcal{C}_{\text{suction}}$	Suction portion of the two-dimensional airfoil contour	[-]
C_A	Axial-force coefficient	[-]
C_D	Three-dimensional drag coefficient	[-]
C_d	Two-dimensional drag coefficient	[-]
C_f	Skin-friction coefficient	[-]
C_L	Three-dimensional lift coefficient	[-]
C_l	Two-dimensional lift coefficient	[-]
C_{l_i}	Airfoil design lift coefficient in the finite-integration correction	[-]

Symbol	Definition	Unit
$C_{l,\mathrm{empty}}$	Empty-tunnel wall-pressure lift contribution	[-]
$C_{l,\mathrm{uncorr}}$	Uncorrected wall-pressure lift coefficient	[-]
$C_{l,\mathrm{wall}}$	Lift coefficient obtained from the measured wall-pressure footprint	[-]
$C_{l,\mathrm{wall}}^{\mathrm{corr}}$	Wall-pressure lift coefficient after finite-integration correction	[-]
$C_{l,\mathrm{SPM}}, C_{l,\mathrm{WPM}}$	Lift coefficients obtained by SPM and WPM, respectively	[-]
C_N	Chord-normal force coefficient	[-]
C_m	Moment coefficient	[-]
C_P	Power coefficient	[-]
C_p	Pressure coefficient	[-]
$C_{p,c}$	Cavity-pressure coefficient	[-]
C_q	Suction coefficient	[-]
C_T	Propulsive-force coefficient	[-]
C_v	Specific heat capacity at constant volume	[J/(kg K)]
c_p	Specific heat capacity at constant pressure	[J/(kg K)]
D'	Drag force per unit span	[N/m]
d_{diff}	Diffraction-limited particle-image diameter	[m]
E	Electrical output voltage in hot-wire anemometry	[V]
E_{th}	Thermal energy of the hot wire	[J]
$\dot{E}$	Energy-transfer rate or power flux	[W]
f	Focal length	[m]
f_D	Doppler frequency	[Hz]
$f\#$	Camera f-number	[-]
$F_{y,\mathrm{wing}}$	Transverse force per unit span exerted by the airfoil on the flow	[N/m]
$F_{y,\mathrm{walls}}$	Transverse pressure force per unit span exerted by the wind-tunnel walls on the flow	[N/m]
Fr	Froude number	[-]
g	Gravitational acceleration	[m/s^2]
H	Boundary-layer shape factor (Appendix E), or convective heat-transfer rate from a hot wire (Appendix D)	[-] or [W]
k	Thermal conductivity	[W/(m K)]
K_1	Solid-blockage correction constant	[-]
K_x	Streamwise stretching factor in the Wu hybrid mapping	[-]
K_y	Pressure-amplitude scaling factor in the Wu hybrid mapping	[-]
l	Characteristic length	[m]
ℓ_{suction}	Arc length of the suction portion of the airfoil contour	[m]
L'	Lift force per unit span	[N/m]
M	Mach number	[-]
M'	Moment per unit span	[N]
M_v	Model volume used in the blockage correction	[m^3]
m	Signed distance from airfoil centre to first wall-pressure tap	[m]
$\dot{m}$	Mass flow rate	[kg/s]
n	Signed distance from airfoil centre to last wall-pressure tap	[m]
$\mathbf{n}$	Outward unit normal vector to a surface	[-]
n_y	Signed transverse component of the outward unit normal vector	[-]

Symbol	Definition	Unit
p	Static pressure	[Pa]
p_0	Total or stagnation pressure	[Pa]
p_{amb}	Ambient pressure	[Pa]
p_c	Pressure in the separated-wake cavity	[Pa]
p_∞	Freestream static pressure	[Pa]
P	Power	[W]
P_{prop}	Installed ship propulsion power	[W]
P_T	Useful aerodynamic propulsive power	[W]
P_{wind}	Effective wind propulsion power	[W]
Pr	Prandtl number	[-]
q_∞	Freestream dynamic pressure	[Pa]
Q	Volumetric flow rate	[m^3/s]
R	Resultant aerodynamic force (Chapter 1), or specific gas constant (Appendix C)	[N] or [J/(kg K)]
Re	Reynolds number	[-]
Re_x	Local Reynolds number	[-]
$Re_{x,\mathrm{crit}}$	Critical local Reynolds number for transition	[-]
r	Radial coordinate in potential-flow solutions	[m]
s	Arc-length coordinate along the airfoil contour	[m]
S	Reference surface area, or Sutherland constant (Appendix C)	[m^2] or [K]
S_{duct}	Suction-duct cross-sectional area	[m^2]
S_{suc}	Suction surface area	[m^2]
T	Temperature, or propulsive thrust force in Chapter 1	[K] or [N]
t	Time	[s]
TI	Turbulence intensity	[-]
U	Flow speed, or dimensionless reference-velocity parameter in Wu's mapping	[m/s] or [-]
U_A	Apparent wind velocity	[m/s]
U_S	Ship velocity	[m/s]
U_T	True wind velocity	[m/s]
U_∞	Freestream velocity	[m/s]
u	Streamwise velocity component	[m/s]
u'	Streamwise velocity fluctuation	[m/s]
$\mathbf{u}$	Local velocity vector in the suction momentum balance	[m/s]
v	Transverse velocity component	[m/s]
v_s	Suction velocity normal to the airfoil surface	[m/s]
$\mathbf{V}$	Velocity vector	[m/s]
V	Flow speed magnitude	[m/s]
V_{duct}	Flow speed in the suction duct	[m/s]
V_∞	Freestream velocity	[m/s]
$\dot{V}$	Total measured volumetric suction flow rate	[m^3/s]
$\dot{V}'$	Volumetric suction flow rate per unit span, $\dot{V}/b$	[m^2/s]
w	Wind-tunnel wall spacing in the WPM correction, or normalised complex velocity in Wu's mapping	[m] or [-]
w_0	Reference complex velocity in Wu's mapping	[-]
W	Electrical heating power in the hot-wire energy balance	[W]
x	Streamwise or chordwise coordinate	[m]
x_{crit}	Boundary-layer transition location	[m]
y	Transverse or wall-normal coordinate	[m]
z	Complex spatial coordinate in Wu's mapping, $z = x + iy$	[m]

Symbol	Definition	Unit
α	Angle of attack	[rad] or [deg]
α_{corr}	Corrected angle of attack	[rad] or [deg]
β_A	Apparent wind angle	[rad] or [deg]
β_S	Sail angle	[rad] or [deg]
β_T	True wind angle	[rad] or [deg]
δ	Boundary-layer thickness	[m]
δ^*	Boundary-layer displacement thickness	[m]
$\Delta\alpha$	Angle-of-attack difference or offset	[rad] or [deg]
$\Delta\alpha_{\mathrm{Wu}}$	Angle-of-attack offset applied in the Wu sensitivity study	[deg]
ΔC_l	Difference between lift-coefficient estimates	[-]
ΔC_l^{sc}	Lift-coefficient correction due to streamline curvature	[-]
$\Delta C_{p,w}$	Differential wall-pressure coefficient	[-]
Δp	Pressure difference	[Pa]
ϵ_{sb}	Solid-blockage correction factor	[-]
η_a	Finite wall-pressure integration correction factor	[-]
η_b	Finite wall-pressure integration correction factor	[-]
η_x	Chordwise finite-integration correction function	[-]
$\gamma(x)$	Chordwise vortex-sheet strength	[m/s]
Γ	Circulation	[m^2/s]
κ	Potential-flow doublet strength	[m^3/s]
λ	Laser wavelength	[m]
Λ	Potential-flow source strength	[m^2/s]
μ	Dynamic viscosity	[Pa s]
μ_{ref}	Reference dynamic viscosity	[Pa s]
ρ	Density	[kg/m^3]
ρ_∞	Freestream density	[kg/m^3]
σ	Streamline-curvature correction factor	[-]
σ_{Wu}	Wake underpressure coefficient in Wu's separated-wake model	[-]
θ	Boundary-layer momentum thickness, or angular co-ordinate in potential flow	[m] or [rad]
τ_w	Wall shear stress	[Pa]
ϕ	Velocity potential	[m^2/s]
ψ	Stream function	[m^2/s]
ω	Angular velocity	[rad/s]

Part I

Research and Results

1

An introduction to wind-assisted ship propulsion

Wind-assisted ship propulsion (WASP) uses aerodynamic forces generated by lifting bodies exposed to the apparent wind experienced by a vessel, thereby reducing the required engine power. Although the underlying aerodynamic principles are similar to those governing lift generation on an aircraft wing, the useful force is not the lift force itself, but the component of the total aerodynamic force acting in the vessel's direction of travel. The main purpose of this chapter is therefore to explain how the propulsive performance of WASP systems depends on the apparent wind direction, aerodynamic operating point, and system orientation.

The chapter begins by describing the historical development of WASP systems in section 1.1, followed by a discussion of their renewed relevance in section 1.2. The aerodynamic operating principles of WASP systems are then introduced in section 1.3, before the different concepts and configurations currently being developed are discussed in section 1.4. Finally, section 1.5 outlines the main approaches used to assess WASP performance, providing the transition to the following chapter, where the wind-tunnel-based performance assessment method employed by Econowind is described.

1.1. Origin of wind-assisted ship propulsion

The earliest member of the WASP family is the conventional sail. Originating approximately 5000 years BC, the basic principle of sail propulsion remained largely unchanged for millennia. During the mid-nineteenth century, sail propulsion reached its peak in the clipper era [28]. These clippers (Figure 1.1), mainly built in the United States and the United Kingdom, formed fleets that operated on long-distance trading routes. Their slender hulls and large sail areas enabled speeds of up to 37 km/h, allowing them to fulfil a valuable niche in fast passenger and cargo transport. In particular, tea transported from China required rapid shipping because of its tendency to deteriorate.



Figure 1.1: The clipper ship *Three Brothers*, published by Currier & Ives in 1875 [14].

During the same period, the Industrial Revolution shifted attention towards engine-driven ships, which gradually took over the shipping market. Engines greatly improved power density and required substantially less operational effort. Engine propulsion also made ships less dependent on weather conditions. In the twentieth century, wind-assisted propulsion entered a new phase with the introduction of novel concepts. In 1925, the first new type of WASP system emerged when Anton Flettner developed his 'Flettner rotor' concept. He demonstrated that the Magnus effect generated by a rotating cylinder could be used for auxiliary ship propulsion by equipping a vessel with two of these systems (Figure 1.2). Another key figure for this innovation phase was the French naval officer, writer, and scientist Jacques Cousteau, who was born in 1910 and later made an important contribution to the development of modern WASP systems. His first operational system, the turbosail, took the form of a vertical boundary-layer suction wing that he initially mounted on one of his sailing ships. The innovative aspect of this design was the use of a large fan at the base of the wing to generate boundary-layer suction. Combined with a movable flap, this allowed the wing to generate lift in both port and starboard directions. He continued his testing in 1985 by introducing a new ship, the *Alcyone* (Figure 1.3). This new floating test setup, carrying two of Cousteau's turbosails, further explored the benefits of wind-assisted propulsion. The concept was patented by the end of 1986. The patent expired in 2004, placing the concept in the public domain.

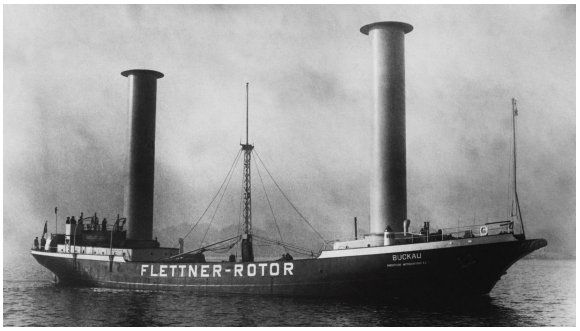


Figure 1.2: The *Buckau* with its two Flettner rotors [8].



Figure 1.3: The *Alcyone* equipped with two turbosails [42].

1.2. Renewed relevance of wind-assisted ship propulsion

Over the past decade, WASP has regained attention as the maritime industry seeks cleaner and more sustainable propulsion methods. In 2021, the European Union introduced the *Fit for 55* legislative package, aimed at reducing net greenhouse gas (GHG) emissions by at least 55% by 2030 compared with 1990 levels. As part of this package, the EU Emissions Trading System (EU ETS), which requires covered sectors to surrender emission allowances, was extended to include maritime transport [13].

Another measure introduced under this package is the *FuelEU Maritime* Regulation, adopted in 2023 and applicable since January 2025. This regulation aims to progressively reduce the GHG intensity of energy used onboard ships, reaching an 80% reduction by 2050 relative to the regulatory reference value [17].

Among its various provisions, the regulation introduces a specific incentive for wind-assisted propulsion systems. The installation of WASP technologies is rewarded based on the ratio of available effective wind propulsion power (P_{wind}) to the ship's installed propulsion power (P_{prop}). As shown in Table 1.1, this ratio determines a reward factor that can reduce the calculated annual average GHG intensity of the energy used onboard by up to 5% for regulatory compliance purposes [17].

Table 1.1: Wind-assisted propulsion reward factors based on the ratio of effective wind power to installed propulsion power [17].

Reward factor (f_{wind})	$P_{\mathrm{wind}}/P_{\mathrm{prop}}$
0.99	0.05
0.97	0.10
0.95	≥ 0.15

Since FuelEU Maritime imposes progressively stricter limits on the annual average GHG intensity of energy used onboard, this reward factor can help ships meet their regulatory requirements and avoid potential financial penalties. Combined with the potential fuel savings offered by wind-assisted propulsion, these incentives encourage the further development and adoption of WASP technologies.

In addition to European legislation, the International Maritime Organization (IMO) has introduced regulations aimed at improving energy efficiency and reducing carbon emissions in international shipping. Since January 2023, two mandatory measures have applied to ships within their respective scope under MARPOL Annex VI [20]:

- **EEXI:** The Energy Efficiency Existing Ship Index evaluates the technical energy efficiency of existing ships relative to an established baseline. The calculated EEXI must not exceed the required value, which depends on ship type and size. This establishes a minimum technical energy efficiency standard for existing ships.
- **CII:** The Carbon Intensity Indicator evaluates a ship's annual operational carbon intensity by relating its CO_2 emissions to its capacity and distance travelled. Based on this indicator, ships receive a rating ranging from A to E, with A representing the highest performance. Ships receiving an E rating for one year or a D rating for three consecutive years must develop a corrective action plan to achieve a rating of C or higher.

Both measures provide additional incentives for adopting WASP technologies, as reducing the required engine power and associated fuel consumption can contribute to improved technical and operational efficiency.

Beyond regulatory incentives, WASP systems offer both economic and environmental benefits through reduced fuel consumption. The achievable savings depend strongly on factors such as system design, operating conditions, vessel type and route. A practical example is the VentoFoil developed by Econowind, discussed in detail in section 1.4. Econowind reports annual fuel savings of up to 15% for this system, while voyage-level reductions may be higher under favourable conditions [15, 16]. These reductions translate into lower operating costs and CO_2 emissions. For example, Econowind reports that one of its customers expects to recover the investment in its VentoFoil installation within approximately four years through fuel savings [15].

The potential benefits become more substantial when considering large-scale adoption. Mason et al. [23] investigated the potential of wind-assisted propulsion across a global fleet of approximately 34,000 ships, using 1.74 billion kilometres of routing data. Their modelled results indicate potential fuel consumption reductions of 6.3–9.4%, corresponding to proportional reductions in fuel expenditure under unchanged fuel prices. Under a scenario of progressive adoption supported by strong policy measures, cumulative CO_2 emissions savings could reach 762 million tonnes by 2050. As an illustrative estimate, assuming these emissions were avoided entirely through reduced heavy fuel oil consumption at a constant price of EUR 600 per tonne, this would correspond to approximately EUR 147 billion in cumulative gross fuel-cost savings. Although the actual financial savings depend on future fuel prices, fuel types and deployment rates, these results illustrate the potential economic and environmental benefits of widespread WASP adoption.

1.3. Operation of WASP systems

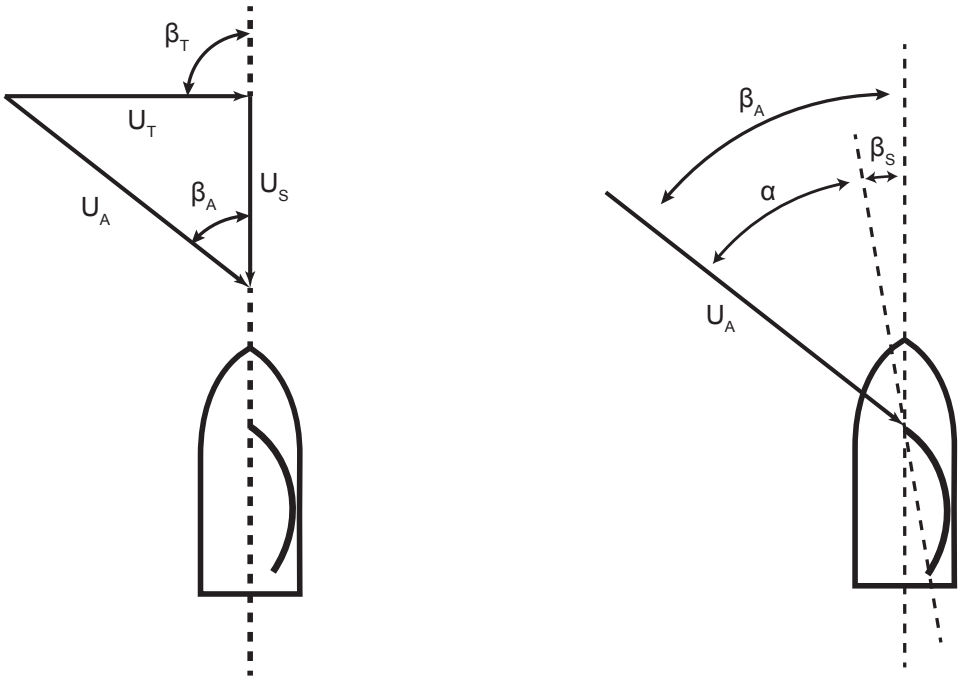
The regulatory incentives and potential economic benefits discussed above have contributed to the renewed interest in wind-assisted ship propulsion. Before introducing the different WASP concepts, it is useful to outline their underlying operating principles. An important distinction between lifting bodies used for aircraft and those used for wind-assisted ship propulsion lies in the force component of interest. For an aircraft, lift is primarily required to counteract the weight of the aircraft. For a WASP system, however, the useful aerodynamic force is the component of the resultant aerodynamic force acting in the ship's direction of travel, since this component contributes directly to propulsion.

Although a wide variety of WASP concepts is currently employed, their operation is governed by the same basic aerodynamic principles. A moving vessel experiences an apparent wind, U_A, defined as the wind velocity relative to the vessel. This apparent wind results from the vector combination of the true wind velocity, U_T, and the velocity induced by the ship's forward motion, U_S, according to Equation 1.1. The resulting velocity relationship is illustrated in Figure 1.4a. The direction of the apparent wind relative to the ship is described by the apparent wind angle, β_A.

$$\mathbf{U}_A = \mathbf{U}_T - \mathbf{U}_S \tag{1.1}$$

For wing-based WASP systems, the main operational parameter controlling the aerodynamic response is the angle of attack. The sail angle, β_S, defines the orientation of the lifting surface relative to the ship, while the apparent wind angle, β_A, defines the incoming flow direction. Their relation to the aerodynamic angle of attack is illustrated in Figure 1.4b. With the sign convention adopted in this figure, the angle of attack is given by Equation 1.2.

$$\alpha = \beta_A - \beta_S \tag{1.2}$$



(a) Vector relationship between true wind, ship velocity, and apparent wind.

(b) Relation between apparent wind angle, sail angle, and aerodynamic angle of attack.

Figure 1.4: Velocity and angular parameters defining the aerodynamic operating condition of a wing-based WASP system.

Changing the sail angle therefore changes the angle of attack and consequently the aerodynamic loading of the lifting body.

For a given geometry, the resultant aerodynamic force generated by the lifting body depends primarily on the angle of attack, Reynolds number, and, where applicable, the applied boundary-layer control. The influence of these parameters on airfoil aerodynamics is discussed further in Appendix E. The aerodynamic resultant force can subsequently be decomposed into lift and drag, where lift acts perpendicular to the apparent wind direction and drag acts parallel to it. Expressing these force components in non-dimensional form results in the corresponding lift and drag coefficients, C_l and C_d.

The aerodynamic behaviour of the system can therefore be represented using a lift-drag polar, as shown in Figure 1.5. Each point on this polar corresponds to a particular aerodynamic operating condition and therefore to a specific resultant aerodynamic force. By varying the sail angle, and consequently the angle of attack according to Equation 1.2, the operating point along the polar can be adjusted.

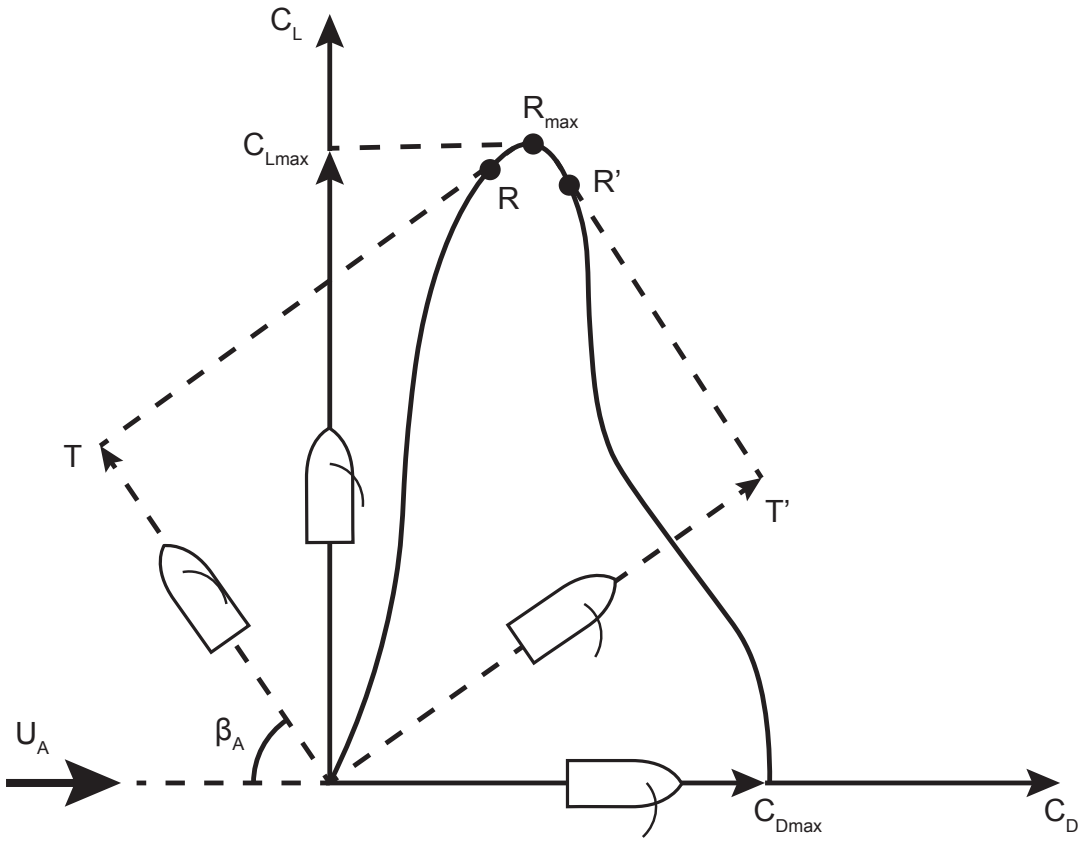


Figure 1.5: Lift-drag polar used to determine the aerodynamic operating point and corresponding propulsive-force component. Modified from [11].

For ship propulsion, the quantity of interest is the component of the resultant aerodynamic force acting in the ship's direction of travel. Using the lift and drag decomposition shown in Figure 1.5, the corresponding propulsive-force coefficient can be expressed according to Equation 1.3.

$$C_T = C_l \sin \beta_A - C_d \cos \beta_A \tag{1.3}$$

For a given apparent wind angle, the operating point can therefore be selected such that the propulsive-force coefficient defined by Equation 1.3 is maximised. Once the corresponding aerodynamic angle of attack is known, the required sail angle follows directly from Equation 1.2. The remaining component of the resultant aerodynamic force acts transverse to the ship's direction of travel and does not contribute directly to propulsion.

The achievable propulsive force consequently depends on the combined aerodynamic response of the system rather than on lift or drag individually. A high lift-to-drag ratio is generally favourable because it reduces the relative contribution of drag to the resultant force. However, the operating point that maximises propulsive force does not necessarily coincide with the maximum value of C_l/C_d. The complete lift-drag polar is therefore required to assess the performance of a WASP system over its operating range. The useful aerodynamic power delivered to the vessel is subsequently determined by the propulsive force and ship velocity according to Equation 1.4.

$$P_T = TU_S \tag{1.4}$$

For rotating-cylinder systems, such as Flettner rotors, the interpretation differs from that of wing-based systems. Due to their rotational symmetry, the aerodynamic loading is not controlled through a sail angle in the same way. Instead, the resultant aerodynamic force depends on the apparent wind conditions and the rotational state of the cylinder. For a fixed apparent wind condition and rotational setting, this

corresponds to a specific aerodynamic operating point. The resultant force can again be decomposed into components parallel and perpendicular to the apparent wind, after which the useful propulsive contribution is obtained by projecting the resultant force onto the ship's direction of travel. Consequently, although the mechanism used to generate the aerodynamic force differs from that of wing-based systems, the final performance assessment is based on the same principle: maximising the component of the resultant aerodynamic force that contributes to ship propulsion.

1.4. Current WASP concepts and configurations

While the underlying principles of thrust generation are similar across WASP systems, the mechanisms used to generate and control aerodynamic forces differ considerably. In the search for the most effective solution, several concepts are currently being developed by the relatively small number of companies active in the renewed field of wind-assisted ship propulsion.

The most widely applied concept currently in operation is based on the Flettner rotor principle, shown in Figure 1.6a. The cylindrical rotor rotates at a constant angular velocity, ω, creating an asymmetry in the surrounding flow field through the Magnus effect. As a result, a lift force is generated perpendicular to the apparent wind direction. This concept is currently employed by companies such as Norsepower, ECO FLETTNER, and Anemoi Marine Technologies.

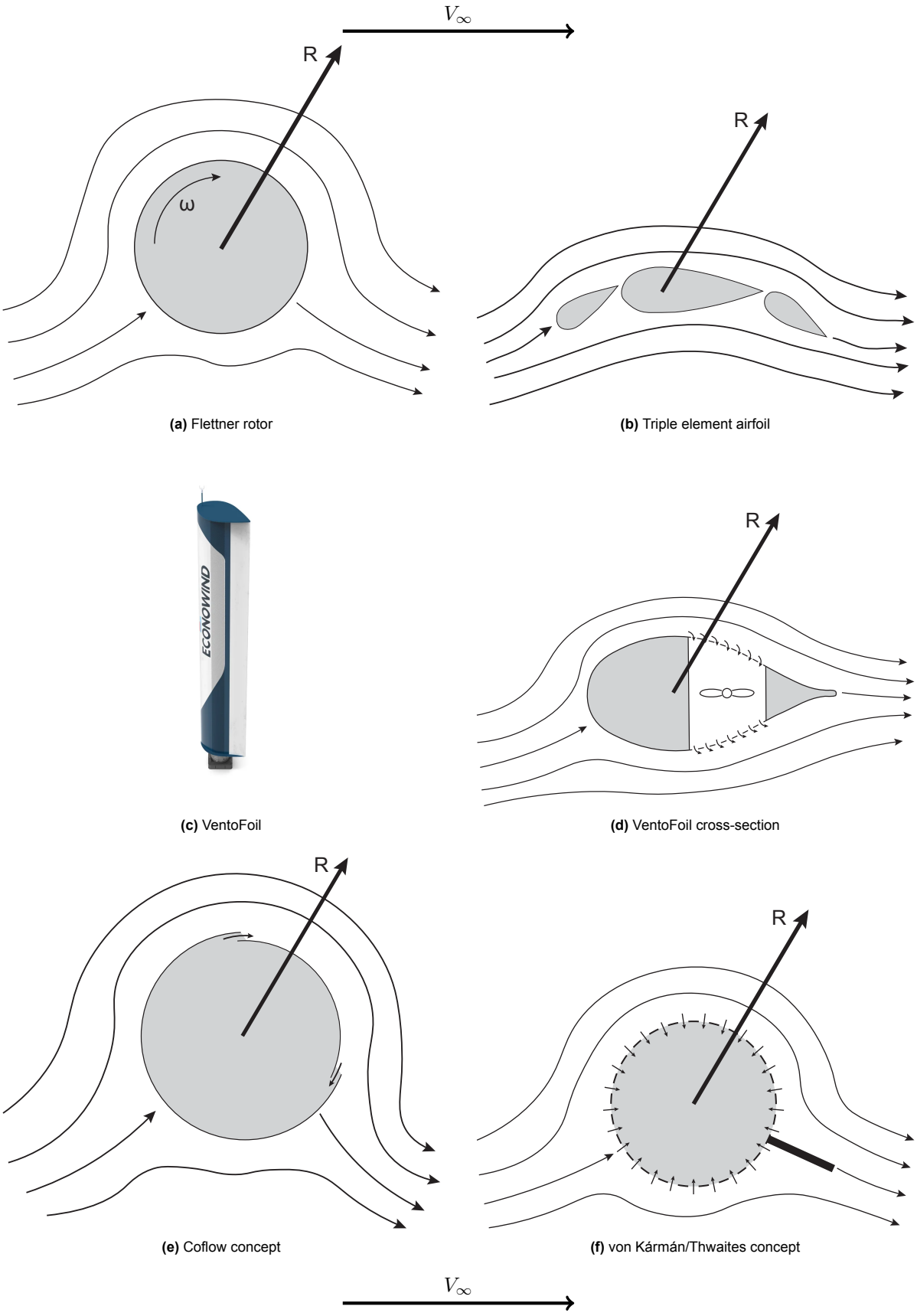
A different approach is taken by BAR Technologies. As shown in Figure 1.6b, their system does not employ active flow control, but instead consists of a three-element wing. The main element, flap and slat can be positioned to form a highly cambered airfoil capable of generating substantial lift. Since no active flow control is applied, these systems generally require a larger surface area than concepts employing suction, blowing, or rotating bodies. A more detailed analysis of airfoil aerodynamics is given in Appendix E, further explaining boundary layer behaviour for airfoils with active flow control.

The wing currently manufactured by Econowind and installed on several ships, the VentoFoil, is depicted in Figure 1.6c. The concept consists of a thick airfoil with a perforated sheet on both sides. Suction is provided by a set of fans distributed along the span. Air is sucked from the leeward side to maintain boundary-layer attachment and expelled from the windward side as illustrated in Figure 1.6d. With one design currently in production, different variations in perforation rate and perforation range are included in Econowind's wind-tunnel test programmes. The practical relevance of this concept is reflected in reported fuel-saving figures. Econowind reports fuel savings of up to 20%, depending on vessel type, route, operating speed, and wind conditions [15, 16]. Although these values are case-dependent, they indicate that suction-based WASP systems can contribute directly to both emission reduction and operational cost savings.

In addition to optimising the design parameters of the current concept, Econowind also investigates new concepts that have shown promising performance in computational fluid dynamics (CFD) analyses. Two principal innovative approaches are currently under consideration.

The Coflow concept depicted in Figure 1.6e originates from the aviation industry and has only recently been introduced to the maritime sector. The underlying co-flow jet principle is protected in patents assigned to Coflow Jet, LLC [47]. The cylindrical shape has two small slits of different sizes for boundary layer control, one for outflow and one for inflow. Its asymmetric geometry presents challenges for application in the maritime sector.

Figure 1.6f shows the von Kármán/Thwaites concept described in [26]. The concept consists of a porous or perforated cylinder employing suction all around its surface, and a simple flap. The study shows that relatively high lift coefficients can be obtained for close to zero drag. Econowind is testing variations of this design in which the perforated region is limited to only part of the cylinder.



(a) Flettner rotor

(b) Triple element airfoil

(c) VentoFoil

(d) VentoFoil cross-section

(e) Coflow concept

(f) von Kármán/Thwaites concept

Figure 1.6: Overview of current WASP concepts. The freestream direction is indicated by V_∞. The vector R indicates the resultant aerodynamic force acting on the body.

1.5. Performance assessment of WASP systems

Although the concepts discussed above differ in geometry and the mechanisms used to generate aerodynamic forces, their performance can be characterised using lift and drag coefficients as earlier described in section 1.3. Accurate determination of these coefficients is therefore essential for evaluating and comparing different concepts. In this thesis, performance assessment refers primarily to the aerodynamic performance of WASP concepts, rather than the complete operational or economic performance of a vessel.

Since full-scale system testing is expensive, logistically complex, and difficult to control, reduced assessment methods are commonly used to determine the aerodynamic performance parameters of WASP systems. In aerodynamic studies, three main approaches can generally be distinguished: theoretical, numerical, and experimental methods. Theoretical methods are mainly applicable to simple or highly idealised problems, where assumptions can be made without significantly affecting the validity of the result. Since WASP concepts often involve complex geometries, separated flow, and, in some cases, active flow-control mechanisms, numerical and experimental methods are of primary importance here.

CFD allows system performance to be modelled using numerical simulations. The governing equations described in subsection C.3.1 are solved for a given geometry and set of boundary conditions, after which lift and drag coefficients can be obtained from the resulting flow field. CFD is particularly useful in the early design stages, as it allows rapid parameter studies over a broad range of geometries and operating conditions. The approach is relatively inexpensive compared with experimental or full-scale testing, making it suitable for exploring concept variations. However, the accuracy of CFD results depends strongly on modelling choices, including turbulence modelling, mesh quality, and boundary conditions. Additional challenges arise for suction-controlled configurations, where the interaction between the external flow, suction system, and internal flow behaviour must be represented accurately. Within Econowind, CFD is therefore mainly used to explore concept variations rather than to determine final design performance in isolation.

Since CFD alone is often insufficient for final design selection, wind tunnel testing provides an additional means of obtaining performance data. It allows the aerodynamic behaviour of a design to be assessed at reduced scale while still capturing relevant geometric features, flow phenomena, and model imperfections. Within Econowind, experimental testing is therefore used to further evaluate concepts that have first been identified as promising through CFD analysis. The focus of this thesis is on this experimental stage of concept assessment. For this reason, the following chapter examines the wind-tunnel methodology used by Econowind and evaluates how effectively it supports the aerodynamic performance assessment of WASP concepts.

2

Econowind's aerodynamic performance assessment methodology

This chapter introduces the experimental methods currently used in the Econowind wind tunnel to assess lift and drag performance and outlines the limitations that motivate the present research. A wide range of measurement techniques can be employed in wind-tunnel testing, an overview of which is provided in Appendix D. This overview was used to establish which alternative measurement approaches could potentially complement or replace the existing methods if additional flow-field information were required during the research.

The present chapter focuses specifically on the methods implemented in the Econowind facility. First, the wind-tunnel facility is described in section 2.1, after which the instrumentation used to obtain the relevant performance parameters is discussed in section 2.2. Since wall-pressure measurements (WPM) form the main focus of the present study, the theoretical basis of WPM and the existing literature on the method are reviewed in section 2.3. The procedure used to reduce the experimental data to aerodynamic performance parameters is then presented in section 2.4, followed by the results of a preliminary validation previously performed by Econowind in section 2.5. Based on these findings, the research gap and objectives of the present study are defined in section 2.6.

2.1. Facility description

The Econowind wind tunnel depicted in Figure 2.1 is an open-circuit wind tunnel with a closed test section measuring $0.45\,\mathrm{m} \times 0.70\,\mathrm{m}$ (height $\times$ width). Airfoil models are mounted vertically, extending from the upper to the lower wall. The wind tunnel has a contraction ratio of 11.1 and is capable of reaching speeds up to 50 m/s, depending on model size. The wind tunnel is driven by a 1.0 m diameter axial fan rated at 18.2 kW. Furthermore, the models can be connected to a smaller 7.5 kW pump to obtain the required boundary-layer suction. Air can both be sucked out of and pumped into the models from the top and bottom sides by this circuit, as depicted in Figure 2.2. When only one of these functions is required for a given model, the circuit can be adapted accordingly. Flow quality is improved by a honeycomb structure and turbulence screen located upstream of the contraction. The instrumentation used is discussed in detail in section 2.2.

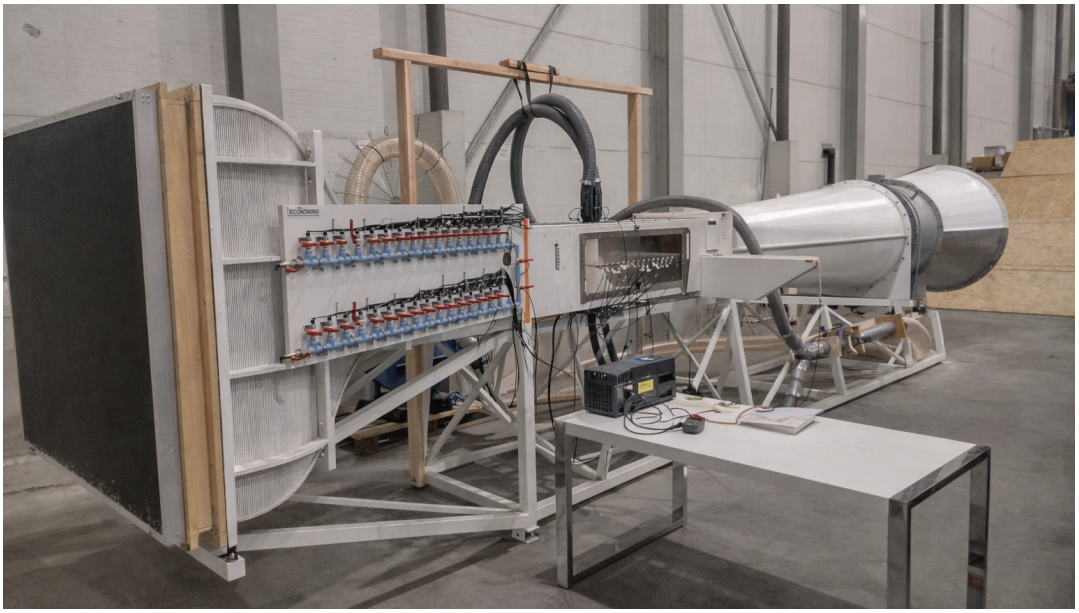


Figure 2.1: Econowind wind tunnel facility.

2.2. Instrumentation

The main purpose of the Econowind wind tunnel is to obtain lift and drag coefficients for two-dimensional studies of high-lift suction wings. The suction circuit imposes physical limitations on measurement equipment. It was therefore decided to equip the facility with wind-tunnel wall-pressure taps, as further discussed in section 2.3. This arrangement prevents the suction mechanism from physically interfering with the performance measurements. Both the upper and lower wind-tunnel walls are equipped with a row of 16 pressure taps (Figure 2.3).

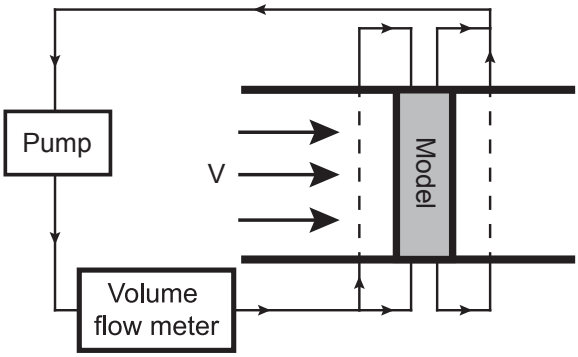


Figure 2.2: Schematic of the suction circuit providing boundary-layer suction and blowing through the model.

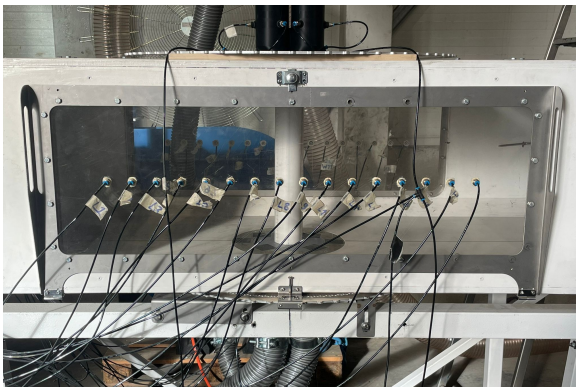


Figure 2.3: Wind-tunnel wall equipped with 16 pressure taps used for lift measurements.

The pressure taps are connected to the centralised valve network depicted in Figure 2.4, allowing a single differential pressure instrument to collect the pressure data. The valves connected to two opposing taps are opened to measure the pressure difference directly, which is subsequently used to derive airfoil lift. To perform drag measurements, the wind tunnel is equipped with a Pitot tube (Figure 2.5) downstream of the model to measure the wake deficit. This Pitot tube is also connected to the valve system for ease of use. Finally, a static-pressure tap upstream of the model provides a feedback signal for controlling the wind-tunnel fan. By maintaining a constant static pressure at this location, the inlet dynamic pressure and flow velocity are kept approximately constant, assuming a constant upstream total pressure.



Figure 2.4: Centralised valve system.



Figure 2.5: Pitot tube downstream of the model used for drag measurements.

Figure 2.2 shows that the suction circuit is equipped with an anemometer to measure the flow rate. Air passes through a fan that provides the suction power and is subsequently expelled at the other end of the model. Pressure taps on both the suction and blowing sides of the model measure the static pressure difference across the model, which is subsequently used to calculate the power coefficient.

2.3. WPM: theoretical basis and known limitations

Since WPM is the main measurement technique used to assess airfoil performance in the Econowind wind tunnel, this section reviews the state of the art in WPM research.

Early wind-tunnel investigations already recognised that the lift generated by a model in a closed test section induces a reaction on the tunnel walls. It was shown that the lift acting on an airfoil could be obtained by integrating the pressure distribution along the lower and upper tunnel walls, with an additional correction to account for the finite integration length [1]. This approach, based on representing the lifting body by an equivalent vortex system and modelling the wind-tunnel walls using an infinite set of image vortices, represents one of the earliest applications of wall-pressure measurements for aerodynamic force estimation.

Later studies further developed this approach into a more complete framework for wind-tunnel correction methods, including corrections for blockage and streamline curvature effects in force measurements [3, 22].

More recent work has renewed interest in wall-pressure measurements as a standalone measurement technique due to their ease of implementation. Earlier theoretical work was extended to describe lift retrieval from wall-pressure measurements in a low-turbulence wind-tunnel environment [4]. A more recent study investigated the sensitivity of the method to a wide range of variables, including port sparsity, chord length, airfoil geometry, surface roughness, and airfoil shape [25]. This study showed that the method can serve as a robust, viable, and inexpensive alternative to conventional measuring techniques in pre-stall conditions.

However, the robustness of the method for high-lift airfoils employing boundary-layer suction has not yet been sufficiently addressed. This represents the operating condition of interest in the present Econowind research project. Lift values obtained through the current wind-tunnel testing program continue to be significantly lower than corresponding values obtained from CFD analyses.

2.4. Obtaining performance parameters

The raw data from the instrumentation are processed to obtain input and performance parameters. The main coefficients of interest are lift, drag, suction and power, which are respectively discussed in subsections 2.4.1 to 2.4.4.

2.4.1. Lift coefficient

The procedure described in this section follows the wall-pressure measurement method and correction approach presented in [1, 25], as adopted by Econowind. The method is based on the conservation of momentum in the transverse, or y, direction within the test section. The flow is assumed to be two-dimensional, steady, and incompressible. Body forces are neglected, while viscous forces are assumed to make a negligible contribution to the transverse momentum balance.

A control volume is considered, bounded by the upper and lower wind-tunnel walls and extending from the first to the last wall-pressure tap. The forces acting on the fluid consist of the pressure forces exerted by the airfoil and the tunnel walls, while transverse momentum is transported through the inlet and outlet of the control volume. For the two-dimensional formulation, the momentum fluxes are integrated over the distance between the upper and lower tunnel walls, denoted by w. With the origin of the y-coordinate at the tunnel centreline, the resulting transverse momentum balance per unit span is given by Equation 2.1.

$$\boxed{F_{y,\mathrm{wing}} + F_{y,\mathrm{walls}} = \int_{-w/2}^{w/2} \rho u_{\mathrm{out}} v_{\mathrm{out}}\, dy - \int_{-w/2}^{w/2} \rho u_{\mathrm{in}} v_{\mathrm{in}}\, dy} \tag{2.1}$$

Here, $F_{y,\mathrm{wing}}$ and $F_{y,\mathrm{walls}}$ represent the transverse forces per unit span exerted by the airfoil and tunnel walls on the fluid, respectively, while u and v denote the streamwise and transverse velocity components. The subscripts in and out identify the inlet and outlet boundaries of the control volume. Under the adopted sign convention, $F_{y,\mathrm{wing}} = -L$, since it represents the force exerted by the wing on the flow, with L denoting the lift force per unit span.

Substituting this relation into Equation 2.1 and non-dimensionalising by the dynamic pressure and chord length yields Equation 2.2, where C_l represents the actual aerodynamic lift coefficient and $C_{l,\mathrm{wall}}$ the contribution obtained from the wall-pressure forces.

$$\boxed{C_l = C_{l,\mathrm{wall}} - \frac{1}{\frac{1}{2}\rho U_\infty^2 c}\left(\int_{-w/2}^{w/2} \rho u_{\mathrm{out}} v_{\mathrm{out}}\, dy - \int_{-w/2}^{w/2} \rho u_{\mathrm{in}} v_{\mathrm{in}}\, dy\right)} \tag{2.2}$$

The experimental setup for obtaining lift is depicted in Figure 2.6. Wind-tunnel wall pressure is measured using 16 taps on each wall and converted into pressure coefficients using Equation 2.3. The finite wall-pressure contribution, $C_{l,\mathrm{wall}}$, is then obtained from Equation 2.4. Here, $C_{l,\mathrm{empty}}$ accounts for the wall-pressure distribution of the empty wind tunnel and is determined using the first term of Equation 2.4.

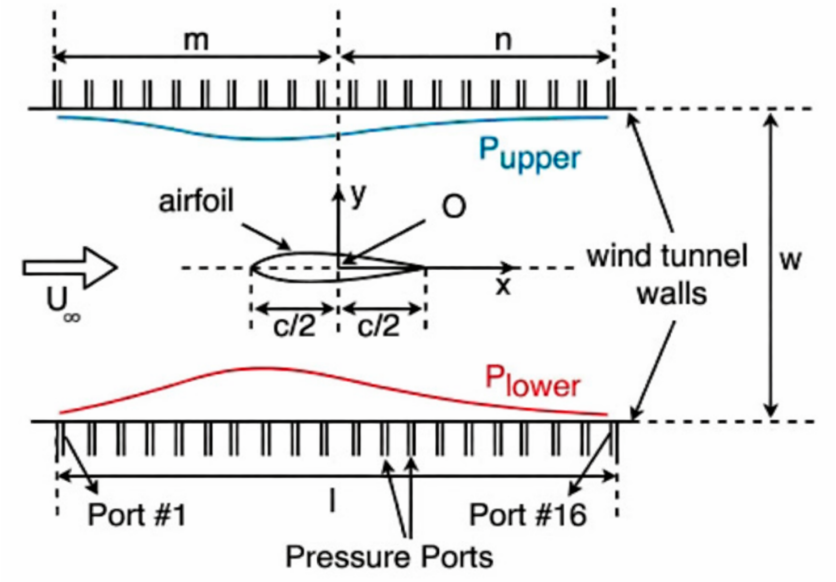


Figure 2.6: Wind-tunnel wall-pressure measurement setup. Modified from [25].

$$C_p = \frac{p - p_\infty}{\frac{1}{2}\rho U_\infty^2} \tag{2.3}$$

$$C_{l,\text{wall}} = \int_m^n \left(C_{p,\text{wall}}^{\text{lower}} - C_{p,\text{wall}}^{\text{upper}} \right) \frac{dx}{c} - C_{l,\text{empty}} \tag{2.4}$$

Having obtained $C_{l,\text{wall}}$ from the measured wall-pressure distribution, the transverse momentum transport through the inlet and outlet of the control volume remains unaccounted for. As shown in Equation 2.2, this contribution must be considered to recover the aerodynamic lift coefficient. Since the transverse velocity field is not measured, the correction approach presented in [1, 25] is employed. This approach uses potential-flow theory to estimate the contribution associated with the finite measurement region through two correction factors, η_a and η_b.

The resulting potential-flow-corrected lift estimate, $C_{l,\text{wall}}^{\text{corr}}$, is obtained from Equation 2.5, where C_{l_i} represents the design lift coefficient of the airfoil. The correction factors η_a and η_b depend on the wind-tunnel geometry and the position of the airfoil relative to the pressure array. Their calculation is provided in Appendix A. When η_a and η_b are approximately equal, the second term becomes negligible, yielding the simplified expression in Equation 2.6. Consequently, the design lift coefficient is no longer required.

$$C_{l,\text{wall}}^{\text{corr}} = \frac{C_{l,\text{wall}}}{\eta_a} - C_{l_i} \left(\frac{\eta_a}{\eta_b} - 1 \right) \tag{2.5}$$

$$C_{l,\text{wall}}^{\text{corr}} = \frac{C_{l,\text{wall}}}{\eta_a} \tag{2.6}$$

The correction can also be interpreted in terms of the wall-pressure footprint. The pressure disturbance induced by an airfoil extends beyond the finite measurement region, meaning that part of the wall-pressure contribution is not captured by the pressure array. Extending the control volume sufficiently far upstream and downstream, where the net transverse momentum flux becomes negligible, would incorporate these previously unmeasured pressure contributions into the wall-pressure integration.

The potential-flow correction can therefore be interpreted either as an estimate of the missing wall-pressure contribution or, equivalently within the assumed flow model, as accounting for the net transverse momentum transport across the boundaries of the finite control volume.

After correcting for the finite wall-pressure footprint, corrections for the influence of the wind-tunnel walls are considered. The model restricts the flow through part of the wind-tunnel cross-section, causing the flow to accelerate. This effect is accounted for by the solid-blockage correction in Equation 2.7, where M_v denotes the model volume within the test section, C the wind-tunnel cross-sectional area, and K_1 a coefficient accounting for the model geometry. A value of $K_1 = 0.52$ is used for models spanning the entire wind-tunnel height.

$$\epsilon_{sb} = \frac{K_1 M_v}{C^{3/2}} \tag{2.7}$$

Furthermore, the walls restrict transverse flow, increasing the effective camber of the airfoil and consequently the lift relative to unbounded-flow conditions. This streamline-curvature effect is accounted for by Equation 2.8 and Equation 2.9, where w is the separation between the upper and lower wind-tunnel walls.

$$\Delta C_l^{sc} = \sigma C_l \tag{2.8}$$

$$\sigma = \left(\frac{\pi^2}{48}\right)\left(\frac{c}{w}\right)^2 \tag{2.9}$$

Accounting for solid blockage and streamline curvature simultaneously, the final lift coefficient estimated from wall-pressure measurements, $C_{l,\mathrm{WPM}}$, is obtained from Equation 2.10.

$$\boxed{C_{l,\mathrm{WPM}} = C_{l,\mathrm{wall}}^{\mathrm{corr}}\left[1 - \sigma - 2\epsilon_{sb}\right]} \tag{2.10}$$

2.4.2. Drag coefficient

The drag coefficient is determined using the wake momentum-deficit approach described by [31]. For idealised, two-dimensional unbounded flow, the drag force per unit span is expressed in terms of the streamwise velocity deficit according to Equation 2.11. The corresponding velocity profiles are shown in Figure 2.7.

$$D' = \rho \int_{-\infty}^{\infty} u\left(U_\infty - u\right)\, dy \tag{2.11}$$

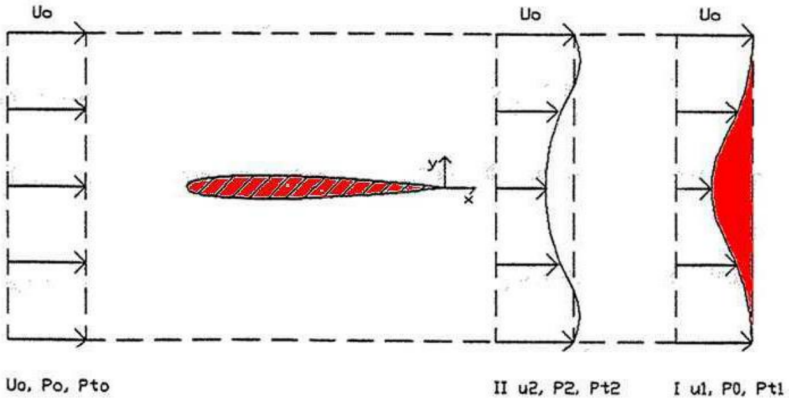


Figure 2.7: Idealised airfoil wake velocity profiles in unbounded flow [31]. The dashed lines denote open control boundaries, not wind-tunnel walls.

To apply this approach in the wind tunnel, the control volume extends across the airfoil wake but excludes the tunnel-wall boundary layers. The tunnel walls therefore do not exert a direct shear force on

the fluid within the control volume. The streamwise velocity along the upper and lower control boundaries is assumed to be close to U_∞, so the momentum carried by flow crossing these boundaries is accounted for through continuity. If shear on the control boundaries is negligible and the static pressure at the wake survey plane has recovered to the upstream value, Equation 2.11 can be applied approximately by integrating across the wake rather than the full tunnel height.

In the present setup, a Pitot tube traverses the wake downstream of the model, measuring the local total pressure relative to ambient pressure. Since the upstream total pressure is also obtained relative to ambient, subtracting these measurements directly yields the total-pressure deficit across the wake. Assuming that the flow at the survey plane is predominantly streamwise and that the static pressure has recovered to the freestream value, this deficit is given by

$$p_{\infty,\mathrm{total}} - p_{\mathrm{wake,total}} = \frac{1}{2}\rho\left(U_\infty + u\right)\left(U_\infty - u\right) \approx \rho u\left(U_\infty - u\right). \tag{2.12}$$

The approximation follows from taking $(U_\infty + u)/2 \approx u$, which is valid for a small velocity deficit relative to U_∞. Integrating this deficit and normalising by the freestream dynamic pressure and chord length provides an approximation of the drag coefficient, as expressed in Equation 2.13.

$$C_d \approx \frac{1}{cq_\infty}\int_{\mathrm{wake}} \left(p_{\infty,\mathrm{total}} - p_{\mathrm{wake,total}}\right)\, dy \tag{2.13}$$

No correction factors are currently applied to the drag coefficient, as drag is of secondary importance compared with lift in the present study.

2.4.3. Suction coefficient

The amount of air extracted through the wing must also be expressed using an appropriate non-dimensional parameter. The suction level is therefore characterised by the suction coefficient, defined in Equation 2.14:

$$C_q = \frac{Q}{U_\infty S} \tag{2.14}$$

where Q is the volumetric flow rate through the suction surface, U_∞ is the freestream velocity and S is the suction surface area. The suction coefficient thus represents the ratio of the volume flow rate extracted through the model to the freestream volume flow rate through the corresponding reference area. An anemometer integrated into the suction circuit measures the flow speed, which is used to calculate the volumetric flow rate according to Equation 2.15.

$$Q = V_{duct} S_{duct} \tag{2.15}$$

2.4.4. Power coefficient

The final non-dimensional parameter used to characterise the operating conditions is the power coefficient. It is defined as the ratio between the hydraulic power required by the system and the available aerodynamic power in the freestream, as given in Equation 2.16.

$$C_P = \frac{P}{\frac{1}{2}\rho U_\infty^3 S} \tag{2.16}$$

The power coefficient is particularly important when assessing the overall efficiency of a suction system. An increase in suction power is only beneficial if it produces a sufficiently large aerodynamic improvement. A useful performance metric is therefore the ratio C_l/C_P, which relates the lift coefficient to the power coefficient. To calculate the hydraulic power, the static pressure difference between the flow entering and exiting the model is measured. The hydraulic power is then obtained from Equation 2.17.

$$P = \Delta p Q \tag{2.17}$$

2.5. Preliminary validation and discrepancies

Using the approach described in subsection 2.4.1, the results of [25] were reproduced, supporting the interpretation of the method. A NACA 0018 airfoil was then tested in the Econowind wind tunnel to further validate the experimental setup and correction factors. The results are presented in Figure 2.8.

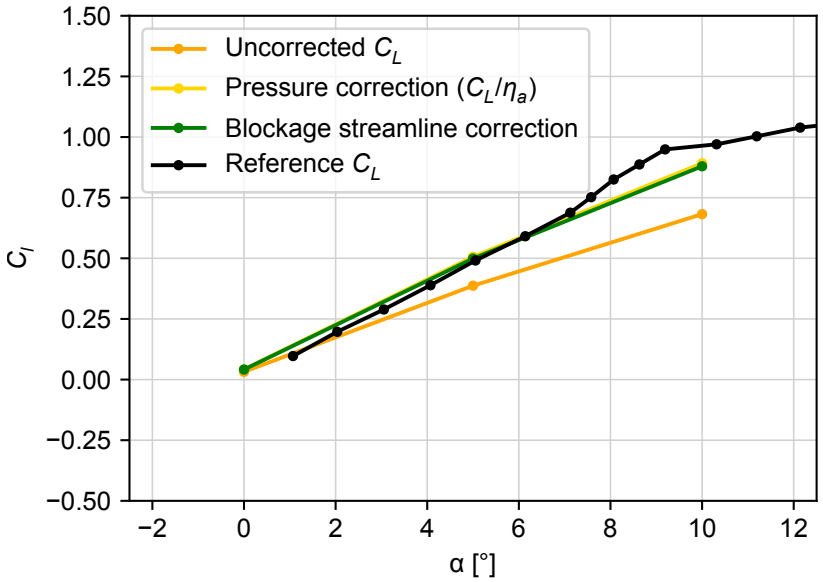


Figure 2.8: Uncorrected and corrected C_l curves for NACA 0018 ($c = 0.165\,\mathrm{m}$, $Re = 500{,}000$) compared to force-balance measurements from [38].

It should first be noted that the validation test consists of only three test points. It is therefore premature to draw firm conclusions from these results, and a more detailed validation of WPM is required. This validation forms the basis of this research and is discussed in chapter 3.

Nevertheless, several trends can be observed from the figure. The final corrected WPM values agree well with the reference results in the pre-stall region. However, a noticeable deviation appears as the angle of attack approaches stall. This discrepancy is likely not caused solely by an increase in blockage magnitude, but rather by the growing nonlinearity of the flow. At higher angles of attack, flow separation and wake thickening become significant, violating the linear and attached-flow assumptions underlying the WPM correction.

The preliminary validation, based on only three measurement points, provided sufficient confidence for Econowind to proceed with the wind-tunnel test campaign but was too limited to establish the accuracy of the method across the full aerodynamic range. Subsequent measurements repeatedly showed lift coefficients that were substantially lower than corresponding CFD predictions for several investigated designs. Since the underlying data are commercially confidential, these discrepancies are not presented quantitatively in this thesis. Although the observed differences do not by themselves indicate whether their origin lies in the numerical or experimental methodology, they provide additional motivation to independently assess the reliability of the wind-tunnel measurement approach.

2.6. Research gap and objectives

The preceding sections identify an important limitation in the current understanding of the Econowind wind-tunnel assessment method. Section 2.3 showed that existing WPM studies have demonstrated accurate lift estimation for conventional airfoils, but have not sufficiently addressed the method's performance for high-lift airfoils employing boundary-layer suction. In addition, section 2.5 showed that the preliminary validation performed at Econowind was based on only a limited number of measurement points, while discrepancies remain between CFD predictions and wind-tunnel measurements for current Econowind designs. Together, these observations indicate that the reliability of WPM-based lift

estimation in the Econowind wind tunnel requires further investigation.

The aim of this study is consequently to investigate the limitations of wall-pressure-based lift estimation in the Econowind wind tunnel and to identify the aerodynamic conditions under which the current method begins to lose accuracy.

The main objectives of this study are:

- Investigate the theoretical assumptions underlying the WPM method and the correction procedure currently applied in the Econowind wind tunnel.
- Perform a controlled experiment on a non-suction airfoil in which lift obtained from WPM can be compared directly with independently obtained surface-pressure measurements (SPM).
- Assess the accuracy of WPM across the pre-stall, stall, and post-stall aerodynamic regimes and determine how its performance varies with Reynolds number.
- Investigate the origin of discrepancies between WPM and SPM, with particular attention to the behaviour of the wall-pressure footprint and the limitations of the existing potential-flow-based correction.

3

Experimental assessment of wall-pressure-based lift estimation

To obtain a better understanding of the principles and corrections underlying the WPM method, this chapter presents a baseline experiment on a NACA 0015 airfoil without suction. The experiment is used to validate the WPM approach, including the established correction factors, under conventional airfoil conditions before considering more complex configurations. First, the experimental objective is outlined in section 3.1, followed by an overview of the test conditions in section 3.2. Section 3.3 describes the experimental setup, after which section 3.4 introduces the data-reduction method applied to the SPM measurements. In section 3.5, the lift curves obtained using both methods are presented together with the reference datasets used for comparison. The results are subsequently discussed in section 3.6, focusing on the agreement between WPM and SPM across aerodynamic regimes, additional observed phenomena and comparison with published lift curves.

3.1. Experimental objective

The objective of this experiment is to compare lift estimates obtained from wall-pressure measurements with those obtained from surface-pressure measurements on the model across the full aerodynamic range, including stall and stall-recovery behaviour. The sensitivity of the WPM method to Reynolds number is also investigated, while the experiment serves as a baseline case for evaluating both measurement approaches against available literature data.

The NACA 0015 airfoil was selected because it provides a simple and well-documented geometry, allowing the comparison to be performed in a relatively low-lift regime without the use of active flow control. The results may provide further insight into the behaviour of the measurement technique for slender lifting bodies operating at relatively low lift, as well as for slender airfoils under stalled conditions, where the flow increasingly exhibits bluff-body-like characteristics. In this way, the experiment provides a useful bridge between conventional airfoil measurements and the more strongly separated-flow conditions expected for bluff lifting bodies. The results may also inform the experimental approach required for future measurements on bluff bodies employing suction.

3.2. Test conditions

To characterise the WPM approach, both WPM and SPM measurements are obtained at Reynolds numbers of $Re = 200{,}000$, $Re = 400{,}000$, and $Re = 600{,}000$. For the $Re = 400{,}000$ campaign, the angle of attack is varied from -24° to 24°, covering the pre-stall, stall, and post-stall regimes for both positive and negative angles of attack. This range also allows the symmetry of the experimental response to be assessed. The campaign is repeated to evaluate the repeatability of the measurements. For $Re = 200{,}000$ and $Re = 600{,}000$, the measurements are limited to positive angles of attack, ranging from 0° to 24°.

The approximately linear portion of the lift curve is tested using increments of 2°, whereas the stall region is sampled in 1° increments to capture the onset and development of stall in greater detail. Measurements in the stall region are performed for both increasing and decreasing angles of attack, allowing both stall-onset and stall-recovery behaviour to be investigated.

3.3. Experimental setup

The experimental setup consists of a NACA 0015 airfoil mounted vertically between the lower and upper wind-tunnel walls. The arrangement of the wind-tunnel wall-pressure taps was previously described in subsection 2.4.1. The model is equipped with 64 surface-pressure taps, with 32 taps on each side arranged in diagonal arrays. This arrangement staggers the taps in the streamwise direction, reducing the likelihood that a measurement is influenced by local flow disturbances generated by an upstream tap. The locations of the model surface-pressure taps and the wind-tunnel wall-pressure taps are shown in Figure 3.1.

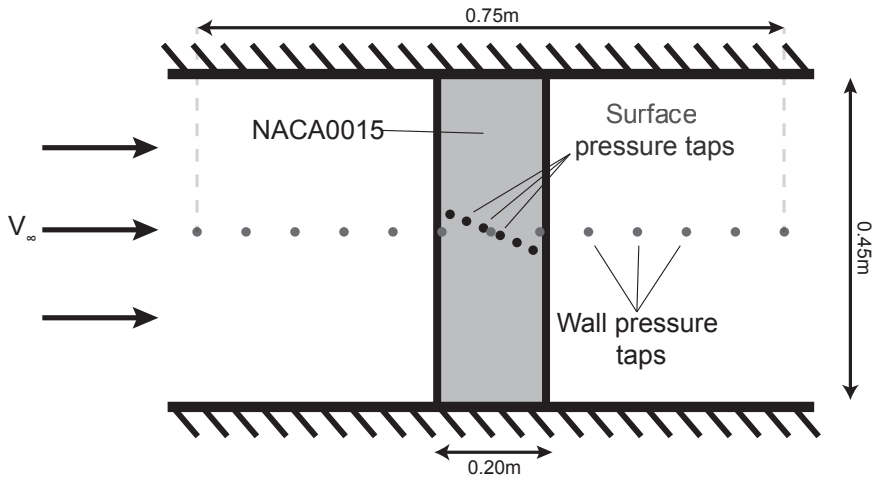


Figure 3.1: NACA 0015 model and pressure-tap arrangement in the wind-tunnel test section.

The 64 model pressure taps are connected via tubing to four pressure scanners, each containing 16 channels. Within each scanner, a pressure transducer measures the deflection of a diaphragm caused by the pressure difference between the connected tap and the reference pressure, which is ambient pressure in the present setup. This pressure difference is converted into an analogue voltage signal and transmitted to the data acquisition unit.

The data acquisition system samples the analogue signals at a specified frequency and returns a sequence of digital values for each channel to the laptop. The specified pressure range corresponding to each transducer is then applied to convert these digital values into pressure measurements. The correspondence between each pressure tap and scanner channel is recorded accurately, as this mapping is required during the final data reduction. The complete measurement setup is shown in Figure 3.2.

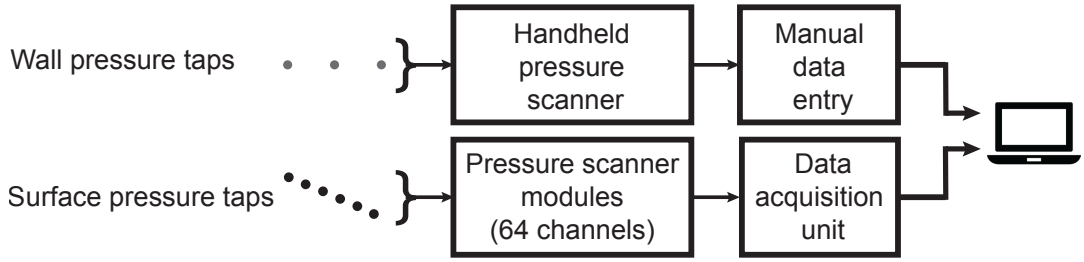


Figure 3.2: Pressure measurement acquisition chain.

Selecting suitable pressure ranges for the pressure scanners is important, as a range that is too small can lead to saturation or potentially damage the scanner, whereas a range that is too large reduces measurement resolution and increases relative uncertainty. To select suitable pressure transducers for the model surface-pressure measurements, a preliminary pressure analysis was performed using XFOIL. Figures 3.3 to 3.5 show only the limiting pressures from the predicted distributions. At each chordwise location, the minimum pressure on the suction side and the maximum pressure on the pressure side were taken across the simulated angles of attack from $0°$ to $24°$. These envelopes are evaluated pointwise and therefore do not represent distributions at a single angle of attack. Red lines show the predicted pressure envelopes and black lines indicate the negative full-scale limits of the selected scanners. Solid and dotted lines represent the suction and pressure sides, respectively.

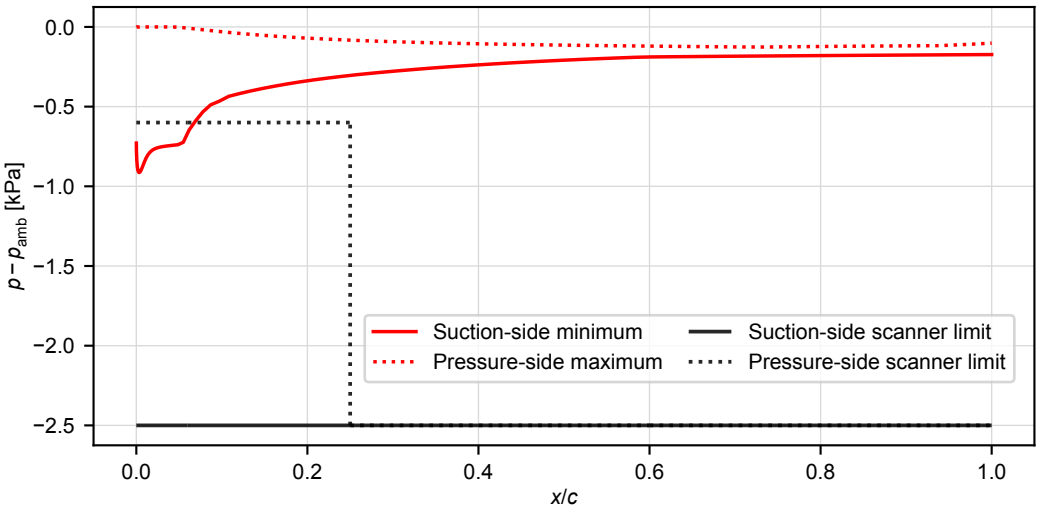


Figure 3.3: Predicted NACA 0015 surface-pressure envelopes and selected scanner limits at $Re = 200{,}000$.

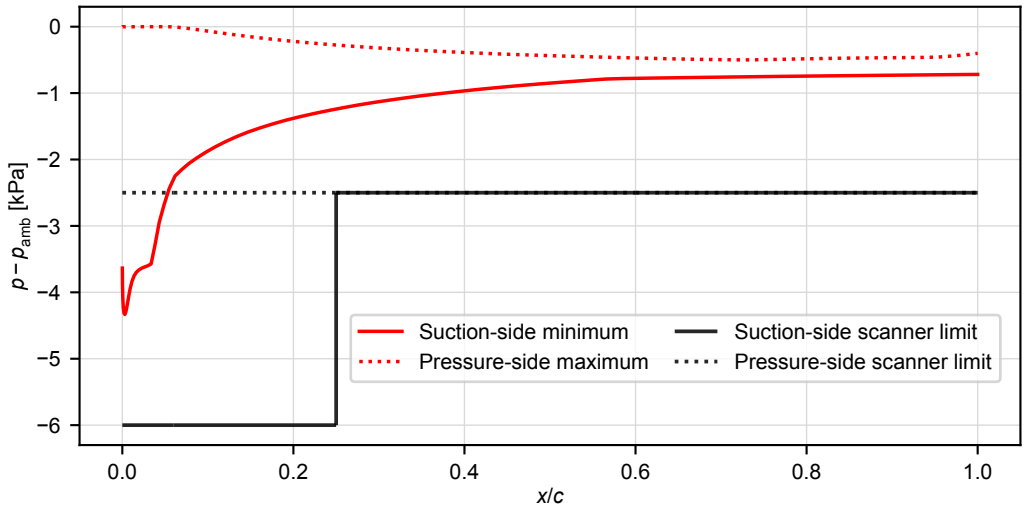


Figure 3.4: Predicted NACA 0015 surface-pressure envelopes and selected scanner limits at $Re = 400{,}000$.

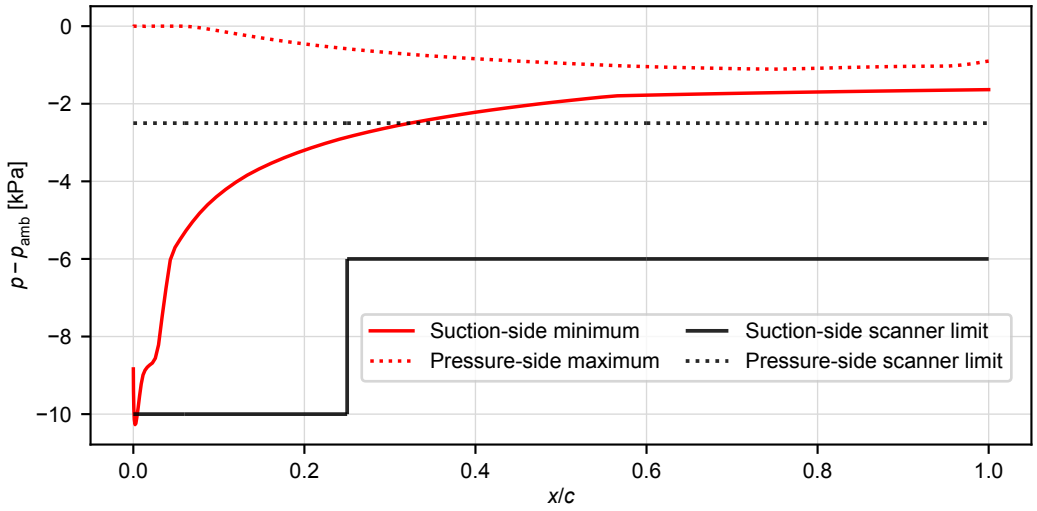


Figure 3.5: Predicted NACA 0015 surface-pressure envelopes and selected scanner limits at $Re = 600{,}000$.

Based on the predicted pressure distributions, a different scanner configuration was selected for each Reynolds number. The suction and pressure sides were each divided into leading- and trailing-edge regions to accommodate the differences in expected pressure magnitude. The resulting scanner configurations are summarised in Table 3.1. The total required scanner set consists of one 10 kPa scanner, one 6 kPa scanner, three 2.5 kPa scanners, and one 600 Pa scanner. The selected configurations provide a compromise between sufficient measurement range and measurement resolution.

Table 3.1: Selected pressure scanner ranges for each measurement region at the investigated Reynolds numbers.

Measurement region	$Re = 200{,}000$	$Re = 400{,}000$	$Re = 600{,}000$
Suction side, leading edge	2.5 kPa	6 kPa	10 kPa
Suction side, trailing edge	2.5 kPa	2.5 kPa	6 kPa
Pressure side, leading edge	0.6 kPa	2.5 kPa	2.5 kPa
Pressure side, trailing edge	2.5 kPa	2.5 kPa	2.5 kPa

3.4. Data reduction

The data reduction approach adopted to obtain lift values using WPM has already been described in subsection 2.4.1. In the present experiment, the raw wall-pressure measurements are converted to uncorrected lift values using the same procedure.

The data reduction procedure for SPM has not yet been discussed. It should first be noted that SPM provides a pressure-derived estimate of lift and is therefore subject to its own assumptions and measurement uncertainties. The raw pressure data from the 64 surface-pressure taps are converted to pressure coefficients following Equation D.8. Together with the local surface orientation, these coefficients can be used to determine the aerodynamic force acting on the airfoil. For an infinitesimal surface element ds, as illustrated in Figure E.1, the differential pressure-force coefficient is given by Equation 3.1,

$$d\mathbf{C}_R = -C_p \mathbf{n} \frac{ds}{c}, \tag{3.1}$$

where $\mathbf{n}$ denotes the outward unit normal vector to the airfoil surface.

When only the force component normal to the chord is considered, the local surface orientation does not need to be evaluated explicitly. The projection of the surface element onto the chordwise direction gives $n_y ds = \pm dx$, with opposite signs for the upper and lower surfaces. Consequently, the contributions from

paired upper- and lower-surface pressure measurements can be combined directly. Integration along the chord then gives the normal-force coefficient,

$$C_N = \int_0^c \left(C_{p,\text{lower}} - C_{p,\text{upper}}\right) \frac{dx}{c}. \tag{3.2}$$

This coefficient represents the pressure contribution to the force normal to the chord line. The corresponding lift coefficient can be approximated from C_N by accounting for the angle of attack, while neglecting the axial pressure force and the contribution of skin friction, as described by Equation 3.3. Here, C_A denotes the axial-force coefficient. This approximation is acceptable here because the pressure contribution dominates the lift force, whereas skin-friction effects mainly affect the drag component.

$$C_l = C_N \cos\alpha - C_A \sin\alpha \approx C_N \cos\alpha \tag{3.3}$$

3.5. Results

Before the measured lift curves can be compared with the reference data, the WPM and SPM results require several corrections to account for experimental and wind-tunnel effects. First, a small horizontal correction was applied to both the WPM and SPM data to account for asymmetry in the wind-tunnel setup and model alignment. This correction was determined from the approximately linear region of the SPM data from both $Re = 400{,}000$ tests. A linear regression was fitted to these data, from which the zero-lift angle was determined. The resulting offset from $\alpha = 0^\circ$ was subsequently applied as a common horizontal shift to all measurements.

After this correction, the WPM results still exhibited a non-zero lift coefficient at the corrected zero-lift angle. Since a symmetric NACA 0015 airfoil is expected to produce approximately zero lift at zero effective incidence, this residual was treated as a systematic measurement offset. A separate vertical correction was therefore determined from the WPM linear regression and applied such that the fitted WPM lift coefficient equals zero at $\alpha_{\text{corr}} = 0^\circ$. No corresponding vertical correction was applied to the SPM data, as these serve as the independent reference measurements.

To account for the finite wall-pressure integration range, the potential-flow-based correction described in Equation 2.6 was applied to the WPM lift values. Finally, the wind-tunnel interference corrections were applied following Equation 2.10. The successive effect of these correction steps on the lift curves is illustrated in Figure 3.6.

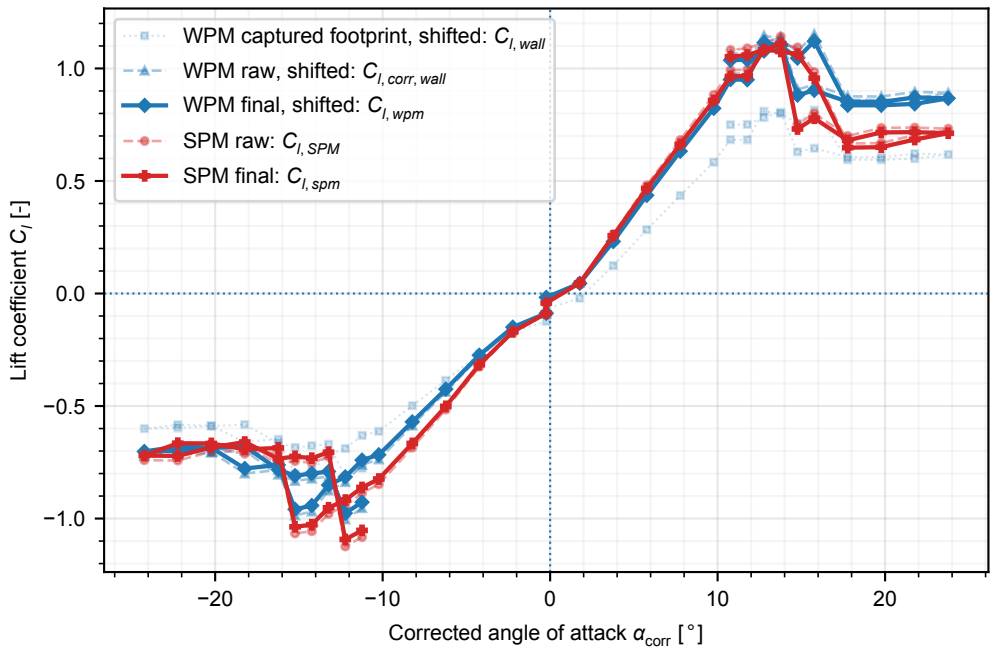


Figure 3.6: Effect of the successive correction steps on the measured lift curves at $Re = 400{,}000$.

After applying the full correction procedure, the results of the four tests conducted at $Re = 200{,}000$, $400{,}000$, and $600{,}000$ are presented in Figure 3.7 to Figure 3.10. The upper panel of each figure shows the lift curves obtained using WPM and SPM, together with reference data from the literature and predictions obtained using XFOIL. The literature datasets were selected based on similarity in Reynolds number.

The lower panel shows the signed difference between the WPM and SPM results. Where suitable literature data are available at a comparable Reynolds number, the signed difference between WPM and the corresponding reference curve is also shown.

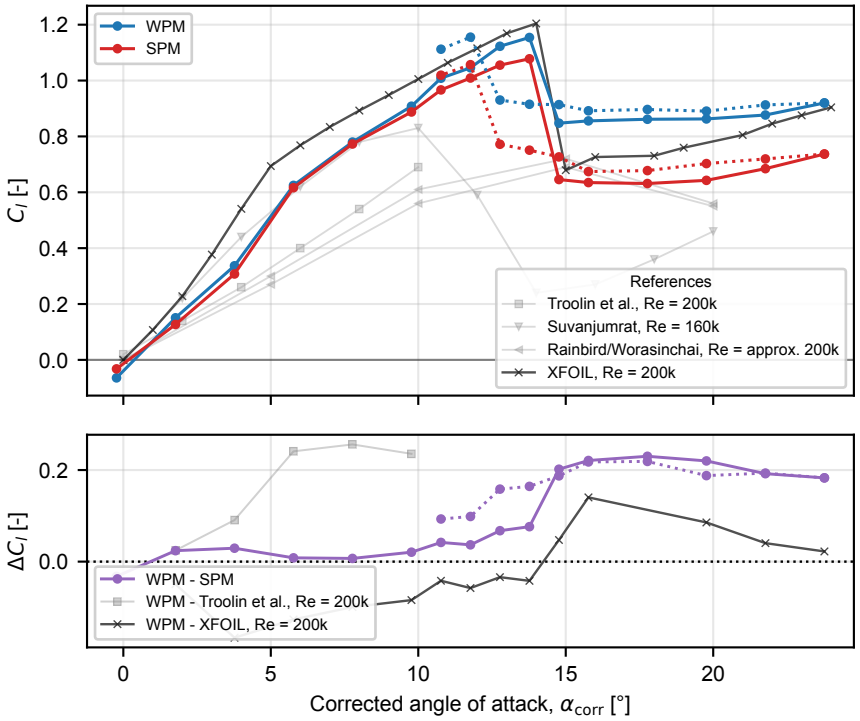


Figure 3.7: Measured lift curves and signed differences at $Re = 200{,}000$ [39, 37, 43].

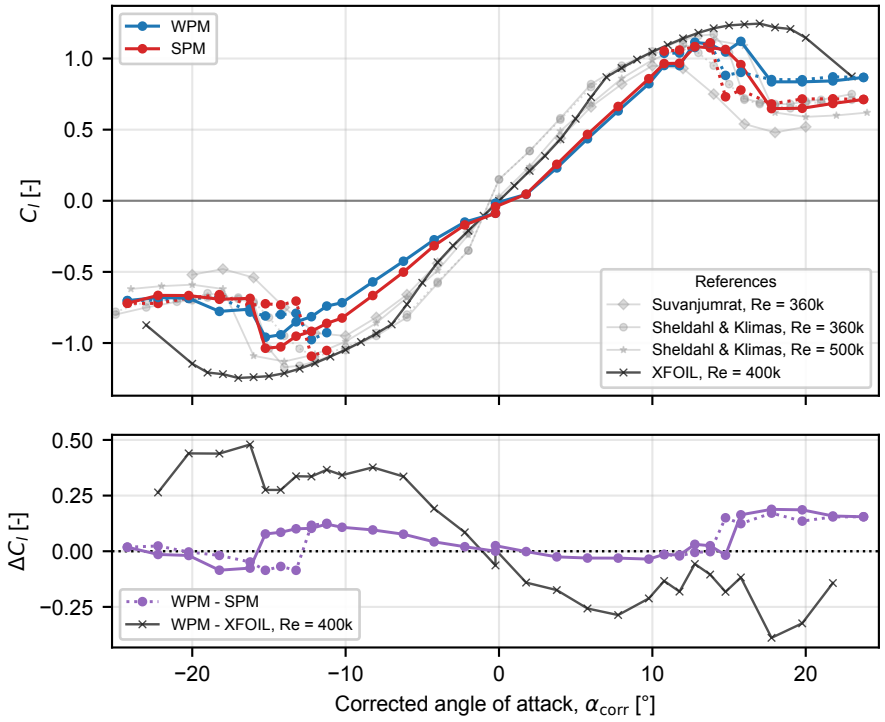


Figure 3.8: Measured lift curves and signed differences at $Re = 400{,}000$, first campaign [37, 34].

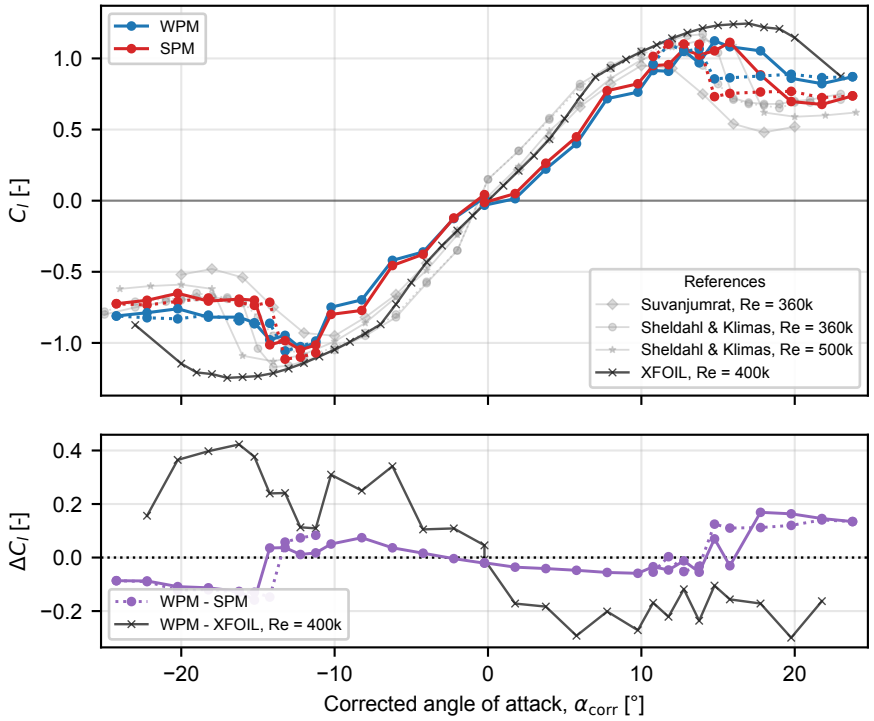


Figure 3.9: Measured lift curves and signed differences at $Re = 400{,}000$, second campaign [37, 34].

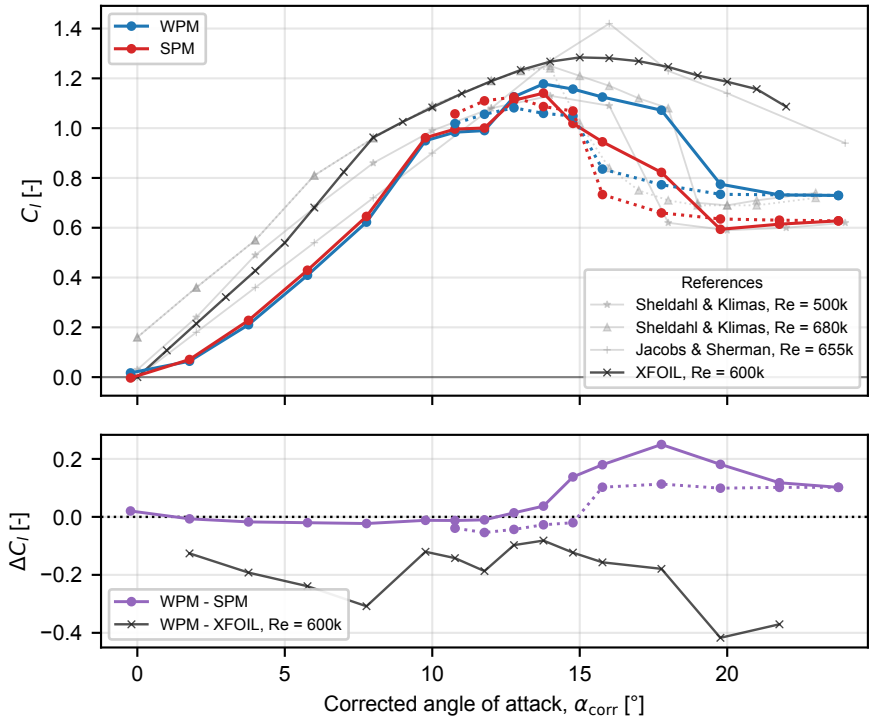


Figure 3.10: Measured lift curves and signed differences at $Re = 600{,}000$ [34, 21].

3.6. Discussion

The following section discusses the main trends and phenomena observed in the experimental results. The agreement between WPM and SPM is evaluated across the different aerodynamic regimes. Subsequently, the commonly observed phenomena are highlighted and their possible origins are discussed, followed by a comparison of SPM and WPM data with the set of reference curves.

3.6.1. Common trends in WPM versus SPM

To quantify the differences between WPM and SPM, Figure 3.11 presents the root mean square error (RMSE) for the three main aerodynamic regimes. For each campaign and regime, the RMSE is expressed as a percentage of the mean SPM lift coefficient magnitude calculated from the same measurements. The pre-stall, stall and post-stall regimes are defined by $0° \leq |\alpha_{\text{corr}}| \leq 9°$, $9° < |\alpha_{\text{corr}}| \leq 15°$ and $15° < |\alpha_{\text{corr}}| \leq 25°$, respectively. Only the primary sweep away from zero angle of attack is considered, excluding return-sweep measurements.

The relative RMSE does not change consistently from pre-stall to stall across the four campaigns. It increases at $Re = 200{,}000$ but decreases in the other campaigns, most noticeably in the second $Re = 400{,}000$ test. In contrast, it increases from stall to post-stall in every campaign. This consistent increase indicates that WPM agrees less closely with SPM in the post-stall regime. A similar deterioration in agreement beyond stall has also been reported in previous WPM studies [25].

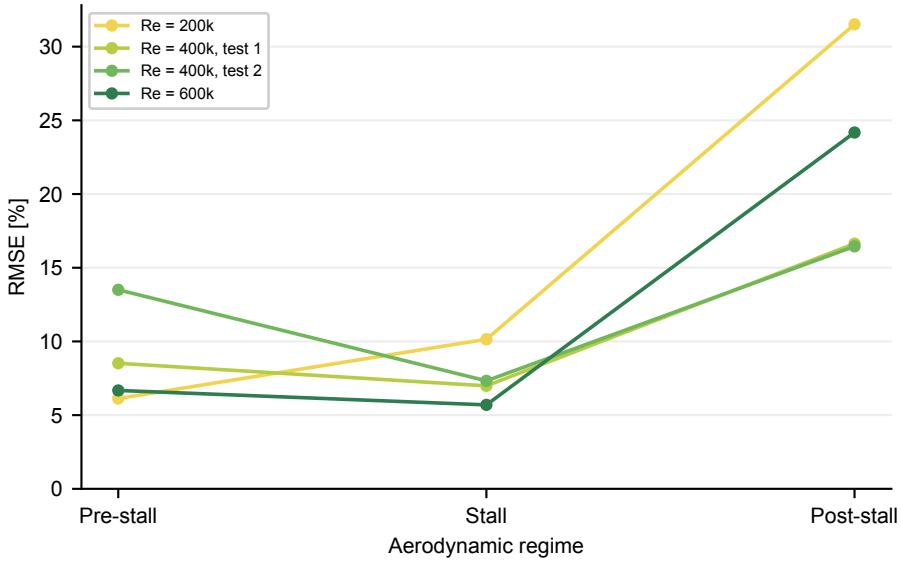
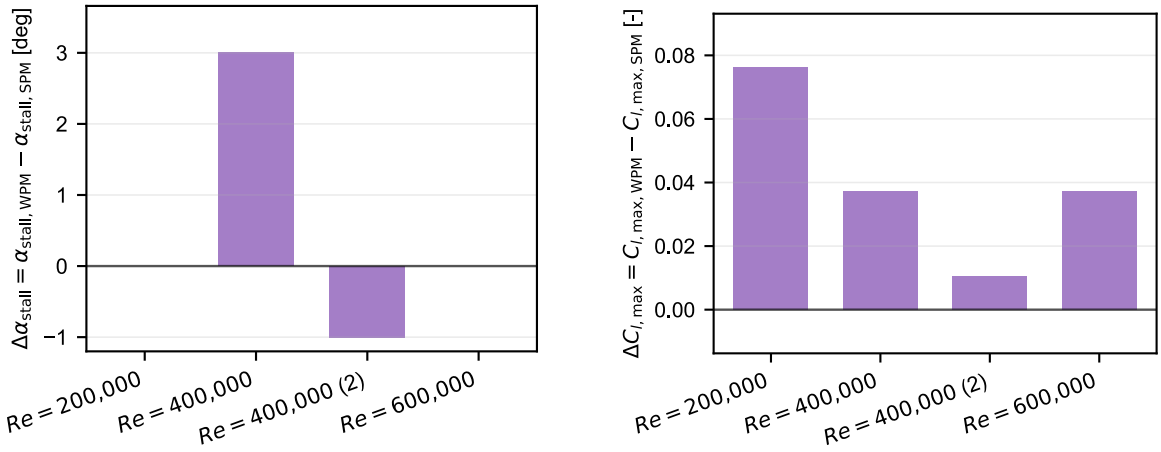


Figure 3.11: RMSE between WPM and SPM across the pre-stall, stall and post-stall regimes.

To assess the accuracy of WPM in predicting the maximum lift coefficient and stall angle of attack, both metrics are compared in Figure 3.12. Only the increasing-angle branch is considered, with the stall angle defined as the corrected angle of attack at which the maximum lift coefficient occurs. The stall angle is determined from measurements obtained at $1°$ increments, while the lift behaviour around stall can vary sharply between adjacent measurement points. Combined with the limited sample size of four test campaigns, this makes it difficult to draw firm conclusions regarding the accuracy of the predicted stall angle.

The maximum lift coefficient, on the other hand, is reproduced more consistently by the WPM method, with the absolute differences remaining below approximately 0.08 across all campaigns.



(a) Difference in predicted stall angle

(b) Difference in predicted maximum lift coefficient

Figure 3.12: Differences between WPM and SPM in stall angle and maximum lift coefficient across the four experimental campaigns.

Furthermore, the stall-recovery angle is observed to be essentially identical for WPM and SPM across all four experimental campaigns, as seen in Figure 3.7 to Figure 3.10. Although the number of campaigns is limited, this consistent agreement indicates that WPM is capable of capturing the angle at which the flow reattaches with good accuracy.

3.6.2. Additional observed phenomena

- **Plateau around $\alpha = 0°$.** The lift curves show a plateau for both WPM and SPM in the vicinity of $\alpha = 0°$. Since this behaviour is captured by both measurement methods, it is unlikely to originate from the measurement technique itself. Similar nonlinear lift behaviour has previously been observed for symmetric airfoils at low Reynolds numbers, particularly between $40{,}000$ and $100{,}000$, and has been attributed to the interaction between laminar separation bubbles on the upper and lower surfaces [33]. These separated regions alter the boundary-layer displacement thickness and thereby modify the effective aerodynamic shape of the airfoil.

  A small change in angle of attack can cause the separation bubbles on the upper and lower surfaces to change differently in size and position. The resulting change in effective airfoil geometry can partly oppose the expected increase in lift with angle of attack, reducing the local lift-curve slope and producing a plateau around zero incidence. As the angle of attack increases further, the separation bubble moves upstream and decreases in size, reducing its influence on the lift-curve slope.

  However, this mechanism has primarily been observed and studied at Reynolds numbers between $40{,}000$ and $100{,}000$ [33], and its presence is therefore not proven for the present experiments. In the present measurements, the plateau is most pronounced at $Re = 200{,}000$, where it extends to approximately $\alpha = 4°$. At the higher Reynolds numbers, the plateau appears to extend only to approximately $\alpha = 2°$, and to approximately $\alpha = -2°$ for the negative-angle measurements. The decreasing extent of the plateau with increasing Reynolds number is qualitatively consistent with a diminishing influence of laminar separation bubbles. This supports the proposed mechanism, although the lift measurements alone are insufficient to confirm the presence of a laminar separation bubble.
- **Hysteresis:** Hysteresis refers to the dependence of the lift response on the direction of the angle-of-attack sweep. Near stall, large-scale flow separation causes a sharp reduction in C_l. During the decreasing-angle sweep, reattachment occurs at an angle of attack lower than the angle at which stall first occurred. Consequently, the increasing- and decreasing-angle lift curves do not coincide over the stall and recovery range. This behaviour is visible in both WPM and SPM.
- **Sweep-direction discrepancy:** A systematic difference is observed between the increasing- and

decreasing-angle sweeps when comparing lift coefficients under attached-flow conditions, with the sweep-down measurements generally yielding higher values. At $\alpha = 11^\circ$ and 12°, where the flow has reattached during the decreasing-angle sweep, the average increase ranges from approximately 5% to 11% for both WPM and SPM, as shown in Table 3.2.

A gradual temperature decrease during the measurements was considered as a possible explanation. Since the tunnel velocity was initially set from the measured dynamic pressure and the corresponding static pressure was subsequently maintained, the main effect of temperature drift is a change in Reynolds number rather than a direct proportional change in the measured lift coefficient. For a representative temperature decrease of $3\ \mathrm{K}$, the resulting Reynolds-number increase is approximately 1.3%. This is considerably smaller than the observed sweep-direction differences and is therefore unlikely to explain them.

A more plausible contribution is a small systematic offset in the actual angle of attack introduced when the direction of rotation is reversed, for example due to mechanical play or backlash in the mounting system. Using a representative lift-curve slope of approximately $0.1\ \mathrm{deg}^{-1}$ and an observed difference of $\Delta C_l \approx 0.05 - 0.10$, the corresponding angular offset is approximately

$$\Delta\alpha \approx \frac{\Delta C_l}{dC_l/d\alpha} \approx 0.5^\circ - 1.0^\circ. \tag{3.4}$$

The magnitude obtained from Equation 3.4 is sufficiently small to be mechanically plausible and could therefore explain a substantial part of the observed sweep-direction discrepancy.

Table 3.2: Average relative increase in lift coefficient from the increasing- to decreasing-angle sweep at $\alpha = 11^\circ$ and 12°.

Reynolds number	WPM increase [%]	SPM increase [%]
200,000	10.39	5.09
400,000	11.14	10.13
600,000	5.06	8.53

3.6.3. Comparison with reference curves

At $Re = 200{,}000$, the published lift curves show considerable scatter. The WPM and SPM lift coefficients lie above several of the published measurements over much of the pre-stall range. Suvanjumrat's measurements at $Re = 160{,}000$ show a similar rise in lift before stall and a similarly abrupt drop at stall, although the drop occurs at a lower angle of attack [37]. The lower Reynolds number may contribute to the earlier stall, but its effect cannot be separated from differences between the experimental setups.

At the same nominal Reynolds number as the present tests, Troolin et al. report lower lift coefficients in the linear regime. They tested a finite-span wing with an aspect ratio of 1.6, whereas the model in the present study spans the wind-tunnel test section [39]. For a finite wing, downwash reduces the effective angle of attack and thus the lift-curve slope relative to that of a two-dimensional airfoil. Troolin et al. report applying a finite-aspect-ratio correction when comparing their results with NACA data [39]. However, the NACA 0015 curve examined in Report 586, which is corrected to infinite aspect ratio, lies below the plotted Troolin curve over the range compared [21, Fig. 4]. Applying a finite-span correction to an uncorrected Troolin curve would steepen it rather than bring it closer to the NACA curve examined here. This comparison therefore does not establish whether the plotted Troolin data were corrected or whether finite-span effects account for the difference with the present measurements.

At $Re = 400{,}000$ and $Re = 600{,}000$, both WPM and SPM give lower lift coefficients than the published reference curves over part of the pre-stall range [37, 34, 21]. After the plateau discussed in subsection 3.6.2, the difference reaches approximately $\Delta C_l = 0.3$. For a representative lift-curve slope of $0.1\ \mathrm{deg}^{-1}$, a difference of this magnitude would correspond to an angle-of-attack error of approximately 3°. Such an offset is unlikely given the experimental alignment and the considerably smaller angle correction inferred from the zero-lift measurements. A systematic error in dynamic pressure would rescale the entire lift curve and is unlikely to explain this discrepancy on its own.

Differences in boundary-layer transition or laminar separation, potentially associated with differences in free-stream turbulence or surface roughness, may contribute to the discrepancy. Residual wind-tunnel interference and uncertainty in the applied corrections may also play a role. The available measurements do not establish the relative importance of these effects. The similar shortfall in WPM and SPM indicates that the discrepancy is not specific to WPM. Relative to the published reference curves, WPM therefore gives conservative lift estimates over this part of the pre-stall range at the two higher Reynolds numbers.

3.7. Summary of experimental findings

The main objective of this experiment was to assess the capability of the WPM method to predict lift in the Econowind wind tunnel across the full aerodynamic range, including pre-stall, stall, post-stall, and stall-recovery behaviour. The comparison with the independently obtained SPM results shows that the performance of WPM is strongly dependent on the aerodynamic regime.

In the pre-stall region, WPM closely follows the SPM-derived lift curves for all investigated Reynolds numbers. The relatively small discrepancies observed in this regime indicate that WPM is capable of reliably reproducing changes in airfoil lift while the flow remains predominantly attached. Both methods also capture the same Reynolds-dependent trends and secondary aerodynamic features, suggesting that these observations are not artefacts specific to the WPM methodology.

The relative RMSE does not increase consistently from pre-stall to stall, but increases from stall to post-stall in all four campaigns. In the post-stall regime, WPM consistently overpredicts lift relative to SPM. This demonstrates that the established WPM approach becomes less reliable once large-scale flow separation develops. The increasing discrepancy is therefore associated primarily with the change in flow regime rather than with Reynolds number alone.

Despite these differences, WPM captures the principal qualitative features of the measured lift behaviour, including stall onset, hysteresis, and stall recovery. The method can therefore provide useful information on changes in aerodynamic loading even when the absolute post-stall lift estimate becomes inaccurate. This distinction is particularly relevant for the intended application to bluff lifting bodies employing suction, where changes between attached and separated flow states are of primary interest.

Overall, the present experiment validates the use of WPM for lift estimation under predominantly attached-flow conditions, while identifying post-stall flow as the main limitation of the current methodology. The consistent post-stall overprediction indicates that additional flow phenomena, particularly those associated with the separated wake and the finite wall-pressure measurement region, must be considered before the method can be applied reliably to strongly separated flows. These effects are investigated further in chapter 4.

4

Limitations of WPM in separated flow

4.1. Motivation and approach

The results presented in chapter 3 showed that WPM agrees well with SPM in the pre-stall region. However, this agreement deteriorates beyond stall angle, with WPM consistently overpredicting the lift coefficient in the post-stall regime. This raises the question of whether these discrepancies can be accounted for through an alternative model or by modifying the existing potential-flow-based correction approach.

The lift curves alone provide insufficient information to explain the origin of these discrepancies. A more detailed examination of the measured wall-pressure distributions is therefore required, shifting the focus from the resulting lift coefficients to the underlying pressure footprints. This investigation is guided by three main questions:

- How does the measured wall-pressure footprint change as the airfoil enters the stall and post-stall regimes?
- Can the pressure distribution beyond the finite pressure-port range be reconstructed using approaches other than the existing potential-flow-based correction?
- What can be inferred about the unmeasured wall-pressure contribution outside the pressure-port range in the post-stall regime?

Answering these questions provides insight into the behaviour of the wall-pressure footprint and the extent to which the pressure distribution outside the measured region can be predicted.

4.2. Evolution of the wall-pressure footprint

The systematic overprediction of post-stall lift by WPM shifts the focus from the resulting lift curves to the wall-pressure distributions from which the WPM lift estimates are obtained. To investigate how the measured pressure footprint evolves with increasing angle of attack, the complete set of wall-pressure distributions at $Re = 200{,}000$ is presented in Figure 4.1.

A gradual increase in the magnitude of the wall-pressure footprint is observed with increasing angle of attack up to stall. This behaviour is consistent with the increasing lift of the airfoil. At this Reynolds number, the lift curve (Figure 3.7) showed a sudden stall onset between $\alpha = 14°$ and $\alpha = 15°$, allowing for a clear comparison between the pressure footprints immediately before and after stall. The two pressure distributions corresponding to these two angles are therefore individually plotted in Figure 4.2.

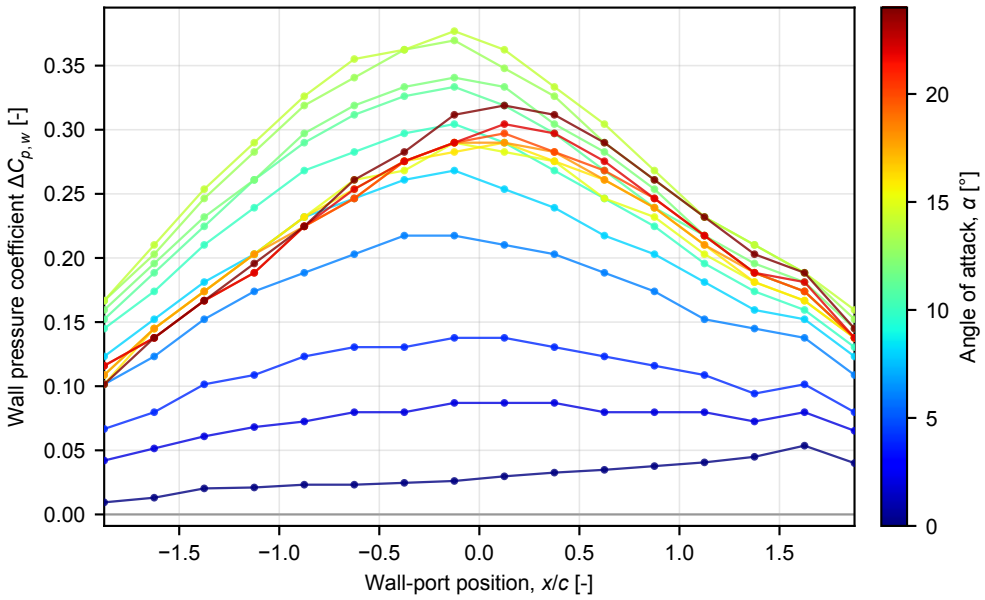


Figure 4.1: Evolution of the wall-pressure footprint during the increasing-angle sweep at $Re = 200{,}000$.

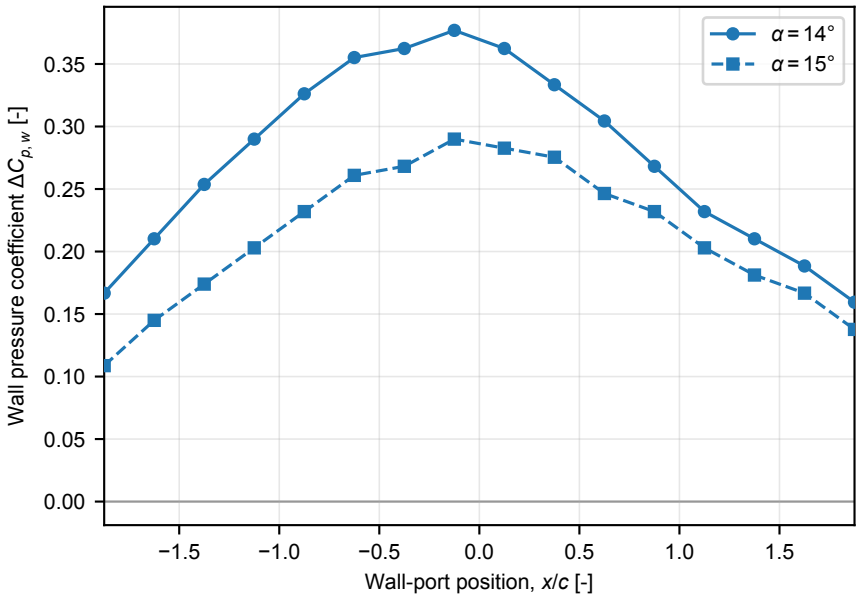


Figure 4.2: Wall-pressure footprints before and after stall at $\alpha = 14°$ and $\alpha = 15°$, respectively, for $Re = 200{,}000$.

Three main features of the wall-pressure footprint are particularly relevant when comparing the pre-stall and post-stall regimes:

- **Peak magnitude decreases:** This change is consistent with the drop in lift after stall. The aerodynamic force exerted by the airfoil on the flow decreases, accompanied by a reduction in the differential wall-pressure magnitude.
- **Peak moves downstream:** During stall, the flow detaches from the airfoil and a wake forms,

as illustrated in Figure E.8. Due to this separation, the transverse momentum generated by the airflow is redistributed and transferred further downstream, causing the wall-pressure distribution to shift accordingly.

- **Pressure remains non-zero at the measured boundaries:** The wall-pressure distribution has not returned to zero at the upstream and downstream limits of the measured domain, whereas the pre-stall distributions are generally closer to zero at these limits. This indicates that a pressure contribution remains outside the measured pressure-tap range.

The abrupt change in the measured wall-pressure footprint across stall therefore suggests that the unmeasured portions of the pressure distribution may also undergo substantial changes, motivating a closer investigation of their post-stall behaviour.

4.3. Empirical extrapolation of the wall-pressure footprint

To assess the predictability of the pressure footprint outside the measured region, a more direct approach can be considered. Rather than relying on the existing potential-flow-based correction, the measured wall-pressure distribution can be extrapolated using suitable fitting functions and subsequently integrated over the extended domain.

A first set of candidate functions was selected based on two criteria:

- The differential wall-pressure distribution appears, at first inspection, to exhibit a normal-distribution-like shape. The selected fitting functions should therefore be capable of representing a similar distribution.
- The fitting functions should approach zero as $x \to \pm\infty$, consistent with the wall-pressure disturbance vanishing sufficiently far from the airfoil.

As a first step, only strictly positive fitting functions are considered. The resulting candidate fits are shown in Figure 4.3 and Figure 4.4 for a pre-stall and post-stall angle of attack, respectively. In both figures, the shaded area represents the measured wall-pressure domain, with blue markers indicating the measured values. Solid lines represent the fitted distributions within the measurement region, while dashed lines indicate their extrapolation beyond this region. Both regimes are included because empirical extrapolation may also provide a more direct alternative in the pre-stall region, where the existing potential-flow-based correction was found to perform well.

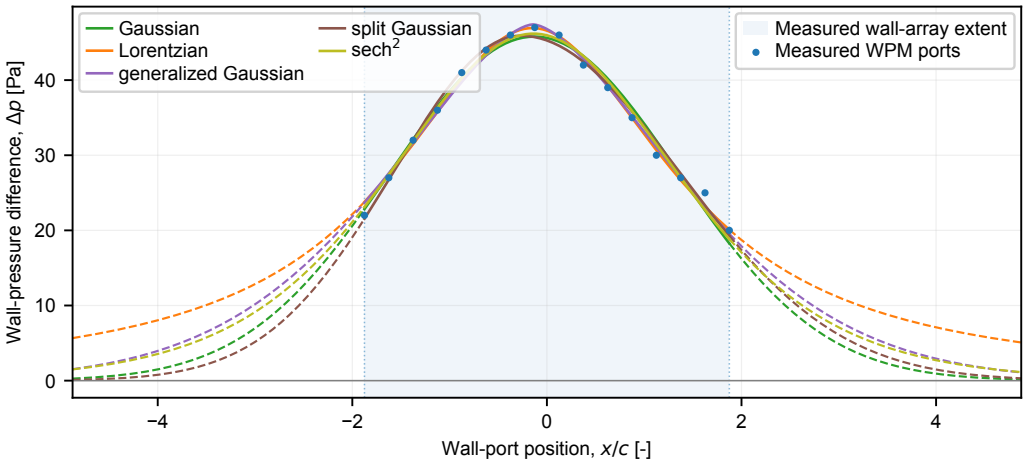


Figure 4.3: Empirical extrapolation functions for the pre-stall wall-pressure footprint at $\alpha = 12°$ ($\alpha_{\text{corr}} \approx 11.77°$) and $Re = 200{,}000$.

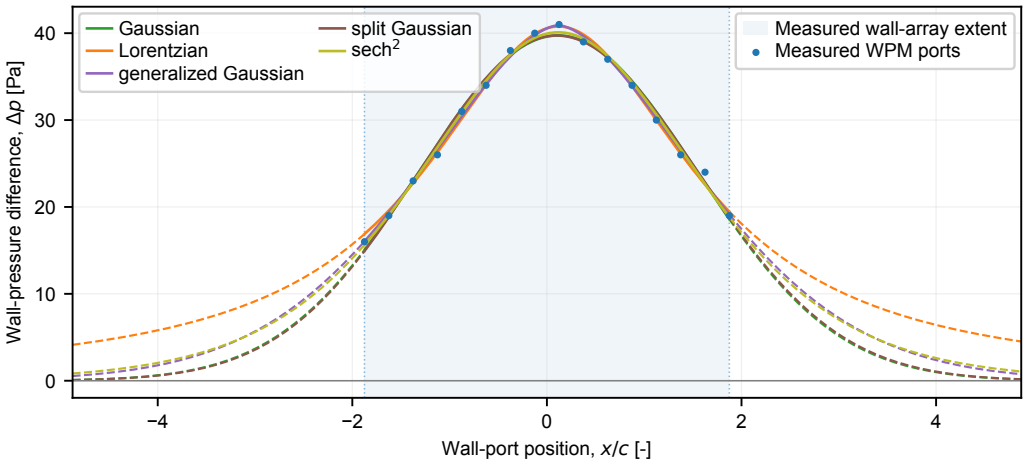


Figure 4.4: Empirical extrapolation functions for the post-stall wall-pressure footprint at $\alpha = 20°$ ($\alpha_{\mathrm{corr}} \approx 19.77°$) and $Re = 200{,}000$.

It can be observed that all five fitting functions reproduce the measured data points well, as further indicated by the fit-quality metrics reported in Table 4.1. The table also shows the resulting increase in lift coefficient relative to the value obtained by integrating only the measured, non-extrapolated pressure footprint.

Table 4.1: Fit quality and resulting lift correction for the candidate extrapolation functions at pre-stall and post-stall conditions.

	Pre-stall, $\alpha = 12°$		Post-stall, $\alpha = 20°$	
Model	R^2	ΔC_l	R^2	ΔC_l
Gaussian	0.9819	0.25563	0.9905	0.19818
Generalised Gaussian	0.9909	0.36760	0.9962	0.26505
Lorentzian	0.9919	0.89532	0.9946	0.72452
Sech squared	0.9874	0.34661	0.9943	0.27218
Split Gaussian	0.9892	0.24838	0.9906	0.19894

Based on the integration of the extrapolated pressure distributions, a new set of lift curves was obtained. Figure 4.5 compares these curves with the finite-integration WPM and SPM results, as well as the WPM results corrected using the existing potential-flow-based model. All WPM-derived curves were independently zero-calibrated using linear fits over $4° \leq |\alpha_{\mathrm{corr}}| \leq 10°$ from the two $Re = 400{,}000$ campaigns. Solid and dotted lines represent increasing and decreasing angles of attack, respectively. General wind-tunnel interference corrections were not applied in this comparison.

The Lorentzian extrapolation substantially overpredicts lift throughout the investigated range due to its relatively large tail contributions. The remaining empirical methods reproduce the SPM lift coefficients reasonably well in the pre-stall region, without showing a clear disadvantage relative to the potential-flow-based correction. However, they exhibit a similar tendency towards lift overprediction in the post-stall regime. As illustrated by the absolute lift-coefficient differences in the lower panel of Figure 4.5, the generalised Gaussian and sech^2 functions provide comparably good agreement with SPM across much of the investigated range. These two functions are therefore considered for further analysis.

Deviations are also observed near $\alpha = 0°$, where the differential wall-pressure signal is small and the measured distribution lacks a clearly defined footprint shape. Consequently, small measurement variations can substantially affect the fitted functions, making the extrapolation poorly constrained and less reliable near zero incidence.

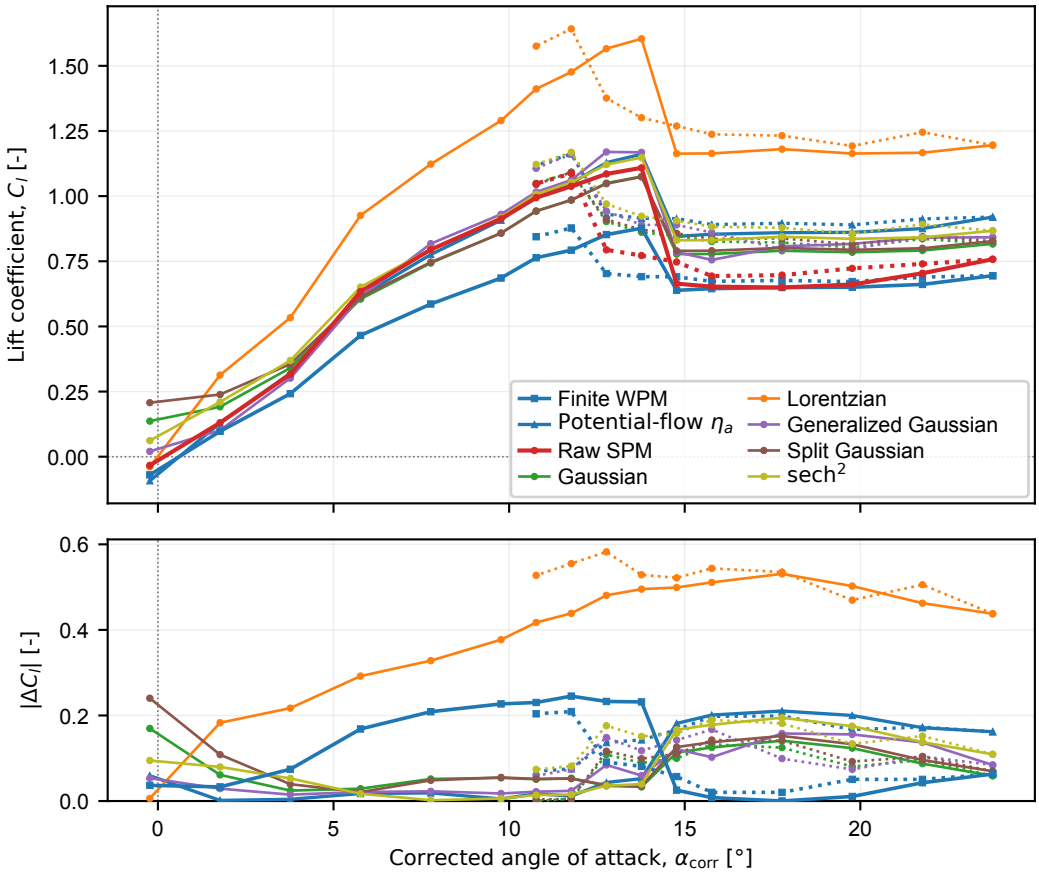


Figure 4.5: Comparison of lift coefficients obtained using finite WPM integration, potential-flow correction and empirical extrapolation against raw SPM results at $Re = 200{,}000$. The lower panel shows the absolute lift-coefficient difference between each WPM method and SPM.

Another notable observation is that the lift estimates obtained from the finite, non-extrapolated wall-pressure footprint agree reasonably well with SPM in the post-stall regime. This indicates that adding a positive contribution outside the measured range does not necessarily improve the lift estimate. The implications for the transverse momentum balance are discussed in section 4.4.

4.4. Physical interpretation of the post-stall discrepancy

In the previous section, it was observed that the lift coefficients obtained through finite integration of the measured wall-pressure distributions appear to coincide with those obtained from SPM. To further investigate the implications of this observation for extrapolating the finite wall-pressure footprint, the complete pressure distribution is divided into three regions, as illustrated in Figure 4.6. Region 1 represents the upstream pressure distribution, extending from $x = -\infty$ to the first measurement port. Region 2 corresponds to the measured pressure distribution between the first and last pressure ports and therefore represents the captured pressure footprint. Finally, Region 3 represents the downstream pressure distribution, extending from the last measurement port to $x = +\infty$.

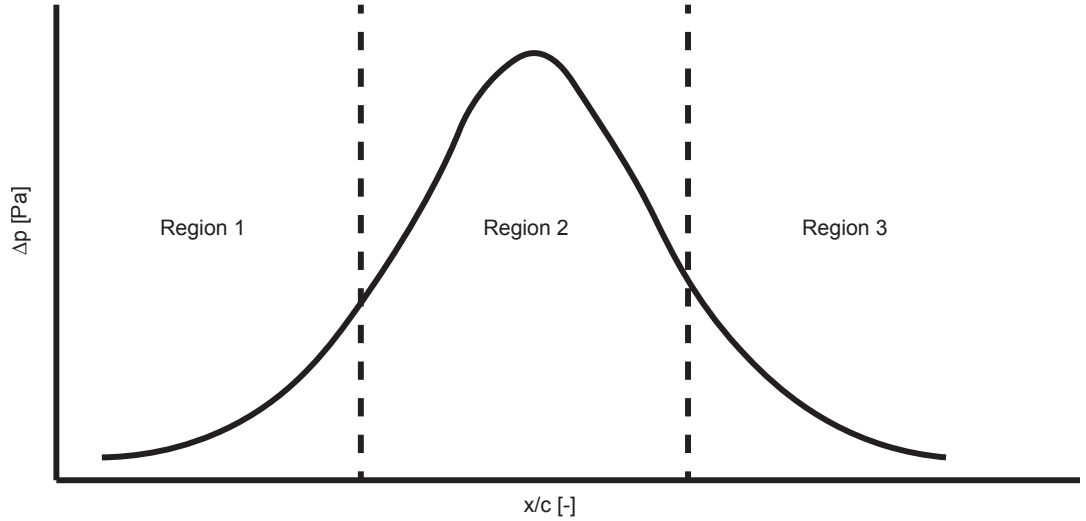


Figure 4.6: Schematic division of the differential wall-pressure distribution into the upstream (Region 1), measured (Region 2) and downstream (Region 3) regions.

The observation that integration over Region 2 produces a lift estimate close to the SPM result in the post-stall regime has important implications for the unmeasured pressure distributions in Regions 1 and 3. Two possible explanations can be considered.

The first possibility is that the pressure contributions from Regions 1 and 3 are negligible. Under this assumption, the net difference between the transverse momentum fluxes entering and leaving the measured region would have to be small for the airfoil and wall-pressure forces to approximately balance. However, this explanation is physically unlikely, as the measured pressure distribution would have to decay to zero immediately beyond the measurement boundaries, despite remaining nonzero at these locations. Such behaviour would imply an abrupt change in the pressure distribution that is inconsistent with the expected gradual spatial variation of wall pressure.

An alternative explanation is that the unmeasured pressure contributions from Regions 1 and 3 partially or fully cancel each other. In particular, the presence of the separated wake could introduce a reversal in the wall-pressure difference further downstream, resulting in a pressure contribution of opposite sign to that captured in Region 2. Such a reversal could explain why integrating only the measured pressure footprint produces lift coefficients close to those obtained from SPM, even though a nonzero pressure distribution may extend beyond the measurement region. This theory would result in an expected distribution as depicted in Figure 4.7.

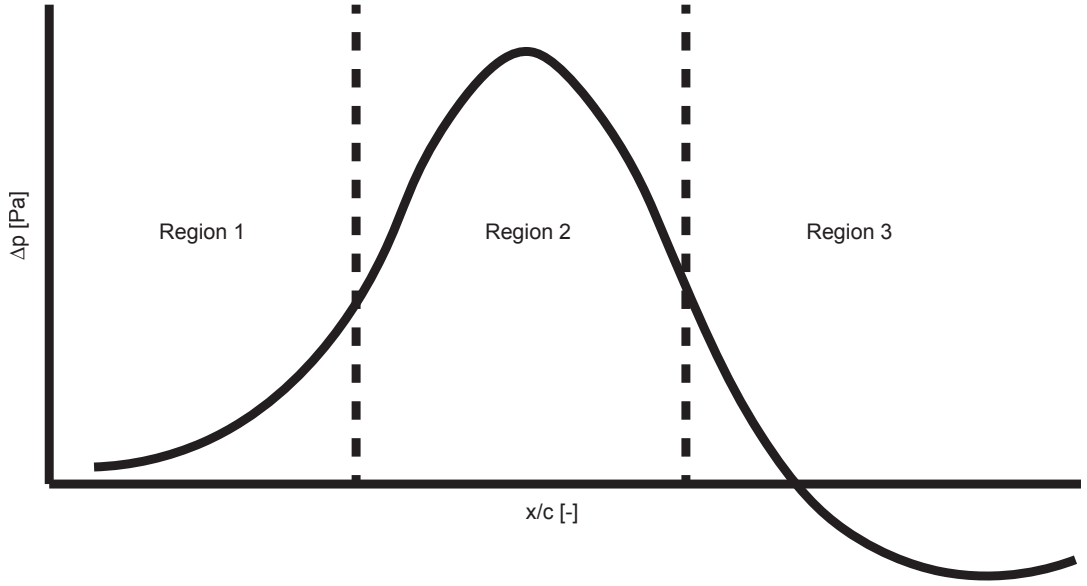


Figure 4.7: Schematic representation of a possible downstream reversal of the differential wall-pressure footprint.

This hypothesis can also be interpreted directly from the momentum balance of the three regions introduced in Figure 4.7. Assuming that no comparable pressure reversal occurs upstream, the wall-pressure contribution in Region 1 imparts transverse momentum to the flow before it enters the measured region. The flow therefore enters Region 2 with a positive transverse momentum flux. Within Region 2, the wall-pressure force and the aerodynamic force exerted by the airfoil approximately balance, such that the transverse momentum flux leaving Region 2 remains of similar magnitude to that entering it. If the flow sufficiently far downstream is assumed to return to an approximately streamwise state, this remaining transverse momentum must subsequently be reduced in Region 3. Under these assumptions, a wall-pressure force acting in the opposite transverse direction would be required, corresponding to a reversal in the differential wall-pressure contribution downstream. The qualitative pressure distribution illustrated in Figure 4.7 is therefore consistent with the momentum balance required to recover the far-downstream flow state.

4.5. Investigation using a separated-wake model

The momentum balance in Region 3 could, in principle, be investigated experimentally in two ways. First, the transverse momentum flux leaving Region 2 could be measured directly, allowing the unknown downstream contribution to the momentum balance to be quantified. This would require measurements of both the streamwise and transverse velocity components across the outlet plane. Alternatively, the wall-pressure distribution could be measured sufficiently far downstream to determine whether the predicted pressure reversal occurs directly. Neither approach can readily be implemented within the present experimental setup. Direct evaluation of the transverse momentum flux would require additional multi-component velocity measurements, while extending the wall-pressure measurements farther downstream is limited by the finite length of the instrumented test section. A theoretical model of the separated wake is therefore considered as an alternative means of investigating the expected downstream wall-pressure behaviour. Rather than serving as a direct correction method, the model is used primarily to assess whether a reversal of the differential wall-pressure contribution can arise under separated-flow conditions and under which conditions such behaviour may be expected.

4.5.1. Wu wake model

A theoretical model proposed by [44] is used to investigate whether a downstream reversal of the differential wall pressure can occur under separated-flow conditions. The model describes the inviscid outer flow around an inclined flat plate with a separated wake by representing the viscous wake with an equivalent potential flow. For a given plate geometry, the solution depends on two parameters, the angle of attack α and the wake underpressure coefficient σ_{Wu}.

The cavity pressure p_c is the constant static pressure prescribed along the near-wake boundary after separation and before pressure recovery begins. The wake underpressure coefficient expresses how far this pressure lies below the freestream static pressure p_∞, normalised by the freestream dynamic pressure.

$$\sigma_{\mathrm{Wu}} = \frac{p_\infty - p_c}{\frac{1}{2}\rho U_\infty^2}. \tag{4.1}$$

The model distinguishes between fully and partially developed wakes based on where the pressure begins to recover towards p_∞. In a partially developed wake, recovery begins along the plate before the trailing edge, whereas in a fully developed wake, it begins downstream of the trailing edge. The governing formulations for both wake regimes are presented in Appendix B.

For each combination of α and σ_{Wu}, the conformal mapping is inverted to obtain the velocity field. Since the model represents flow around an inclined flat plate rather than the actual airfoil, it is used to assess qualitatively whether a reversal of the differential wall pressure is possible.

4.5.2. Predicted wall-pressure response

With the velocity field determined, the corresponding pressure field was obtained using Bernoulli's equation, as given in Equation E.3. The pressure was evaluated along two hypothetical wall locations positioned at the same distance from the airfoil as the upper and lower walls of the wind-tunnel test section. Since Wu's model represents an unbounded flow field, these lines serve only as pressure-sampling locations and do not impose physical wall boundary conditions.

The resulting differential wall-pressure distribution was evaluated over a range of angles of attack and wake underpressure coefficients. Figure 4.8 illustrates the evolution of the predicted pressure footprint for angles of attack between 10° and 30°, at a constant wake underpressure coefficient of $\sigma_{\mathrm{Wu}} = 0.90$. The primary objective of this analysis is to determine whether the separated-wake model can reproduce a reversal in the differential wall-pressure contribution. Such a reversal becomes apparent at angles of attack exceeding approximately 28°. However, even below this threshold, the magnitude of the downstream pressure contribution decreases substantially with increasing angle of attack. This reduction may already improve lift predictions based on the finite wall-pressure footprint, as discussed further in subsection 4.5.4.

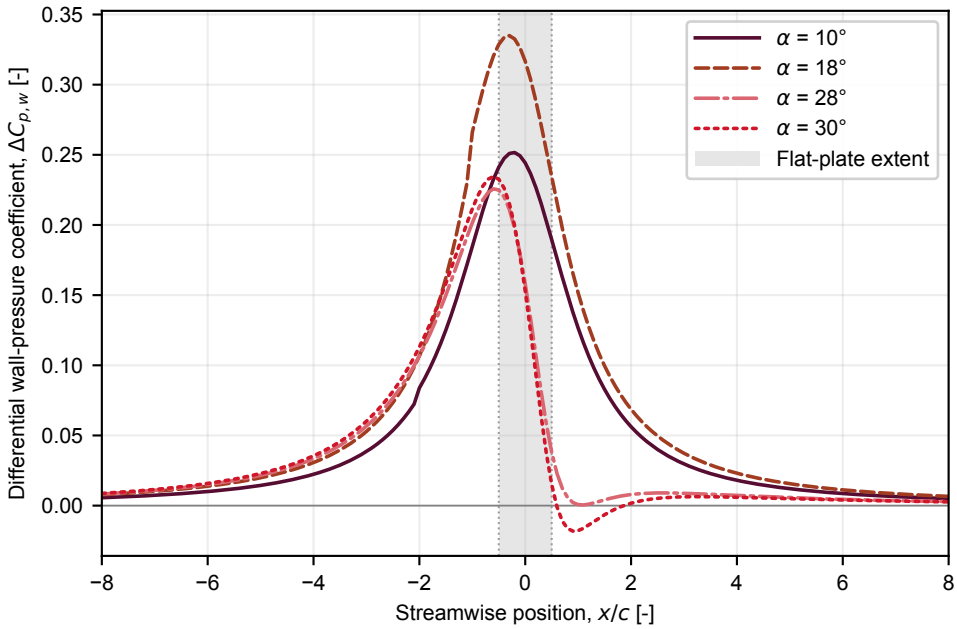


Figure 4.8: Evolution of the differential wall-pressure distribution predicted by Wu's separated-wake model at a constant wake underpressure coefficient of $\sigma_{\mathrm{Wu}} = 0.90$.

To identify the combinations of angle of attack and wake underpressure coefficient for which a pressure reversal occurs, the minimum differential wall-pressure coefficient was determined over the evaluated streamwise domain for each parameter combination. The resulting values are presented in Figure 4.9. Negative minimum values indicate conditions under which the model predicts a reversal in the differential wall-pressure contribution.

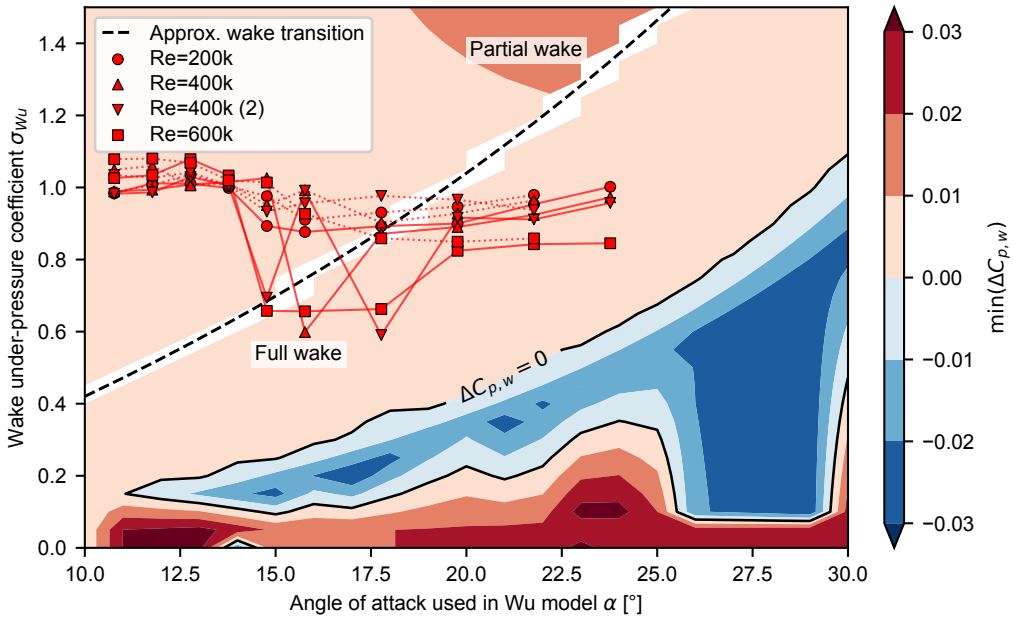


Figure 4.9: Minimum downstream differential wall-pressure coefficient predicted by [44], with SPM-derived experimental conditions overlaid. Negative values indicate pressure reversal.

The figure combines the partially and fully developed wake formulations. Although the distinction between these two wake states is physically based on the location at which pressure recovery begins, as discussed previously, each regime also corresponds to a specific range of combinations of σ_{Wu} and α. The dotted black line indicates the transition between the two regimes.

The model predicts a reversal of the differential wall-pressure contribution for sufficiently low values of σ_{Wu} or sufficiently large angles of attack. These conditions are represented by the blue region enclosed by the solid black contour. Some regions of the map show a positive minimum differential pressure, even though the pressure difference is expected to approach zero sufficiently far from the airfoil. This occurs because the minimum is evaluated only over the finite downstream domain $1 < x/c < 8$. For some combinations of α and σ_{Wu}, this domain is not sufficiently long for the differential pressure to approach zero or become negative.

The experimental conditions from the present study are also included in the figure and are discussed further in subsection 4.5.3.

4.5.3. Comparison with experimental conditions

The experimental conditions are overlaid on the Wu pressure-differential map in Figure 4.9. For each measurement, the wake underpressure parameter σ_{Wu} was estimated from the pressure measured over the separated region on the suction side of the airfoil. Figure 4.10 illustrates the range of surface-pressure values used to estimate the cavity pressure p_c required in Equation 4.1. Since the wake underpressure coefficient is equivalent to the negative cavity-pressure coefficient, the required value can be obtained directly by changing the sign of the average C_p over this region.

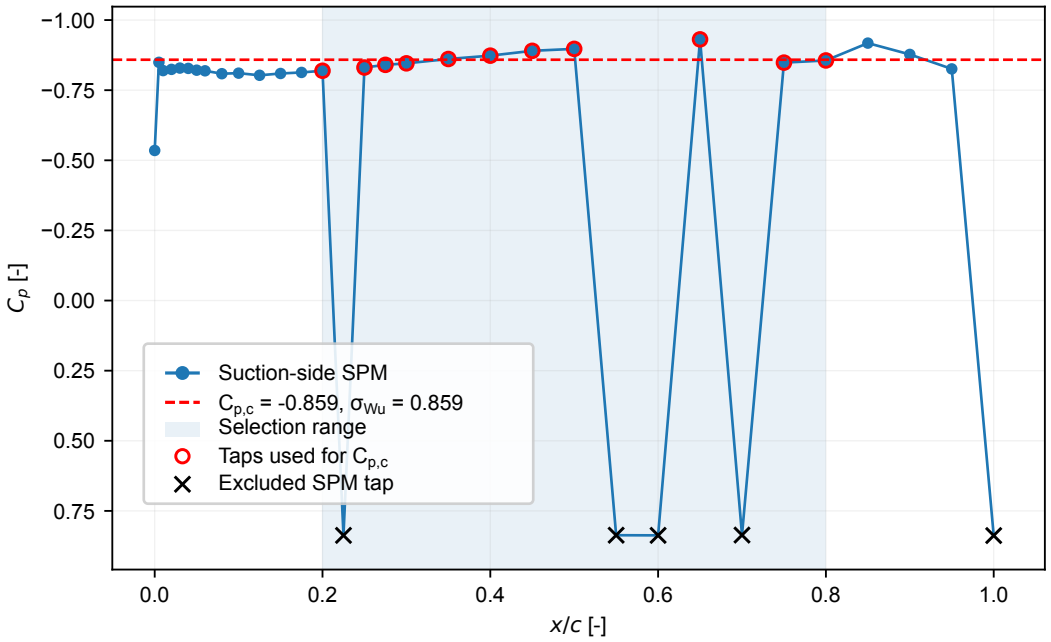


Figure 4.10: Suction-side pressure distribution at $\alpha = 22°$, illustrating the selection of pressure taps used to estimate $C_{p,c}$ and determine σ_{Wu}.

Overlaying the experimental conditions on the Wu map reveals several notable features. At the lower angles of attack considered, the experimental points lie within the partially developed wake region. As the angle of attack increases, the points transition into the fully developed wake region at approximately $\alpha = 17.5°$. This transition is broadly consistent with the experimentally observed development of strong flow separation following stall, which occurs at approximately $\alpha = 15°$ for the corresponding Reynolds number.

Several experimental points also exhibit noticeably lower values of σ_{Wu} than neighbouring measure-

ments. Inspection of the corresponding suction-side pressure distributions shows that these deviations coincide with a reduction in the magnitude of the negative pressure plateau around stall, particularly immediately before stall in certain cases. The resulting lower values of σ_{Wu} therefore reflect changes in the measured pressure distributions rather than isolated measurement outliers.

Although the experimentally derived conditions show reasonable agreement with the distinction between the partially and fully developed wake regimes, they do not enter the region in which the model predicts a negative differential wall-pressure contribution. The Wu model therefore demonstrates that a downstream reversal of the differential wall pressure is possible within a separated-wake flow, but it does not predict such a reversal for the specific combinations of angle of attack and wake underpressure obtained in the present experiments. Consequently, the model supports the qualitative plausibility of the proposed pressure-reversal mechanism, but does not provide direct confirmation that it occurred under the tested conditions.

4.5.4. Obtaining lift values using Wu's pressure distributions

Although the separated-wake model proposed by Wu does not predict a reversal of the differential wall pressure for the experimental conditions considered in this study, the resulting pressure distributions may still provide a physically motivated shape for extrapolating the measured wall-pressure footprint. To investigate this possibility, the Wu pressure distribution corresponding to the measured angle of attack and wake under-pressure coefficient was mapped onto the experimentally obtained differential wall-pressure distribution.

Only the downstream side of the pressure peak was represented using the Wu distribution, since this part of the footprint is expected to be most strongly influenced by the separated wake. Upstream of the peak, the pressure distribution was represented by the best-performing empirical fit identified in section 4.3. For each measurement, both the generalized Gaussian and sech^2 functions were fitted to the measured wall-pressure data, after which the function with the lowest RMSE at the measured wall-pressure locations was selected. The empirical and Wu distributions were joined at the pressure peak, resulting in the hybrid pressure distribution illustrated in Figure 4.11 for a representative post-stall measurement.

The mapping of the downstream Wu distribution consists of three transformations. First, the Wu distribution is shifted in the streamwise direction such that its pressure peak coincides with that of the empirical distribution. The distribution is subsequently stretched in the streamwise direction by a factor K_x, which is fitted to the measured wall-pressure points downstream of the peak. Finally, a vertical scaling factor K_y is applied such that the Wu distribution is anchored to the empirical distribution at the pressure peak. In this way, the experimentally supported upstream footprint is retained while the downstream extrapolation follows the shape predicted by the separated-wake model.

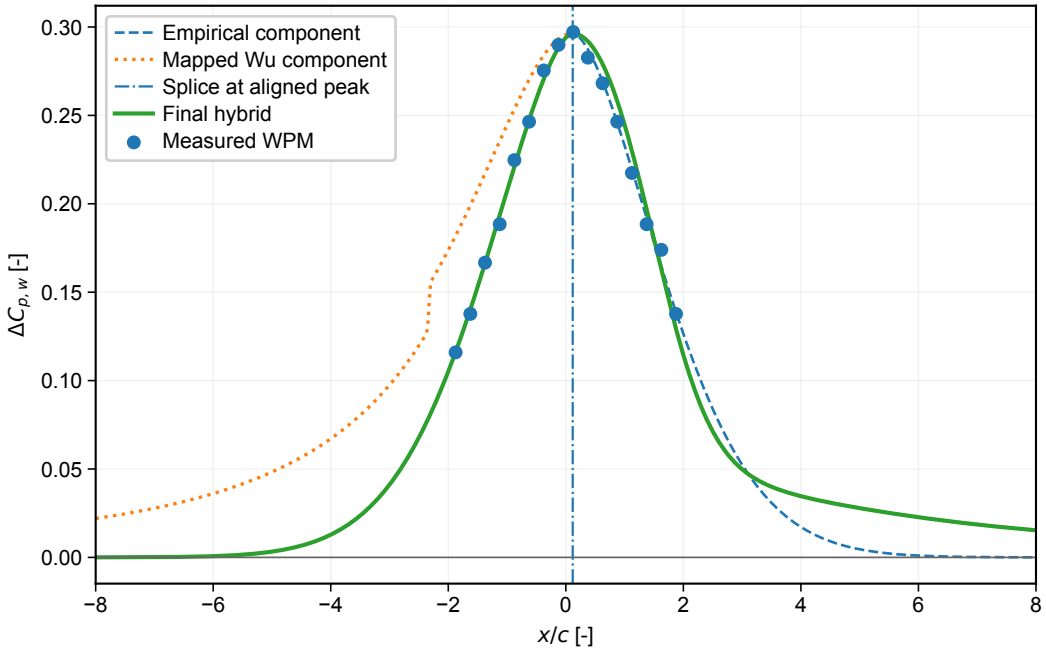


Figure 4.11: Construction of the hybrid wall-pressure distribution for $Re = 200{,}000$ at $\alpha = 20°$.

The resulting hybrid pressure distributions were integrated to obtain the corresponding lift coefficients. As shown in Figure 4.12, the Wu-based hybrid method continues to overpredict the lift coefficient in the post-stall regime and therefore does not improve the agreement with the SPM reference. The same qualitative behaviour was observed for the other Reynolds-number cases; therefore, only the results for $Re = 200{,}000$ are presented in this section for conciseness.

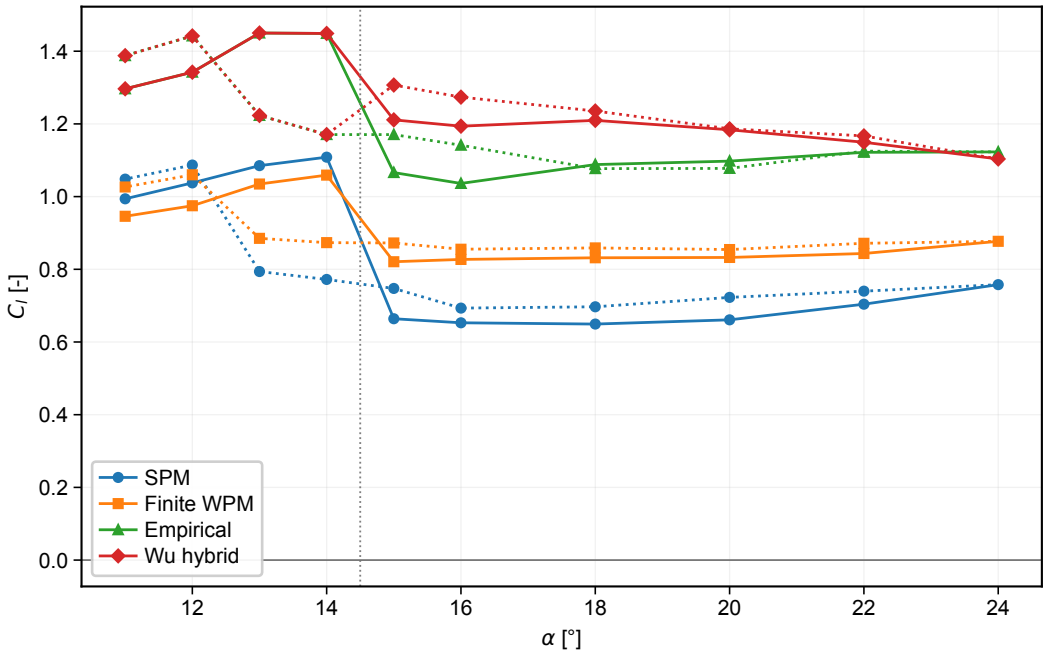


Figure 4.12: Comparison of lift coefficients obtained from SPM, finite WPM, empirical extrapolation and the Wu-based hybrid method for $Re = 200{,}000$.

As a final sensitivity study, an additional offset was applied to the angle of attack used to evaluate the Wu distribution. In this approach, the mapped Wu distribution is evaluated at an angle $\Delta\alpha$ larger than the corresponding baseline Wu angle. The purpose of this offset is to force the model farther into the separated-wake regime, thereby introducing a stronger downstream pressure reversal at lower experimental angles of attack.

The sensitivity results in Figure 4.13 show that increasing the applied offset reduces the reconstructed lift coefficient, as expected from the increasingly negative downstream pressure contribution. However, the shape of the resulting lift curve also changes substantially, and no single offset provides consistent agreement with the SPM measurements throughout the post-stall regime. A reliable quantitative correction therefore cannot be obtained using this approach. The model limitations discussed in subsection 4.5.5 provide further explanation for the remaining discrepancies between the Wu-based predictions and the experimental measurements.

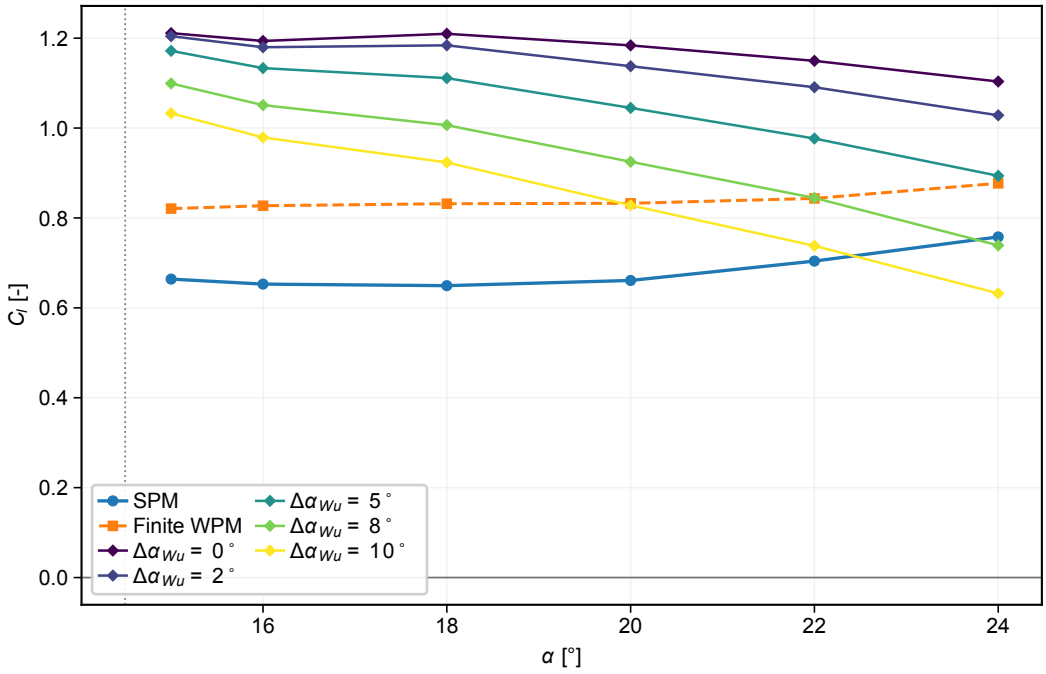


Figure 4.13: Sensitivity of the hybrid lift prediction to the applied Wu angle offset for $Re = 200{,}000$.

4.5.5. Model limitations

Three main limitations should be considered when interpreting the separated-wake model in its present implementation.

- **Flat-plate representation:** The pressure-differential map is based on the potential-flow field around an inclined flat plate rather than a NACA 0015 airfoil. Although the flow around a flat plate may become increasingly representative of a thin airfoil at sufficiently large angles of attack, the present test range extends only to approximately $24°$. Differences in geometry may therefore shift the location of the predicted transition and pressure-reversal regions in Figure 4.9.
- **Imaginary walls:** The pressure is evaluated along two hypothetical wall locations within an otherwise unbounded flow field. The predicted pressures therefore do not include the influence of the physical wind-tunnel walls. Since the Wu model provides a mapping between velocity and position rather than an explicit elementary potential representation that can readily be mirrored, incorporating wall effects using a simple method of images is not straightforward.
- **Required cavity pressure:** Even if the geometric and wall-related limitations were addressed, the model would still require the cavity pressure to be known in order to determine the wake underpressure parameter σ_{Wu}. In the present study, this value is estimated from surface-pressure mea-

surements on the suction side of the airfoil. The method therefore still requires model-mounted pressure measurements, which partly reduces the practical advantage of a wall-pressure-based approach that would otherwise avoid instrumentation of the model itself.

As a consequence of the first two limitations, the pressure-reversal map corresponding to the actual NACA 0015 configuration is expected to differ from that predicted by the present flat-plate, unbounded-flow model in Figure 4.9. The model should therefore be interpreted primarily as a qualitative tool for investigating whether a downstream pressure reversal can occur, rather than as a quantitative correction method for the post-stall WPM measurements.

5

Conclusions

The present study assessed the accuracy of wall-pressure measurements (WPM) for estimating aerodynamic lift across attached and separated flow regimes. Motivated by the need for a reliable lift measurement technique for Econowind's suction-controlled airfoils, the investigation focused on a conventional NACA0015 airfoil without boundary-layer suction, using surface-pressure measurements (SPM) as a reference. The results demonstrated good agreement before stall, but revealed significant discrepancies beyond stall, motivating further investigation into the wall-pressure response and possible improvements to lift estimation.

The extent to which the research objectives were achieved is evaluated below.

- **Investigate the theoretical assumptions underlying the WPM method and the correction procedure currently applied in the Econowind wind tunnel.**

  The WPM methodology is based on transverse momentum conservation, assuming approximately two-dimensional flow and accounting for momentum transport across the control-volume boundaries. The measured wall-pressure footprint, obtained from 16 pressure taps on each tunnel wall, is integrated over a finite domain. Contributions outside this domain are estimated using a potential-flow-based correction [1, 25], followed by solid-blockage and streamline-curvature corrections.

  Although momentum conservation remains applicable across different flow regimes, the adopted correction procedures rely on assumptions associated with attached, predominantly potential flow. Their validity therefore becomes questionable under separated-flow conditions.

- **Perform a controlled experiment on a non-suction airfoil in which lift obtained from WPM can be compared directly with independently obtained surface-pressure measurements.**

  A controlled experimental campaign was conducted using a NACA0015 airfoil equipped with surface-pressure taps. Its well-documented aerodynamic characteristics provided an additional reference for evaluating the results. Pressure distributions were measured on both the airfoil surface and tunnel walls across different angles of attack and Reynolds numbers. These measurements were independently processed to obtain WPM and SPM lift coefficients for direct comparison.

- **Assess the accuracy of WPM across the pre-stall, stall and post-stall aerodynamic regimes and determine how its performance varies with Reynolds number.**

  Following the application of the finite-domain, solid-blockage and streamline-curvature corrections, WPM lift coefficients were compared with SPM results. As shown in Figure 3.11, agreement was quantified for each campaign and aerodynamic regime using the root mean square error (RMSE), expressed as a percentage of the mean SPM lift coefficient magnitude for the same measurements. Only the primary sweep away from zero angle of attack was included.

The relative RMSE did not increase consistently from pre-stall to stall. In contrast, it increased from stall to post-stall in all four campaigns. No systematic relationship between relative RMSE and Reynolds number was observed. Over the tested range, the deterioration in agreement between WPM and SPM was therefore more consistently associated with the onset of post-stall flow than with changes in Reynolds number.

- **Investigate potential discrepancies between WPM and SPM, with particular attention to the wall-pressure footprint and the applicability of existing potential-flow-based corrections across different flow regimes.**

  The post-stall discrepancies motivated further investigation into the wall-pressure footprint, revealing a downstream shift and reduction in magnitude of its pressure peak. Several empirical extrapolation methods were evaluated, but none consistently improved post-stall lift predictions. Notably, direct integration of the finite measured footprint produced estimates closer to SPM than the extrapolated distributions, a finding observed across the investigated Reynolds numbers.

  Reconsideration of the momentum balance suggested that a reversal in the differential wall-pressure contribution outside the measured domain could explain these results. However, this hypothesis could not be verified experimentally, and effects such as three-dimensional flow and transverse momentum transport may also contribute.

  The separated-wake model proposed by [44] demonstrated that such a pressure reversal is theoretically possible, but the model did not predict reversal for the experimental input conditions. Furthermore, extrapolation using the modelled pressure distributions did not yield reliable post-stall lift predictions.

  This objective was therefore partially achieved. Although potential mechanisms and limitations of the existing corrections were identified, the physical origin of the discrepancies remains unresolved and no reliable post-stall correction was obtained.

6

Recommendations

The present study has demonstrated that wall-pressure measurements can provide accurate lift predictions for a passive airfoil in the pre-stall regime. However, the post-stall regime remains challenging, as the observed discrepancies could not be adequately explained or corrected using the methods investigated.

Future research could therefore proceed in two directions. The first focuses on extending the application of WPM to suction-controlled bluff-body airfoils, as employed by Econowind. The second involves further investigating the physical mechanisms responsible for the post-stall discrepancies, with the aim of developing a reliable correction method.

6.1. Application to suction-controlled bluff-body airfoils

The fundamental principle underlying WPM, conservation of momentum, remains applicable to suction-controlled airfoils. Nevertheless, the introduction of suction modifies the control-volume momentum balance by introducing an additional flux of transverse momentum through the airfoil surface. For the simplified case in which suction is applied along the upper surface without additional blowing, the momentum balance introduced in Equation 2.1 can be extended to Equation 6.1.

$$\boxed{F_{y,\mathrm{wing}} + F_{y,\mathrm{walls}} = \int_{-w/2}^{w/2} \rho u_{\mathrm{out}} v_{\mathrm{out}}\, dy - \int_{-w/2}^{w/2} \rho u_{\mathrm{in}} v_{\mathrm{in}}\, dy + \int_{\mathcal{C}_{\mathrm{suction}}} \rho v(\mathbf{u}\cdot\mathbf{n})\, ds} \tag{6.1}$$

Here, $\mathcal{C}_{\mathrm{suction}}$ denotes the suction portion of the airfoil contour in the two-dimensional cross-section, and ds is the arc-length element along that contour. The unit normal $\mathbf{n}$ points out of the external-flow control volume and into the airfoil, so suction is treated as an outflow.

The Econowind wind tunnel is already equipped with an anemometer from which the volumetric suction flow rate can be determined. This measurement could also be used to estimate the additional momentum flux. Assuming uniform suction along the active span b, the volumetric suction flow rate per unit span is $\dot{V}' = \dot{V}/b$, where $\dot{V}$ is the total measured suction flow rate. If the suction velocity is also uniform along the suction contour and normal to the surface, its magnitude is $\dot{V}'/\ell_{\mathrm{suction}}$, where ℓ_{suction} is the arc length of the suction contour. The transverse momentum flux per unit span can then be approximated as follows, with n_y denoting the transverse component of the outward unit normal $\mathbf{n}$.

$$\int_{\mathcal{C}_{\mathrm{suction}}} \rho v\,(\mathbf{u}\cdot\mathbf{n})\ \mathrm{d}s \approx \rho \left(\frac{\dot{V}'}{\ell_{\mathrm{suction}}}\right)^2 \int_{\mathcal{C}_{\mathrm{suction}}} n_y\, \mathrm{d}s. \tag{6.2}$$

This approximation allows the suction contribution to be estimated from the measured volumetric flow rate and the known suction-surface geometry. However, non-uniform suction would require additional

information about the local velocity distribution. If blowing is also applied, its momentum contribution must be considered separately.

Consequently, the wall-pressure-based lift formulation developed for an impermeable airfoil cannot be applied directly to suction-controlled configurations without accounting for this additional momentum transport. Nevertheless, as long as suction maintains flow attachment, the wall-pressure response may remain comparable to that of a conventional airfoil in the pre-stall regime. Whether the existing corrections remain applicable under these conditions requires experimental validation. As the airfoil approaches stall and a separated wake develops, discrepancies similar to those observed in the present study may arise. Investigating the applicability of WPM under these conditions, and determining whether the suction contribution can be reliably incorporated into the existing methodology, therefore represents a relevant direction for future research.

6.2. Further investigation of post-stall discrepancies

Although several approaches were investigated to improve the accuracy of WPM in the post-stall regime, none provided a consistently reliable correction for the observed lift overprediction. Future research should therefore focus on establishing the physical mechanisms responsible for these discrepancies before attempting to develop further correction methods.

A first recommendation is to investigate the transverse momentum transported through the downstream boundary of the control volume. The present WPM formulation accounts for this contribution using a potential-flow-based correction. However, the development of a separated wake alters the downstream velocity field, potentially reducing the accuracy of this correction. Measurements of the downstream velocity field, for example using particle image velocimetry (PIV), could quantify the actual transverse momentum transport and determine whether inaccuracies in its prediction contribute to the observed lift discrepancy.

A second recommendation is to extend the wall-pressure measurements further upstream and downstream of the airfoil. This would provide a more complete representation of the pressure footprint and help establish whether negative contributions develop outside the currently measured region. Extending the control volume sufficiently far from the airfoil would also allow the validity of the two-dimensional flow assumption to be assessed indirectly. If the transverse momentum fluxes at the inlet and outlet become negligible, the integrated wall-pressure contribution should converge towards the lift determined from SPM. Agreement between the two methods would indicate that the neglected momentum contributions have no significant net effect, thereby supporting the two-dimensional approximation underlying the WPM formulation. Furthermore, the extended measurements would provide experimental validation for the extrapolation methods investigated in this study.

Finally, the separated-wake model investigated in subsection 4.5.4 could be extended to account for the confinement imposed by the wind-tunnel walls and the actual airfoil geometry. The present implementation assumes unbounded flow around an inclined flat plate, which limits its applicability to the experimental configuration. Incorporating these geometric effects could provide a more representative prediction of the wall-pressure distribution and further insight into the downstream pressure footprint. Although this approach could be pursued without additional experimental data, making it relatively straightforward to investigate, obtaining further measurements is considered more promising for identifying the underlying causes of the observed discrepancies.

References

[1] Ira H. Abbott, Albert E. von Doenhoff, and Louis S. Stivers. *Summary of Airfoil Data*. NACA Report 824. National Advisory Committee for Aeronautics, 1945. URL: https://ntrs.nasa.gov/citations/19930090976.

[2] Miguel Angel Aguirre et al. "Design of an external six-component wind tunnel balance with floating frame". In: *International Journal of Aerodynamics* 7.2 (2021), pp. 105–126. DOI: 10.1504/IJAD.2021.112709.

[3] H. Julian Allen and Walter G. Vincenti. *Wall Interference in a Two-Dimensional-Flow Wind Tunnel, with Consideration of the Effect of Compressibility*. NACA Report 782. National Advisory Committee for Aeronautics, 1944. URL: https://ntrs.nasa.gov/citations/19930091861.

[4] D. Althaus. *Measurement of Lift and Drag in the Laminar Wind Tunnel*. Institute of Aerodynamics and Gas Dynamics, University of Stuttgart. URL: https://www.iag.uni-stuttgart.de/dateien/pdf/laminarwindkanal_messtechniken/althaus_2.pdf.

[5] D. Althaus. *Tunnel-Wall Corrections at the Laminar Wind Tunnel*. Institute of Aerodynamics and Gas Dynamics, University of Stuttgart. URL: https://www.iag.uni-stuttgart.de/dateien/pdf/laminarwindkanal_messtechniken/althaus_1.pdf.

[6] John D. Anderson. *Fundamentals of Aerodynamics*. 5th ed. McGraw-Hill, 2010. ISBN: 9780073398105.

[7] Jewel B. Barlow, William H. Rae, and Alan Pope. *Low-Speed Wind Tunnel Testing*. 3rd ed. Wiley, 1999. ISBN: 9780471557746.

[8] Bundesarchiv. *Kiel, Flettner-Rotorschiff "Buckau"*. Photograph from the German Federal Archives. 1924. URL: https://commons.wikimedia.org/wiki/File:Bundesarchiv_Bild_102-00814,_Kiel,_Flettner-Rotorschiff_%22Buckau%22.jpg (visited on 04/23/2026).

[9] D. S. Bynum, R. L. Ledford, and W. E. Smotherman. *Wind Tunnel Pressure Measuring Techniques*. AGARDograph 145. Advisory Group for Aerospace Research and Development, 1970. DOI: 10.21236/AD0714565.

[10] Yunus A. Çengel and John M. Cimbala. *Fluid Mechanics: Fundamentals and Applications*. 3rd ed. McGraw-Hill Education, 2014.

[11] Bertrand Charrier et al. "Fondation Cousteau and windship propulsion 1980–1985: System Cousteau-Pechiney". In: *Journal of Wind Engineering and Industrial Aerodynamics* 20.1–3 (1985), pp. 39–60. DOI: 10.1016/0167-6105(85)90011-X.

[12] Jean-Jacques Chattot and Mohamed M. Hafez. *Theoretical and Applied Aerodynamics and Related Numerical Methods*. Dordrecht: Springer, 2015. ISBN: 978-94-017-9824-2. DOI: 10.1007/978-94-017-9825-9.

[13] Council of the European Union. *Fit for 55*. 2025. URL: https://www.consilium.europa.eu/en/policies/fit-for-55/#0 (visited on 12/02/2025).

[14] Currier & Ives. *Clipper ship Three Brothers, 2972 tons: The largest sailing ship in the world*. Hand-coloured lithograph. Library of Congress. 1875. URL: https://www.loc.gov/pictures/item/90716156/ (visited on 04/23/2026).

[15] Econowind. *Shipping can profitably reduce CO2 with VentoFoil wind support*. 2023. URL: https://econowind.nl/news/shipping-can-profitably-reduce-co2-with-ventofoil-wind-support/ (visited on 04/24/2026).

[16] Econowind. *VentoFoil Fuel Savings Calculator*. URL: https://econowind.nl/apps/calculator/ (visited on 04/24/2026).

[17] European Parliament and Council of the European Union. *Regulation (EU) 2023/1805 on the use of renewable and low-carbon fuels in maritime transport, and amending Directive 2009/16/EC*. 2023. URL: https://eur-lex.europa.eu/eli/reg/2023/1805/oj (visited on 11/01/2026).

[18] Kelly Hile. *CFD Modeling Meets Wind Tunnel Design... and the Rest is History*. Azore CFD Simulation Software Blog. URL: https://www.azorecfd.com/blog/cfd-modeling-wind-tunnel-design (visited on 05/14/2026).

[19] E. L. Houghton et al. *Aerodynamics for Engineering Students*. 7th ed. Oxford: Butterworth-Heinemann, 2017.

[20] International Maritime Organization. *EEXI and CII - ship carbon intensity and rating system*. URL: https://www.imo.org/en/mediacentre/hottopics/pages/eexi-cii-faq.aspx (visited on 12/02/2025).

[21] Eastman N. Jacobs and Albert Sherman. *Airfoil section characteristics as affected by variations of the Reynolds number*. Tech. rep. NACA Report 586. National Advisory Committee for Aeronautics, 1937. URL: https://ntrs.nasa.gov/citations/19930091662.

[22] E. C. Maskell. *A Theory of the Blockage Effects on Bluff Bodies and Stalled Wings in a Closed Wind Tunnel*. Reports and Memoranda 3400. Aeronautical Research Council, 1963. URL: https://reports.aerade.cranfield.ac.uk/handle/1826.2/3982.

[23] J. Mason et al. *A Global Fleet Under Wind: Scaling Wind Propulsion for Emission Reduction, Energy Demand and Equity*. Tech. rep. Tyndall Centre, 2026. URL: https://seas-at-risk.org/wp-content/uploads/2024/09/A-global-Fleet-Under-Wind_Seas_At_Risk-1.pdf.

[24] R. D. Mehta and P. Bradshaw. "Design rules for small low speed wind tunnels". In: *The Aeronautical Journal* 83.827 (1979), pp. 443–453. DOI: 10.1017/S0001924000031985.

[25] Sreevishnu Oruganti and Shreyas Narsipur. "Airfoil lift calculation using wind tunnel wall pressures". In: *Proceedings of the Institution of Mechanical Engineers, Part G: Journal of Aerospace Engineering* 236.8 (2022). First published online in 2021; assigned to a 2022 journal issue, pp. 1515–1531. DOI: 10.1177/09544100211038253.

[26] R. C. Pankhurst and B. Thwaites. *Experiments on the Flow past a Porous Circular Cylinder Fitted with a Thwaites Flap*. Reports and Memoranda 2787. Aeronautical Research Council, 1950. URL: https://reports.aerade.cranfield.ac.uk/handle/1826.2/3338.

[27] Ludwig Prandtl. "Über Flüssigkeitsbewegung bei sehr kleiner Reibung". In: *Verhandlungen des III. Internationalen Mathematiker-Kongresses in Heidelberg 1904*. Leipzig: B. G. Teubner, 1905, pp. 484–491.

[28] Jean-Paul Rodrigue. *Clipper Ships*. The Geography of Transport Systems. 2017. URL: https://transportgeography.org/contents/chapter1/emergence-of-mechanized-transportation-systems/clipper-ship/ (visited on 04/24/2026).

[29] Marija Samardžić et al. "External Six-Component Strain Gauge Balance for Low Speed Wind Tunnels". In: *Scientific Technical Review* 64.3 (2014), pp. 40–46. URL: https://www.vti.mod.gov.rs/ntp/rad2014/3-2014/6/f6.htm.

[30] Fulvio Scarano. "Particle Image Velocimetry". In: *Encyclopedia of Aerospace Engineering*. Ed. by Richard Blockley and Wei Shyy. Wiley, 2010. DOI: 10.1002/9780470686652.eae074.

[31] Hermann Schlichting and Klaus Gersten. *Boundary-Layer Theory*. 9th ed. Berlin, Heidelberg: Springer, 2016. ISBN: 9783662529195. DOI: 10.1007/978-3-662-52919-5.

[32] A. Sciacchitano et al. *Wind Tunnels*. 2024.

[33] Michael S. Selig et al. "Experiments on Airfoils at Low Reynolds Numbers". In: *34th Aerospace Sciences Meeting and Exhibit*. Reno, Nevada: American Institute of Aeronautics and Astronautics, 1996. DOI: 10.2514/6.1996-62.

[34] R. E. Sheldahl and P. C. Klimas. *Aerodynamic characteristics of seven symmetrical airfoil sections through 180-degree angle of attack for use in aerodynamic analysis of vertical axis wind turbines*. Tech. rep. SAND80-2114. Sandia National Laboratories, 1981. DOI: 10.2172/6548367.

[35] Tomas Sinnige. *(Subsonic) Wind Tunnels*. Lecture slides for AE4115 Experimental Simulations, Delft University of Technology. Unpublished lecture slides. Nov. 2023.

[36] Vincenzo Stornelli et al. "The Assessment of Wind Conditions by Means of Hot Wire Sensors and a Modifed Wheatstone Bridge Architecture". In: *Sensors and Actuators A: Physical* 262 (2017), pp. 130–139. DOI: 10.1016/j.sna.2017.05.005.

[37] Chakrit Suvanjumrat. “Comparison of turbulence models for flow past NACA0015 airfoil using OpenFOAM”. In: *Engineering Journal* 21.3 (2017), pp. 207–221. DOI: 10.4186/ej.2017.21.3.207.

[38] W. A. Timmer. “Two-dimensional low-Reynolds number wind tunnel results for airfoil NACA 0018”. In: *Wind Engineering* 32.6 (2008), pp. 525–537. DOI: 10.1260/030952408787548848.

[39] D. R. Troolin, E. K. Longmire, and W. T. Lai. “Time resolved PIV analysis of flow over a NACA 0015 airfoil with Gurney flap”. In: *Experiments in Fluids* 41.2 (2006), pp. 241–254. DOI: 10.1007/s00348-006-0143-8.

[40] Cameron Tropea. “Laser Doppler Velocimetry”. In: *Encyclopedia of Aerospace Engineering*. Ed. by Richard Blockley and Wei Shyy. Wiley, 2010. DOI: 10.1002/9780470686652.eae073.

[41] UIUC Applied Aerodynamics Group. *Low Reynolds Number Flow Visualization*. Web page. 2026. URL: https://m-selig.ae.illinois.edu/LRNFlowViz.html (visited on 05/19/2026).

[42] Wikipedia contributors. *Alcyone (1985 ship)*. 2025. URL: https://en.wikipedia.org/wiki/Alcyone_%281985_ship%29 (visited on 11/24/2025).

[43] S. Worasinchai, G. Ingram, and R. Dominy. “A low-Reynolds-number, high-angle-of-attack investigation of wind turbine aerofoils”. In: *Proceedings of the Institution of Mechanical Engineers, Part A: Journal of Power and Energy* 225.6 (2011), pp. 748–763. DOI: 10.1177/0957650911405411.

[44] T. Yao-Tsu Wu. “A wake model for free-streamline flow theory. Part 1. Fully and partially developed wake flows past an oblique flat plate”. In: *Journal of Fluid Mechanics* 13.2 (1962), pp. 161–181. DOI: 10.1017/S0022112062000609.

[45] Yuta Yamaguchi, Tomohisa Ohtake, and Akinori Muramatsu. “Pressure Distribution on a NACA0012 Airfoil at Low Reynolds Numbers”. In: *Proceedings of the 4th International Conference on Jets, Wakes and Separated Flows*. 2013, pp. 1201-1–1201-5. DOI: 10.1299/jsmeicjwsf.2013.4._1201-1_.

[46] Kianoosh Yousefi and Reza Saleh. “Three-dimensional suction flow control and suction jet length optimization of NACA 0012 wing”. In: *Meccanica* 50.6 (2015), pp. 1481–1494. DOI: 10.1007/s11012-015-0100-9.

[47] Gecheng Zha. *Fluid systems that include a co-flow jet*. European patent application EP3476720A1. Assignee: Coflow Jet LLC. European Patent Office. 2019. URL: https://patents.google.com/patent/EP3476720A1/en (visited on 04/24/2026).

Part II

Appendix

A

Potential-flow correction

The correction factors η_a and η_b introduced in subsection 2.4.1 are calculated using Equation A.1 and Equation A.2, respectively. Both factors depend on the function η_x, which describes the fraction of the integrated wall-pressure contribution captured by the finite pressure array for an elementary singularity located at position x along the airfoil chord. The resulting correction factors depend on the wind-tunnel geometry, the measurement region, and the position of the airfoil relative to the pressure array.

$$\eta_a = \int_0^c \frac{2}{\pi} \sqrt{\frac{1 - x/c}{x/c}}\, \overline{\eta}_x \, \frac{dx}{c} \tag{A.1}$$

$$\eta_b = \int_0^c \overline{\eta}_x \, \frac{dx}{c} \tag{A.2}$$

The function η_x is defined by Equation A.3, where x denotes the streamwise position of an elementary singularity relative to the airfoil mid-chord. The parameter w represents the distance between the wind-tunnel walls, while m and n denote the signed streamwise distances from the mid-chord to the first and last wall-pressure taps, respectively, with m being negative.

$$\eta_x = \frac{2}{\pi} \arctan\left(\frac{e^{-\pi x/w} \left(e^{\pi n/w} - e^{\pi m/w} \right)}{1 + e^{-2\pi x/w} e^{\pi (m+n)/w}} \right) \tag{A.3}$$

The values of m and n depend on the alignment of the airfoil relative to the pressure array. If the quarter-chord rather than the mid-chord is used as the alignment reference, the corresponding coordinate offset must be accounted for.

For the evaluation of Equation A.1 and Equation A.2, a coordinate transformation is required. The function η_x uses a mid-chord-centred coordinate system, defined over $[-c/2, c/2]$, whereas the integrals for η_a and η_b use a leading-edge-centred coordinate system over $[0, c]$. The shifted function $\overline{\eta}_x$ is therefore defined by Equation A.4.

$$\overline{\eta}_x = \eta_x \Big(x - \frac{c}{2} \Big) \tag{A.4}$$

The integrand of Equation A.1 exhibits an integrable singularity proportional to $x^{-1/2}$ as $x/c \to 0$. To avoid numerical difficulties associated with this behaviour, the substitution in Equation A.5 is applied.

$$\frac{x}{c} = \sin^2 \theta, \qquad dx = 2c \sin\theta \cos\theta \, d\theta \tag{A.5}$$

This transformation removes the singular behaviour at the leading edge and yields the smooth integrand in Equation A.6, which can be evaluated numerically.

$$\boxed{\eta_a = \frac{4}{\pi} \int_0^{\pi/2} \cos^2\theta \; \overline{\eta}_x|_{x=c\sin^2\theta} \; d\theta} \tag{A.6}$$

B

Wu separated-Wake model

The separated-wake model developed by Wu [44] is briefly introduced in subsection 4.5.1. The model provides analytical solutions for both fully and partially developed wakes surrounding an inclined flat plate. For a prescribed angle of attack α and wake underpressure, the corresponding conformal mapping relates the complex velocity variable w to the complex spatial coordinate $z = x + iy$, describing the position in the physical flow field. Since the mapping equations are extensive, they are presented separately in this appendix. The mappings for the partially and fully developed wakes are given by Equation B.1 and Equation B.2, respectively. The remaining parameters follow the definitions provided by Wu [44].

$$\begin{aligned}\frac{2\pi[z(w)+a_0]}{\Gamma} &= 2U(1-U^2)\sin\alpha\big[1+w^2-2wU\cos\alpha(1-\beta U\sin\alpha)\big]I(w)\\ &\quad+\beta\ln\big[(w-w_0)(w-\overline{w}_0)\big]-w_0(\beta w_0+2i)\ln\left(w-\frac{1}{w_0}\right)\\ &\quad-\overline{w}_0(\beta\overline{w}_0-2i)\ln\left(w-\frac{1}{\overline{w}_0}\right).\end{aligned} \tag{B.1}$$

$$\begin{aligned}z(w)+a_0 = \frac{f(w)}{w}+iB\Bigg[&\left(\frac{1}{\overline{w}_0}-\overline{w}_0\right)\left(\frac{1}{w_0}\ln(w-w_0)-w_0\ln\left(w-\frac{1}{w_0}\right)\right)\\ &-\left(\frac{1}{w_0}-w_0\right)\left(\frac{1}{\overline{w}_0}\ln(w-\overline{w}_0)-\overline{w}_0\ln\left(w-\frac{1}{\overline{w}_0}\right)\right)\Bigg].\end{aligned} \tag{B.2}$$

Here, $z = x + iy$ represents the complex spatial coordinate, while w denotes the normalized complex velocity. The angle of attack α and wake underpressure coefficient σ_{Wu}, derived from the estimated cavity pressure p_c, determine the flow configuration. The remaining parameters and auxiliary functions follow the definitions provided by Wu [44].

Part III

Literature study

C

Fundamentals of wind tunnel testing

Wind tunnels exist in many shapes and sizes and are designed for a wide range of applications. This chapter provides a brief overview of wind tunnel facilities and the main principles underlying wind tunnel testing. First, Appendix C.1 introduces the main categories of wind tunnel configurations. Next, Appendix C.2 describes the principal wind tunnel components and their functions. Appendix C.3 discusses the importance of flow similarity and the challenges associated with achieving representative test conditions. The chapter is finalised by Appendix C.4, which explains the required boundary corrections compensating for the difference between wind tunnel and unbounded flow.

C.1. Wind Tunnel Configurations

Wind tunnels can be divided into two main groups: open and closed circuit. [7]. The flow in an open wind tunnel, as depicted in Figure C.1, follows a straight line. Incoming ambient flow passes through a series of flow conditioning devices in the settling chamber, continuing through the contraction, after which it reaches the test section. A diffuser connects the test section to the driving system. Alternatively, an extra diffuser could be mounted after the driving system, behind which the flow leaves the system. The design is low in construction cost and space-efficient compared to the closed return type. Furthermore, the system is not sensitive to debris build-up [35].
A closed circuit wind tunnel utilizes the same components, but outflow is now redirected to the entrance of the wind tunnel by a shaft, as shown in Figure C.2. The drive system for this type is generally located in the return shaft of the wind tunnel. The biggest benefit of this type is the energy returns: the kinetic energy of the flow is reused, resulting in lower required energy input of the driving system. This means the flow in the system needs to be cooled since a continuous energy input by the driving system increases flow temperature. Closed return wind tunnels are silent and have low operational costs compared to the open return type. With this closed system, the flow is easier to control, resulting in higher flow quality.

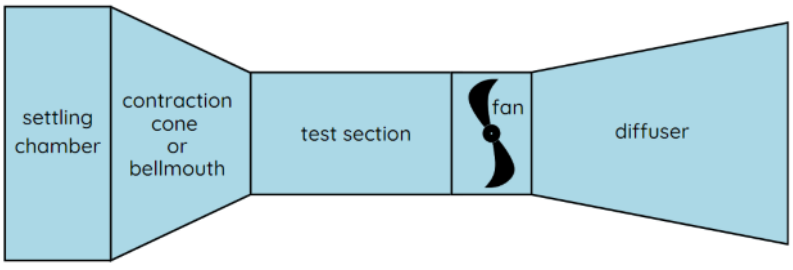


Figure C.1: Schematic of an open-circuit wind tunnel [18]

The second thing that characterises a wind tunnel is the test section configuration, for which again 2

main groups can be distinguished. In a closed test section, the model is surrounded by walls, whereas in an open test section, the model is not enclosed. Closed test sections are most commonly used for high-performance aerodynamic wind tunnels due to their clearly defined boundaries, allowing for precise application of boundary layer corrections. Corrections are required for both closed and open configurations to account for the bounded test conditions (Appendix C.4).

C.2. Main components of a wind tunnel

A wind tunnel consists of several components, each with a specific function. [24] and [7] describe the roles of these components for low-speed tunnels and propose design guidelines for each of them. As a practical example, the components of the TU Delft low-turbulence closed-return wind tunnel [32] are discussed in this section. Open-circuit wind tunnels use only a subset of these components, meaning the relevant elements are fully covered in this discussion.

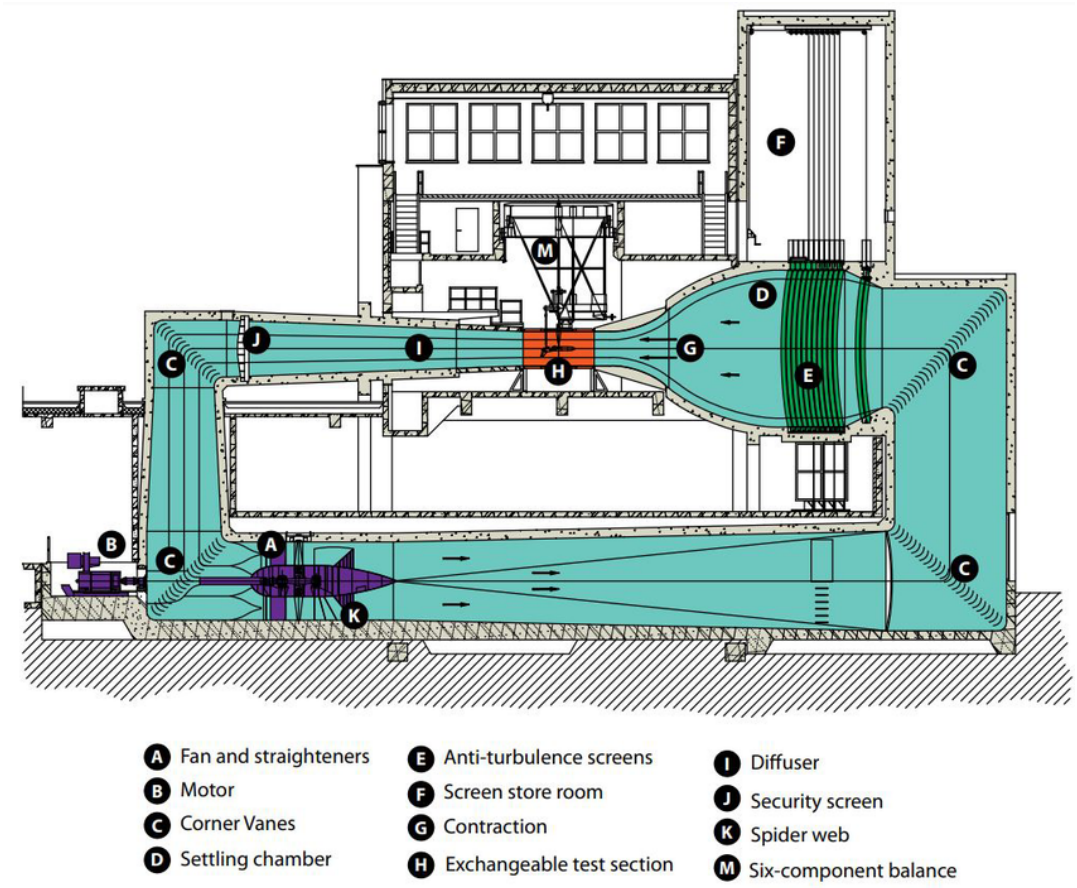


Figure C.2: TUDelft low turbulence wind tunnel [32]

Fan [A]. The fan is the driving part of the wind tunnel. It accelerates the flow to obtain the desired velocity in the test section. Axial fans are most commonly used for low-speed wind tunnels. Flow speed is then controlled by fan rpm and/or blade pitch. For higher speed open-loop facilities, pressurised air is released to reach speeds up to the supersonic regime. This drive system limits the operational window of these wind tunnels.

Motor [B]. The motor provides the shaft power required to drive the fan. For wind tunnels, the power associated with the flowing jet in the test section is defined by Equation C.1. This represents the kinetic energy flux of the flow passing through the test section at a given velocity. In practice, the required fan power exceeds the jet power due to total pressure losses in the tunnel, including wall friction, turning losses, screen losses, and other dissipative effects.

For closed-return wind tunnels, a significant portion of the flow energy is retained within the circuit, so the fan only needs to compensate for the losses rather than regenerate the full jet power each cycle. This effect is commonly expressed using the energy ratio, which is typically between 3 and 7. Consequently, the required fan power is approximately one-third to one-seventh of the jet power, before accounting for component efficiencies. To obtain the required motor power, the mechanical efficiency of the fan motor system must also be considered.

$$P = \dot{E} = \frac{1}{2}\dot{m}V_\infty^2 = \frac{1}{2}\rho A V_\infty^3 \tag{C.1}$$

Corner vanes [C]. Corner vanes are used in the corners of the duct to deflect the flow. Corner vanes are mostly built from thin metal sheets. For larger wind tunnels, airfoil sections are used, focusing on robustness rather than aerodynamic efficiency. In usual practice, corner vane implementation focuses on shape and spacing. The gap-to-chord ratio should not exceed a value of 0.25, with gap distance being defined as the distance between the leading edges of the vanes. Typically, a quarter circle shape is adopted with slightly extruded leading and trailing edges. The trailing edge points directly downstream, and the leading edge generally has a slightly positive angle of attack.

Settling chamber[D]. In this chamber, the flow straightening devices are located. The chamber should be big enough to provide sufficient spacing between these devices. In this part of the wind tunnel, the speeds are lowest due to the big cross-section, allowing optimal flow conditioning before the contraction.

Flow straightening devices [E]. The most common flow straightening devices used in wind tunnels are honeycombs and screens. Honeycombs reduce lateral velocity components by guiding the flow in the streamwise direction, thereby suppressing large-scale transverse motions. When properly dimensioned, they also contribute to turbulence reduction. Anti-turbulence screens mainly improve longitudinal velocity uniformity by imposing a static pressure drop proportional to the square of the local velocity $\Delta p \propto U^2$. Regions with higher velocity, therefore, experience larger pressure losses than slower regions. This creates pressure gradients that redistribute momentum within the flow, reducing velocity non-uniformities and producing a more uniform velocity profile downstream.

Spacing between screens should be carefully determined such that static pressure has time to recover before reaching the next screen. For optimal turbulence reduction, the spacing between screens should furthermore be in the order of the largest eddies to allow for sufficient breakdown space. A spacing of 0.2 settling chamber diameter has proven to be sufficient in most cases.

Screen storage room [F]. This section is used to store interchangeable screens, allowing quick replacement and adjustment of the flow-conditioning configuration for different operating conditions and experimental requirements.

Contraction [G]. The contraction is a converging section that accelerates the flow from the settling chamber into the test section. The relatively low velocity in the settling chamber limits pressure losses in the upstream components. As the flow accelerates in the contraction, the turbulence intensity decreases because the mean velocity increases, with absolute velocity fluctuations remaining approximately constant. Turbulence intensity is defined as in Equation C.2

$$TI = \frac{u'}{U} \tag{C.2}$$

Additionally, spatial velocity non-uniformities across the flow are reduced, resulting in a more uniform velocity field in the test section. Typical aerodynamic wind tunnels employ contraction ratios between 6 and 9 to achieve high flow uniformity and low turbulence intensity. A short contraction is preferred for space and cost considerations. However, the contraction must be sufficiently long and smoothly contoured to prevent boundary layer separation.

Test section [H]. This is where the model and most of the instrumentation are located. The combination of flow straightening devices and contraction assures sufficient flow quality and minimal boundary layer effects in this section for accurate testing. The test duct can have different cross-sectional shapes:

rectangular, oval, or octagonal. Shapes with straight walls are often preferred since this makes the installation of models easier. Some test sections adopt a slightly diverging cross-section to compensate for boundary layer growth along the walls. In specific cases, wind tunnel walls are ventilated or adaptive to allow for boundary condition control.

Diffuser [I]. The function of the diffuser is to gradually convert the dynamic pressure of the flow in the test section into static pressure by decelerating the flow. In closed-return wind tunnels, this slows the flow before it enters the return duct, thereby reducing energy losses in the circuit. In open-return wind tunnels, the diffuser reduces the kinetic energy discharged into the surrounding atmosphere, which also improves the overall energy efficiency of the tunnel.

Security screen [J]. A security screen is installed downstream of the test section to prevent loose components or debris from entering the fan or other parts of the wind tunnel circuit.

Spider web [K]. The spider web structure consists of radial struts that support the fan and its shaft within the duct.

Balance [L]. For this specific set-up, data are obtained using a 6-degree balance system. A set of 6 load cells is used to measure the forces acting on the model and derive performance parameters. Measurement techniques differ per setup. A detailed overview of all measuring techniques used in wind tunnels is given in Appendix D.

Heat exchanger. Because the fan continuously adds energy to the flow, the air temperature in a closed-circuit wind tunnel gradually increases. To ensure consistent test conditions, the temperature must be maintained at a nearly constant level, which is achieved using heat exchangers. Cooling is commonly implemented in the settling chamber or diffuser, or by using cooled turning vanes.

C.3. Flow similarity

One of the biggest challenges in wind tunnel testing is obtaining results that can be translated to full-scale models. Flow phenomena change when models are tested on smaller scales with deviant flow speeds. This section describes how flow similarity parameters follow from non-dimensionalising the governing equations, including their relevance to aerodynamic testing.

C.3.1. Governing equations

To fully describe a flow, six scalar variables are required: p, **V**, ρ, and T [7]. To solve for these variables, a set of six equations is required, of which the first five are in the form of conservation laws. Equation C.3 describes the conservation of mass in a domain. In standard continuum mechanics, mass can not be created nor destroyed, leading to this first relation. The same holds for momentum as explained by Equation C.4. These so–called Navier–Stokes equations consist of three coupled partial differential equations representing conservation of momentum in the three spatial directions. Together with the continuity equation, they form the governing equations for viscous fluid flow. Equation C.5, the energy equation, completes the set of conservation laws.

$$\frac{\partial \rho}{\partial t} + \nabla \cdot (\rho \mathbf{V}) = 0 \tag{C.3}$$

$$\rho \left(\frac{\partial \mathbf{V}}{\partial t} + (\mathbf{V} \cdot \nabla)\mathbf{V} \right) = \rho \mathbf{g} - \nabla \left(p + \frac{2}{3}\mu \nabla \cdot \mathbf{V} \right) + 2\nabla \cdot (\mu \dot{\mathbf{S}}) \tag{C.4}$$

$$\begin{aligned} \rho \frac{\partial}{\partial t} \left(C_v T + \frac{V^2}{2} \right) + \rho \mathbf{V} \cdot \nabla \left(C_v T + \frac{V^2}{2} \right) &= \rho \mathbf{g} \cdot \mathbf{V} - \nabla \cdot (p\mathbf{V}) \\ + \nabla \cdot \left[2\mu \nabla \left(\frac{V^2}{2} \right) + \mu (\nabla \times \mathbf{V}) \times \mathbf{V} - \frac{2}{3}\mu (\nabla \cdot \mathbf{V})\mathbf{V} + k \nabla T \right] & \end{aligned} \tag{C.5}$$

The system is closed by the conservation equations and the equation of state (Equation C.6) only if the caloric and transport properties are assumed constant. If this is not the case, additional relations such as Sutherland's law (Equation C.7) are required. These extra relations define the behaviour of

the internal energy, viscosity, and thermal conductivity. Different relations exist, ranging from simple temperature-dependent relations to high-accuracy models.

$$p = \rho R T \tag{C.6}$$

$$\mu = \mu_{\text{ref}} \left(\frac{T}{T_{\text{ref}}} \right)^{3/2} \frac{T_{\text{ref}} + S}{T + S} \tag{C.7}$$

The total set of equations requires a set of boundary conditions to calculate a unique flow solution. The set of equations is generally too complicated to be analytically applied to problems. When valid, the following assumptions can drastically simplify the set:

- **Incompressible flow:** This indicates constant flow density throughout the field. All spatial and time derivatives of ρ can be left out of the equations
- **Inviscid flow:** The flow viscosity is assumed to be zero. All terms including μ can be ignored.
- **Steady flow:** The flow does not change over time. This means all time derivatives can be left out of the conservation equations.

Due to the complex behaviour of flows where these assumptions are invalid, solutions of this set of equations are generally obtained with CFD analyses.

C.3.2. Non-dimensionalization

To compare the behaviour of scaled models with in-field systems, such as airplane flow similarity, is desired. The first step in understanding flow similarity is non-dimensionalising the conservation equations. To do so, every variable is defined as the ratio between that variable and a defined reference value. Following the non-dimensionalisation procedure described in [7], the variables are defined as in Equation C.8.

$$\mathbf{r} = l\hat{\mathbf{r}}, \quad t = \left(\frac{l}{V_\infty} \right) \hat{t}, \quad \mathbf{V} = V_\infty \hat{\mathbf{V}}, \quad \rho = \rho_\infty \hat{\rho}, \quad T = T_\infty \hat{T}, \quad \mu = \mu_\infty \hat{\mu}, \quad p - p_\infty = \frac{1}{2} \rho_\infty V_\infty^2 c_p \tag{C.8}$$

Substituting these definitions in Equation C.3 - Equation C.5 results in the non-dimensionalized conservation equations. When the reference values are then clustered in each term, a set of dimensionless coefficients arises. In the momentum equation, these are the Froude and Reynolds numbers as defined in Equation C.9 and Equation C.10 respectively. The first describes the ratio between inertia forces and gravitational forces. The Froude number becomes a relevant parameter when free surfaces are present in the flow field or when unsteady boundary layer conditions are present. This is generally not the case in wind tunnel testing. The Reynolds number expresses the ratio of inertial to viscous forces and is the key parameter determining the flow regime and its behaviour. For wind tunnel experiments where the Mach number (Equation C.11) is smaller than 0.3 this scaling parameter is the most important.

$$Fr = \sqrt{\frac{V_\infty^2}{lg}} \tag{C.9}$$

$$Re = \frac{\rho_\infty V_\infty l}{\mu_\infty} \tag{C.10}$$

From non-dimensionalizing the energy equation, two more coefficients appear. The Mach number in Equation C.11 is defined as the ratio between the flow speed far upstream and the speed of sound. Its value becomes important when compressibility effects can no longer be neglected (generally above M=0.3). The Prandtl number (Equation C.12) is a parameter solely dependent on the state of the

flow. It describes the ratio between the viscous and thermal boundary layer and is thus temperature dependent.

$$M = \frac{V_\infty}{a} \tag{C.11}$$

$$Pr = \frac{\mu c_p}{k} \tag{C.12}$$

Besides the non-dimensional parameters used to describe the operating conditions, the aerodynamic forces and moments are also non-dimensionalised. For a two-dimensional airfoil, aerodynamic performance is commonly expressed using the lift, drag, and moment coefficients per unit span, defined as

$$C_l = \frac{L'}{\frac{1}{2}\rho U_\infty^2 c} \tag{C.13}$$

$$C_d = \frac{D'}{\frac{1}{2}\rho U_\infty^2 c} \tag{C.14}$$

$$C_m = \frac{M'}{\frac{1}{2}\rho U_\infty^2 c^2} \tag{C.15}$$

Three-dimensional effects are not considered here, as the present study focuses on airfoil behaviour that is assumed to be uniform along the span. These coefficients can also be obtained by integrating the pressure coefficient and shear stress coefficient distributions over the surface of the body. The resulting forces are resolved parallel to the freestream direction to obtain the drag coefficient and perpendicular to the freestream direction to obtain the lift coefficient, while the moment coefficient is determined by taking the moment of these forces about the chosen reference point. The aerodynamics of airfoils is discussed further in detail in Appendix E.

From the similarity analysis, it follows that the aerodynamic coefficients are, in general, functions of several nondimensional parameters, including the angle of attack, Reynolds number, Mach number, and nondimensional time. However, for steady, low-speed, two-dimensional airfoil testing, compressibility and unsteady effects can be neglected, and the aerodynamic coefficients primarily depend on the angle of attack and Reynolds number. For a fixed airfoil geometry, this relation can be formulated as in Equation C.16.

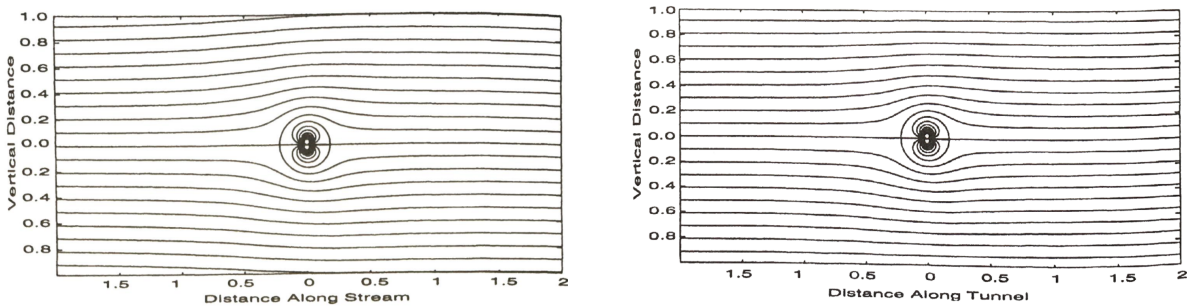
$$C = f(\alpha, Re) \tag{C.16}$$

Since the desired angle of attack is set directly during testing, the main difficulty in achieving similarity between model and full-scale conditions lies in matching the Reynolds number.

C.4. Wind tunnel wall interference

Even when the relevant similarity parameters are matched as closely as possible, wind tunnel measurements do not fully represent unbounded flow conditions. The presence of the wind tunnel itself alters the flow around the model. Both open and closed test sections impose artificial boundary conditions that differ from free-flight conditions, affecting the measured aerodynamic forces and moments. Correction factors are therefore required to relate wind tunnel measurements to equivalent free-air conditions.

The difference between the unbounded flow field around a cylinder and the flow around a cylinder in a closed wind tunnel test section is illustrated in Figure C.3. It can readily be observed that, in the unbounded case, the streamline curvature extends toward the top and bottom of the domain. In the bounded case, however, the streamlines are forced to follow the wind tunnel walls. This phenomenon is called *streamline curvature* and should be corrected for.



(a) Unbounded case **(b)** Bounded case

Figure C.3: Potential flow solution of a cylinder with wake [7].

Other wall-imposed effects do not directly appear in the streamline pattern and mainly affect local flow velocities. *Solid blockage* is the increase in local flow velocity caused by the flow restriction imposed by the model, resulting in higher lift and drag forces. Similarly, the velocity deficit in the wake causes the flow outside the wake to increase in velocity, an effect called *wake blockage*.

Buoyancy is the final effect of the wind tunnel wall on the model. It results from the growing boundary layer along the wind tunnel walls, which effectively decreases the test section area along its length. This creates a positive velocity gradient and therefore a negative pressure gradient throughout the test section. As a result, the model is pushed forward, decreasing the measured drag.

Different correction procedures have been developed to account for these wall-interference effects, depending on the test-section configuration, model geometry, blockage ratio, and measurement approach [7]. For wall pressure measurement methods specifically, additional relations are required to convert the measured wall pressure distribution into aerodynamic force coefficients [5, 25]. The specific correction procedure adopted in the Econowind wind tunnel is therefore not discussed in detail here, but is introduced in section 2.4, where the performance-parameter calculation method is described.

D

Instrumentation and measurement techniques

A great variety of instrumentation is used when it comes to wind tunnel testing. Instrumentation is typically classified according to the quantity it measures. Balance systems, as described in Appendix D.1, directly measure force components. Other instrumentation is used to strictly measure local velocity (Appendix D.2) and pressure (Appendix D.3) in the flow field. Flow visualisation also plays a significant role in identifying flow field characteristics. Different approaches for this are discussed in Appendix D.4. This chapter provides an overview of existing instrumentation and measurement techniques, establishing a basis for selecting suitable methods for the present research.

D.1. Force and moment measurements

[29] describes the use of balance systems in wind tunnel testing. A balance system is a device used to measure the aerodynamic forces acting on a model in a wind tunnel by means of strain gauges. Two main configurations can be distinguished: internal and external balance systems.

An internal balance system is located inside the wind tunnel, where the model is directly connected to a set of supporting struts containing strain gauges used to measure the aerodynamic loads. When an external balance system is used, the model is mounted on a support on a disc that is flush with the wind tunnel wall, as shown in Figure D.1. The platform is then connected to the force-measuring devices.

A balance system contains multiple strain gauges arranged in specific orientations. The number of

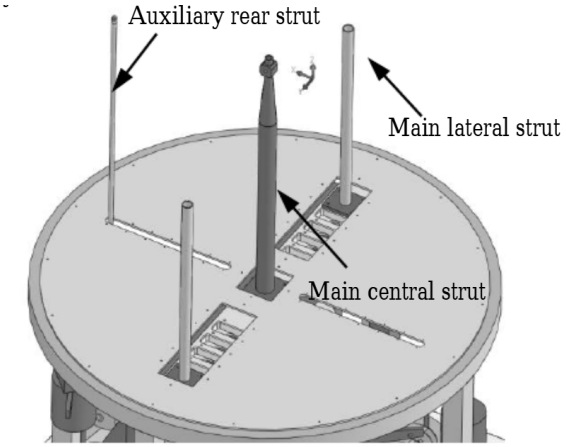


Figure D.1: Balance platform with balance beneath [2]

gauges and their alignment determine which independent force and moment components can be resolved, typically allowing the measurement of three force and three moment components acting on the model.

The load cells are commonly stainless-steel S-shaped elements whose working principle is based on elastic deformation under load. The applied force causes bending of the load cell, where strain gauges are mounted. Typically, four strain gauges are arranged in a Wheatstone bridge configuration to allow accurate determination of the applied force. The deformation of the strain gauges results in a change in electrical resistance, producing a measurable voltage signal. After calibration, this signal can be related to the deformation of the load cell and consequently to the applied force.

A crucial design step in setting up a reliable force balance system is the calibration. Calibration is typically carried out by applying forces and moments of known magnitude. The measured force outputs are then compared to the theoretically expected outputs. For optimal calibration, not only isolated forces and moments should be tested, but also combined loads should be investigated.

D.2. Velocity measurements

This section outlines the main techniques available for measuring flow velocity in wind-tunnel experiments. Several methods exist, each based on a different measurement principle and suited to specific flow conditions and accuracy requirements. In this work, velocity measurements are discussed for Pitot-static tubes, hot-wire anemometry (HWA), particle image velocimetry (PIV), and laser Doppler velocimetry (LDV). The working principles, main advantages, and limitations of each technique are briefly described.

D.2.1. Pitot-static tubes

A Pitot-static tube is a device consisting of a set of pressure ports, as shown in Figure D.2. The total pressure port is oriented in the flow direction, causing the flow to stagnate at the opening. This port measures the stagnation pressure, also referred to as the total pressure. The total pressure consists of a static and a dynamic component, as given in Equation D.1.

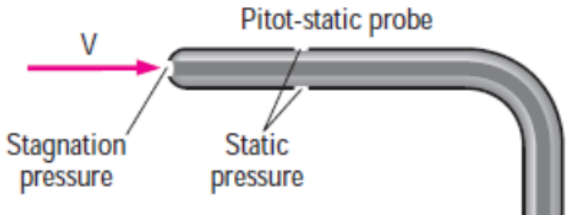


Figure D.2: Pitot-static tube [10]

One or more static pressure ports are located on the side of the tube, where the flow is not disturbed by stagnation. The difference between the total pressure and the static pressure is used to determine the local flow velocity. Pitot-static tubes are typically designed as slender probes to minimise flow disturbance and measurement error. The shape of the nozzle is chosen according to the Mach regime the tube operates in. Pressure measurements are described in more detail in Appendix D.3.

$$p_0 = p + \frac{1}{2}\rho U^2 \tag{D.1}$$

D.2.2. Hot-wire anemometry

HWA uses very thin wires, as shown in Figure D.3, to measure flow velocity. The fragile wire is supported by two struts and is located at the end of a probe to minimise flow disturbance. The working principle is based on an energy balance of the heated wire. The flow passing the wire cools it through convective heat transfer, while an imposed electrical current heats it. The energy balance described

by Equation D.2, where W is the heat produced by the Joule effect, and H is the heat removed from the wire by the passing flow.

$$\frac{dE_{th}}{dt} = W - H \tag{D.2}$$

A single hot wire can only measure the velocity component perpendicular to the wire. To determine multiple velocity components, multiple wires arranged at different orientations are required. Depending on the configuration, two- or three-component velocity measurements can be obtained. Two different operating modes can be distinguished: constant temperature anemometry (CTA) and constant current anemometry (CCA).

For CTA, the temperature of the hot wire is kept constant by adjusting the electrical current supplied to the wire. The wire is part of a Wheatstone bridge circuit, in which the resistance of the heated wire is continuously monitored. Since the electrical resistance of the wire depends on its temperature, a change in flow velocity alters the cooling of the wire and causes the Wheatstone bridge to become unbalanced. A feedback amplifier then adjusts the current through the wire to restore the bridge balance, thereby maintaining a constant wire temperature. The required current needed to maintain this equilibrium is related to the local flow velocity.

CTA provides a higher frequency response than CCA because the feedback circuit keeps the wire temperature nearly constant, reducing the influence of the thermal inertia of the wire. As a result, CTA is well-suited for measurements involving small time scales and rapidly fluctuating flow. The governing energy balance equation for this process follows from Equation D.2 and is given in Equation D.3. A, B, and n are unknown parameters that are determined by a calibration procedure. During calibration, a series of known flow velocities is applied to the CTA. For each velocity, the required current is measured, producing a current–velocity scatter plot. Equation D.3 is subsequently used to fit a calibration curve to the data.

$$E^2 = A + BU^n \tag{D.3}$$

In CCA, the electrical current through the wire is kept constant, while the wire temperature is allowed to vary in response to changes in the flow velocity. The governing behaviour therefore follows directly from the transient energy balance given in Equation D.2, without the constant-temperature simplification used in CTA. As a result, the response of a CCA system is more strongly influenced by the thermal inertia of the wire. Due to the time-dependent behaviour of the governing equation, calibration is performed using a known dynamic velocity input.

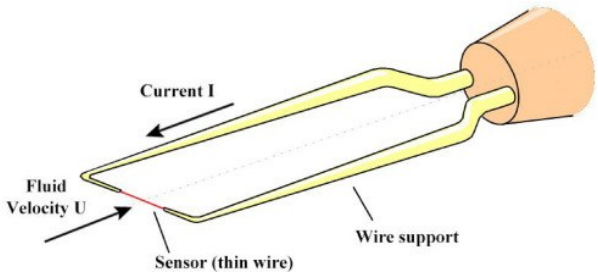


Figure D.3: Hot wire anemometer [36]

It should be noted that the calibration factors are temperature dependent, and measurements should therefore be performed at the same temperature as used during calibration. In practice, hot-wire probes are often calibrated over a range of temperatures to ensure accurate measurements under different testing conditions.

D.2.3. Particle Image Velocimetry

PIV is a non-intrusive optical measurement technique used to determine velocity fields in a flow. The method relies on tracer particles that are introduced into the flow and illuminated by a laser sheet. The

local flow velocity is obtained by evaluating the displacement of these tracer particles over a known time interval. This relation is expressed in Equation D.4.

$$\mathbf{V} = \frac{\Delta \mathbf{X}}{\Delta t} \tag{D.4}$$

Compared with point-based techniques such as HWA and LDA, the main advantage of PIV is that it provides an instantaneous velocity vector field over a planar domain. This makes the method useful when spatial flow structures, such as separation regions, wakes or vortices, need to be identified. A drawback is its lower temporal resolution compared with HWA and LDA. HWA can reach measurement rates up to approximately 100 kHz, while LDA typically provides data rates in the order of $1{-}10$ kHz. Standard PIV systems typically operate at much lower repetition rates, although high-speed PIV systems can reach rates up to approximately 10 kHz. Online PIV evaluation is generally slower and may be limited to approximately one velocity field per second [30].

The full setup required for PIV is depicted in Figure D.4. Small tracer particles are introduced into the flow, either as liquid droplets or solid particles. Liquid droplets can be generated using atomizers or fog machines, while solid particles can be produced by burning incense sticks or by entraining particles from a fluidized powder bed. The particles must be small enough to accurately follow the flow, but large enough to scatter sufficient light for imaging. Particle selection is therefore based on a trade-off between flow-tracking accuracy and image visibility.

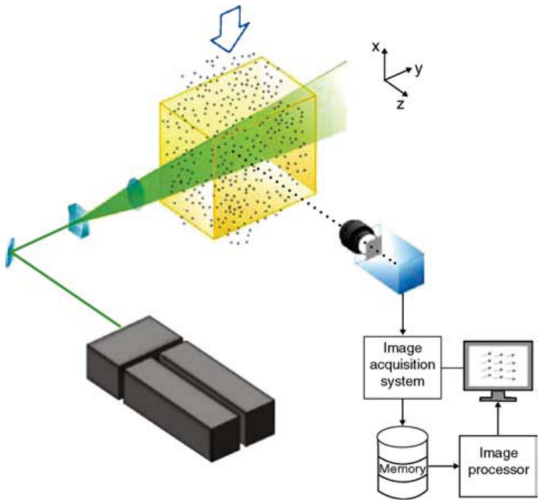


Figure D.4: Typical PIV setup for a two-component velocity measurement [30].

The measurement plane is illuminated by a laser sheet. This light sheet is formed by directing the laser beam through a series of optical lenses, producing a thin illuminated plane in the flow. Solid-state lasers are commonly used because they can produce short, high-energy light pulses. A commonly used laser type is the frequency-doubled Nd:YAG laser, which emits light at a wavelength of 532 nm. Such systems typically produce pulse energies in the range of $20{-}400$ mJ, with pulse durations below 10 ns.

The optical part of the setup consists of one or more cameras used to record the illuminated tracer particles. The camera lens is characterised by its focal length f, aperture diameter D, f-number $f\#$, and image magnification M. The f-number is defined as

$$f\# = \frac{f}{D} \tag{D.5}$$

The particle image diameter depends on both the geometric image of the particle and the diffraction-limited spot diameter. The diffraction-limited spot diameter is given by

$$d_{\text{diff}} = 2.44\lambda f\#(1+M), \tag{D.6}$$

where λ is the laser wavelength. Increasing the f-number reduces the aperture size and therefore increases diffraction blur, which enlarges the particle image diameter. In practice, this must be balanced against the reduced amount of collected light.

The recorded images are post-processed to obtain the velocity vector field. The two recorded frames are divided into interrogation windows, each containing a group of tracer particles. The particle patterns in corresponding interrogation windows from two subsequent frames are compared using cross-correlation. The displacement corresponding to the highest correlation peak represents the average particle-image displacement within the interrogation window. After applying the appropriate image scaling and dividing by the known time interval between the laser pulses, the local flow velocity is obtained.

D.2.4. Laser Doppler Velocimetry

Laser Doppler velocimetry (LDV) is a different non-intrusive method of determining flow velocity [40]. The method determines the velocity of a single point in the flow up to three components, depending on the setup. The technique is less suitable for visualising entire flow fields but is favourable for analysing turbulent flows due to the high temporal and spatial resolution.

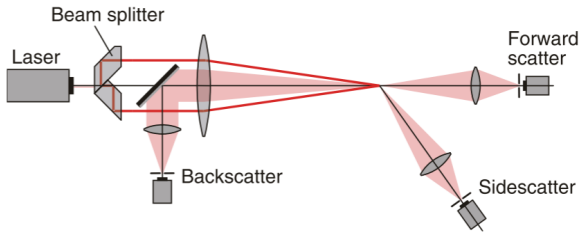


Figure D.5: Laser Doppler Velocimetry setup for different aperture placements

A laser is split into two beams, each directed to a focal point from a different angle (Figure D.5). The lasers illuminate particles in the flow just as for PIV. The particles moving through the focal point scatter this light, which is collected by an aperture and a photodetector. The photon detector measures the frequency difference of the scattered light originating from the two different laser rays, called the beat frequency. This difference (f_D) can be directly related to the velocity of the particle in the direction of the photon detector (U_x) as Equation D.7 shows. Only Θ, the full angle between the two different laser beams, and λ, the wavelength of the laser beam, are needed to determine the directional speed of the particles.

$$f_D = \frac{2U_x \sin(\Theta/2)}{\lambda} = \frac{U_x}{\Delta x} \tag{D.7}$$

D.3. Pressure measurements

The use of pressure taps was briefly introduced in subsection D.2.1 in the context of pitot-static tube velocity measurements. In this section, pressure measurements are discussed in more detail, focusing on the measurement principle and their applications in wind tunnel testing.

D.3.1. Measurement principle and hardware

Pressure measuring requires a pressure transducer and tubing that connects these to the desired pressure measurement location. The setup is depicted in Figure D.6. Short tubing is only desired when quick response times drastically reduce the operational cost (short-duration facilities) of the wind tunnel, or when unsteady pressures are to be measured [9]. This means generally tubing length is not critical, meaning pressure transducers are located outside of the wind tunnel. This means the setup time and costs for swapping models are minimised, and a single transducer suffices, which

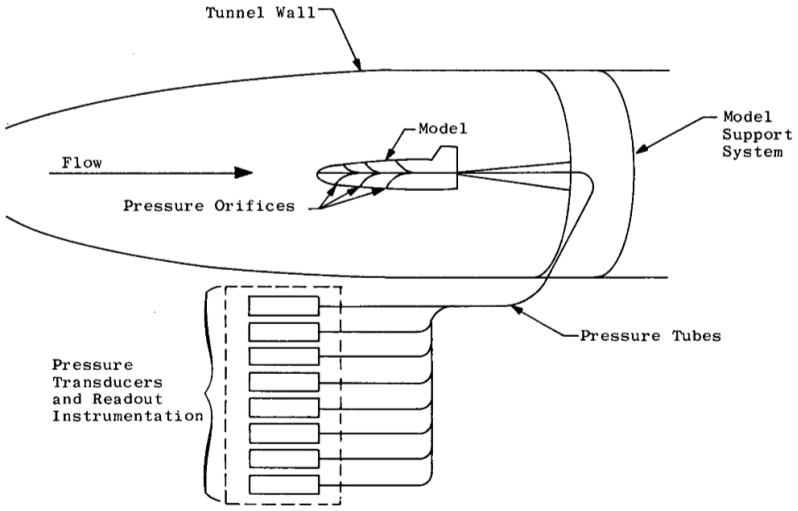


Figure D.6: Setup for surface pressure measurement on a wind tunnel model [9]

can be connected to different pressure ports. Vibrations of the transducers should be prevented to ensure accurate measurements. For steady pressure measurements, during installation, the main focus should be on preventing pressure leakage in the circuit from the pressure tap to the transducer. When fast response times are desired, new challenges are introduced. Pressure transducers should be directly connected to the pressure tap or with sufficiently short tubing. The transducers are now more prone to damage due to debris in the flow, and the sensor is now sensitive to any heating originating from the flow. To prevent this, the exposed transducer can be protected by means of a silicone layer. This postpones the heating of the transducer until after pressure measurements are carried out.

D.3.2. Applications in wind tunnel testing

Pressure measurements are applied in several ways in wind tunnel testing. The most used application is the integration of pressure taps in a model. For airfoil testing, the circumferential pressure profile is measured and non-dimensionalised as shown in Equation D.8 to obtain pressure coefficients. Integrating the pressure coefficients in the lift and drag direction results in aerodynamic coefficients of interest: lift coefficient and drag coefficient.

$$C_p = \frac{p - p_\infty}{\frac{1}{2}\rho U_\infty^2} \tag{D.8}$$

Another approach integrates pressure taps in wind tunnel walls as discussed in [25]. The approach is based on the conservation of momentum and the predictability of the axial velocity entering and leaving the test section. This means the pressure applied to the model by the flow is equal and opposite in sign to the pressure the wind tunnel walls apply to the flow. A streak of pressure taps on the walls can thus be used to obtain lift coefficients of 2D models. A typical wall pressure measurement (WPM) setup is shown in Figure 2.6. Since the pressure tap range is finite and the pressure field introduced by a lifting body is theoretically infinite, correction factors are required to translate this pressure to model pressure, which are discussed in the same section.

D.4. Flow visualisation

Since most fluids and air, particularly for wind tunnel testing, are transparent, flow visualisation is a convenient approach towards understanding flow physics. Visual inspection reveals flow behaviour and is a relatively inexpensive approach. Drawbacks are that the approach can only be used for qualitative analyses and is generally intrusive. This section describes the most commonly used techniques.

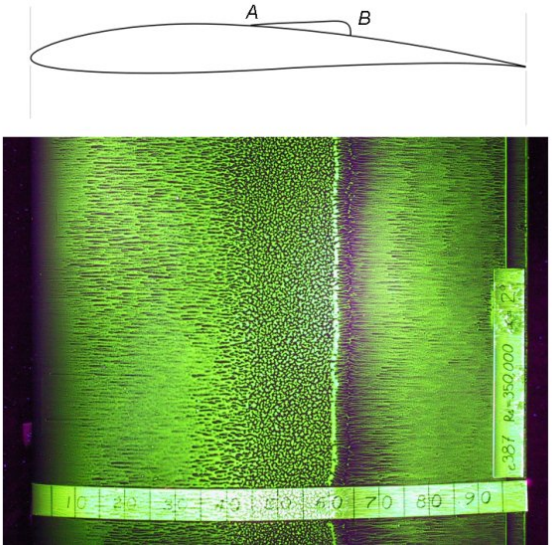


Figure D.7: Oil-flow visualisation of a laminar separation bubble on an E387 airfoil. Point A indicates laminar separation, and point B indicates reattachment [41].

D.4.1. Oil flow visualisation

Oil can be used to visualise the interaction of air flow with the surface of a body. It can be used to identify flow separation, transition, and reattachment, or to identify streamlines over the surface. The surface is coated with a thin, often fluorescent layer of oil to maximise visibility. To identify flow-regime behaviour, the full surface is covered with oil. Spatial variations in oil accumulation can then be observed at locations of separation, transition or reattachment. Figure D.7 shows an example of how these regimes can be identified. Local oil accumulation or removal occurs due to changes in wall shear stress. In laminar flow, momentum exchange between flow layers is limited, so the oil layer is only weakly affected by shear. Once the flow becomes turbulent, momentum exchange increases, resulting in higher wall shear stress and stronger oil displacement. Similar changes in wall shear stress occur at separation and reattachment locations. These locations therefore appear as distinct bright and dark lines on the surface.

Oil can also be used to identify surface streamlines. In this approach, oil drops are distributed over the surface and are swept in the local flow direction, revealing the surface-flow pattern. This method is mainly suitable for steady flows, since strongly unsteady or turbulent behaviour does not produce a consistent oil-track direction.

D.4.2. Wall-tufts

Wall tufts are lightweight, flexible pieces of string connected to a surface. They are used to indicate attached or separated flow. When flow is attached, the tufts give an indication of the flow direction, whereas for turbulent and separated flow, they show restless behaviour. It should be noted that due to their weight, the real flow direction generally has a small offset angle. The benefit is that they are simple and cheap to implement and can be used on complex 3D surfaces. However, tufts create surface roughness and therefore contribute to flow transition.

D.4.3. Smoke and dye

Dye is used for liquid flow studies, whereas smoke is used for gas studies, in this case, air. The smoke is released into the flow by an emitter and carried away by the medium. The emitter should be installed such that intrusion is minimised, meaning flush installation and little mass and momentum input. Smoke visualisation is only applicable when little turbulent diffusion is present. Smoke emitted from a single point visualises streamlines for laminar flows. For turbulent flow, the smoke follows streaklines. Streaklines show all flow particles that have passed a certain location, in this case, the emission location. When a smoke rake is used with periodic smoke emission, timelines can also be identified. These are all points in the flow that passed a certain surface at the same moment.

E

Airfoil aerodynamics

With the fundamentals of wind tunnels and instrumentation techniques established, the aerodynamic behaviour of an airfoil can now be considered. Since aerodynamic performance parameters, as well as the limitations in their measurement, originate from the flow behaviour around the airfoil, an understanding of the underlying aerodynamic principles is required.

This chapter provides a concise summary of airfoil aerodynamics. First, the fundamental mechanisms are reviewed in Appendix E.1, followed by the simplified inviscid description provided by potential flow theory in Appendix E.2. Appendix E.3 then considers the viscous region of the airfoil flow field. Finally, Appendix E.4 focuses on the aerodynamic effects introduced by boundary layer suction.

E.1. Fundamentals of Airfoil Aerodynamics

An airfoil is the cross-section of a wing or blade. The shape is designed such that, when moving through a fluid, the shape generates a desired aerodynamic force. The two single sources of which this force is the result are pressure distribution and shear stress distribution, respectively acting perpendicular and parallel to the airfoil surface as depicted in Figure E.1. [6]. Summing the contributions of these distributions results in the resultant force (R) acting on the airfoil. This resultant vector can be decomposed into the lift and drag forces, which are ultimately converted to aerodynamic coefficients following Equation C.13 and Equation C.14. A full overview of the forces and their origin is provided in Figure E.2.

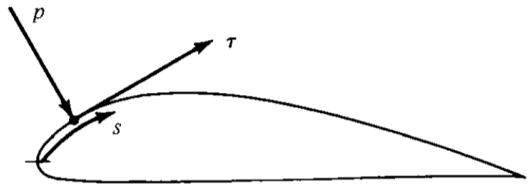


Figure E.1: Pressure and shear stress acting on an airfoil surface [6].

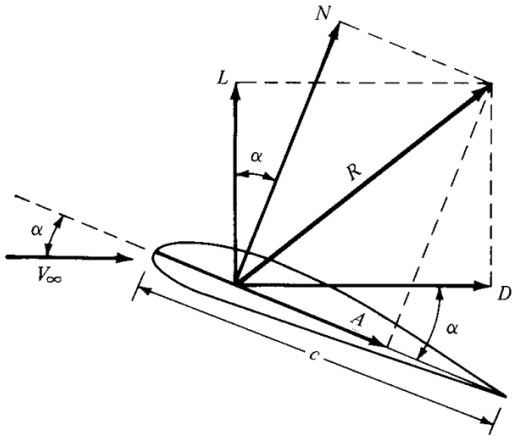


Figure E.2: Resultant aerodynamic force components acting on an airfoil [6].

Varying the angle of attack (α) results in a different pressure distribution due to a change in flow. Pres-

sure distributions are generally depicted using the pressure coefficient as defined in Equation E.1. Figure E.3 illustrates how the pressure distribution over the surface changes when α is varied.

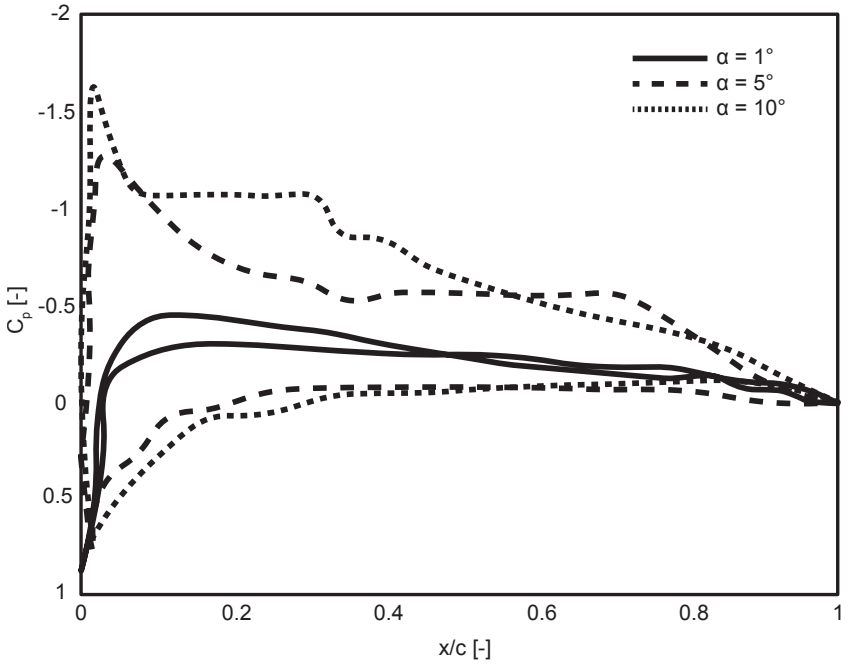


Figure E.3: Surface-pressure distributions for a NACA 0012 airfoil at $Re = 30{,}000$. Adapted from [45].

$$Cp = \frac{p - p_\infty}{\frac{1}{2}\rho V^2} \tag{E.1}$$

While the pressure coefficient distribution describes the local pressure variation over the airfoil surface, the total aerodynamic response is commonly expressed in terms of lift and drag coefficient curves. These curves show how the integrated pressure and shear stress contributions change with angle of attack. Typical lift and drag characteristics for a NACA airfoil are shown in Figure E.4.

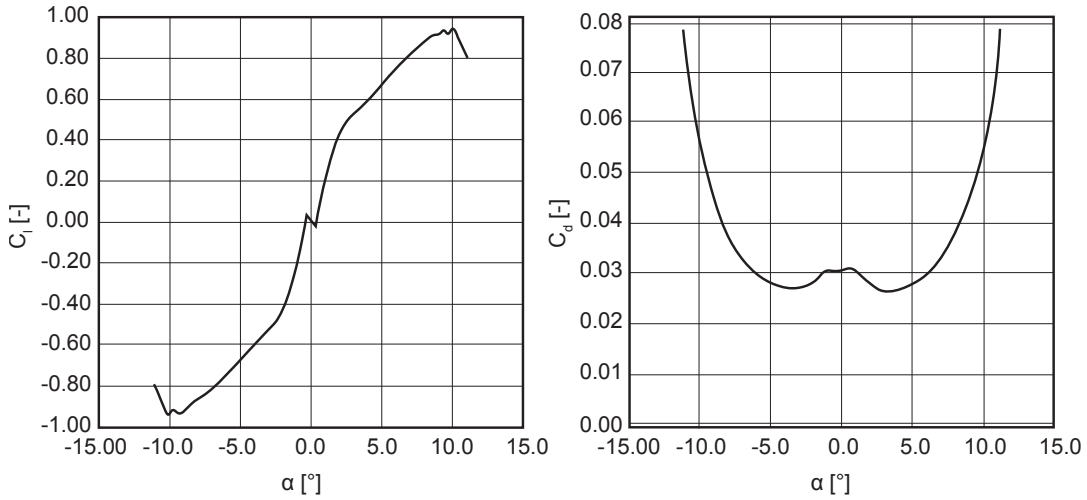


Figure E.4: XFOIL-predicted lift and drag coefficients for a NACA 0015 airfoil at $Re = 50{,}000$.

E.2. Potential Flow and Lift Generation

Potential flow provides the simplest framework for analysing the flow around an airfoil. The theory assumes the flow to be inviscid and incompressible, thereby neglecting viscous effects and density variations. Under these assumptions, the governing equations simplify considerably. Conservation of mass reduces to the incompressibility condition given in Equation E.2.

$$\nabla \cdot \mathbf{V} = 0 \tag{E.2}$$

For such a flow field, the velocity can be represented by a velocity potential, and Bernoulli's equation may be applied along any streamline. This relation, given in Equation E.3, links the local flow velocity to the pressure distribution and therefore forms the basis for explaining lift generation around an airfoil.

$$p + \frac{1}{2}\rho V^2 = const \tag{E.3}$$

When the flow is also irrotational as described by Equation E.4, Bernoulli's theory extends to the full flow field. In this case the flow can also be described by a single velocity potential (ϕ) that adheres to the governing equation for irrotational and incompressible flow, Laplace's equation (Equation E.5).

$$\nabla \times \mathbf{V} = 0 \tag{E.4}$$

$$\nabla^2 \phi = 0 \tag{E.5}$$

This velocity potential is a scalar function from which the velocity components in the flow field can be derived by taking its gradient as described by Equation E.6.

$$\mathbf{V} = \nabla \phi \tag{E.6}$$

Furthermore, potential flow theory allows the velocity field around a body to be represented as a superposition of elementary flow solutions, each satisfying Laplace's equation and the relevant boundary conditions. By combining a limited number of these basic flow types, semi-infinite bodies can be modelled. Four elementary flows are commonly distinguished, each described by a mathematical expression for its velocity potential. The corresponding streamline patterns are shown in Figure E.5.

Uniform flow. Uniform flow represents a constant velocity field in a single direction. For a flow purely in the x-direction, the corresponding velocity potential is given by Equation E.7. The associated streamline pattern is shown in Figure E.5a.

$$\phi = V_\infty x \tag{E.7}$$

Source and sink. A source represents flow emanating radially outward from a central point, while a sink describes the opposite behaviour. The velocity potential of a source is given by Equation E.8, where Λ denotes the source strength. A negative value of Λ corresponds to a sink, meaning velocity is directed towards the central point. The associated streamline pattern is shown in Figure E.5b. The flow has a one singularity point at its origin where the compressibility condition $\nabla \cdot V = 0$ is violated.

$$\phi = \frac{\Lambda}{2\pi} \ln r \tag{E.8}$$

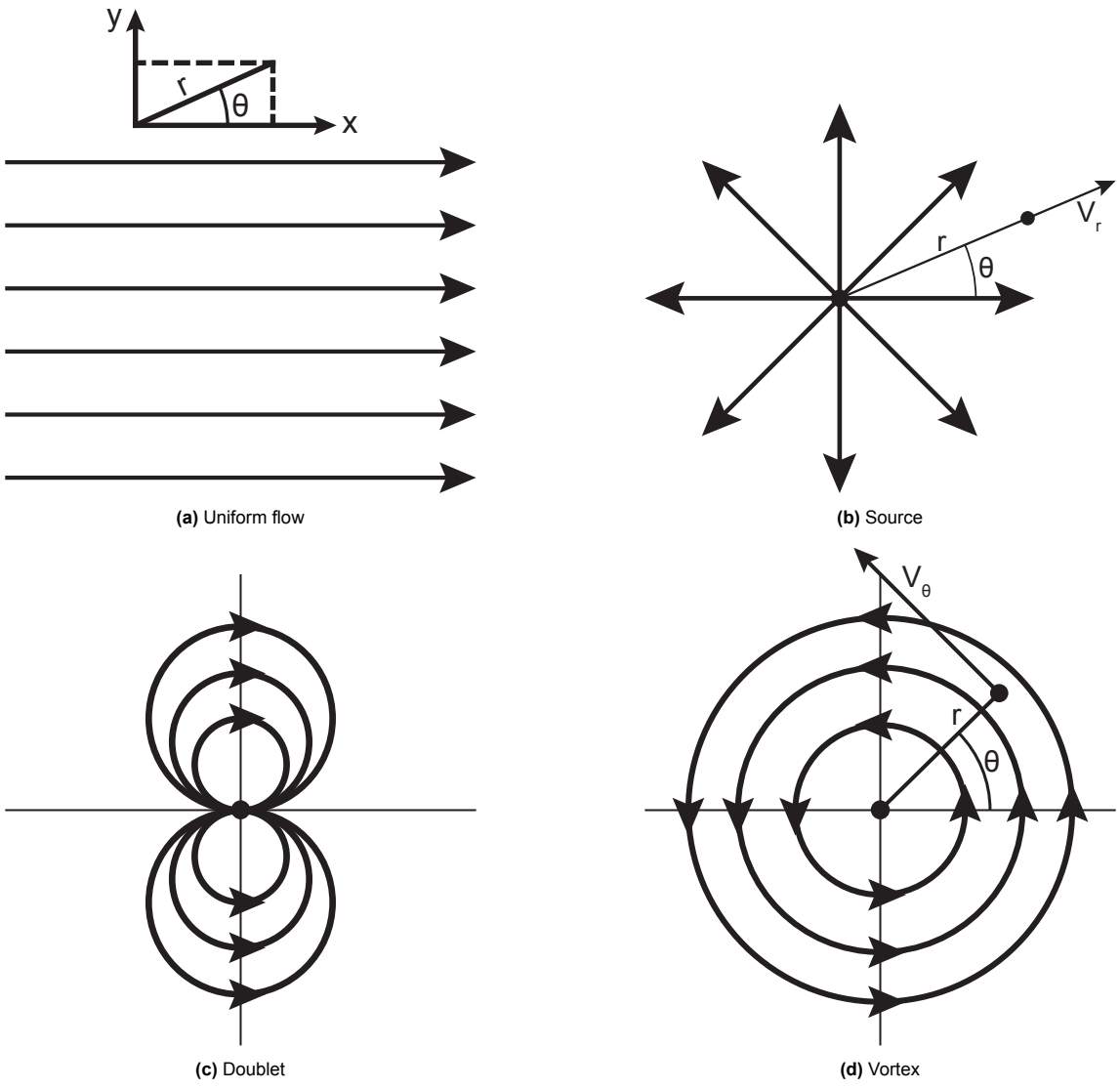
Doublet. A doublet is obtained by placing a source and sink of equal strength infinitely close together. The resulting singular flow field can be described by the velocity potential given in Equation E.9, where κ denotes the doublet strength. The associated streamline pattern is shown in Figure E.5c. The singularity regarding compressibility also holds here, just like for the source/sink flow.

$$\psi = -\frac{\kappa}{2\pi}\frac{\sin\theta}{r} \tag{E.9}$$

Vortex. A vortex represents rotational flow about a central point. Its velocity potential is given by Equation E.10, where Γ denotes the circulation strength. Positive values of Γ correspond to counter-clockwise rotation, while negative values correspond to clockwise rotation. The associated streamline pattern is shown in Figure E.5d.

Apart from the singularity at its centre, the vortex flow satisfies both the incompressibility and irrotationality conditions. At the origin, however, the velocity becomes singular, and the vorticity becomes infinitely large.

$$\phi = -\frac{\Gamma}{2\pi}\theta \tag{E.10}$$



(a) Uniform flow

(b) Source

(c) Doublet

(d) Vortex

Figure E.5: Elementary flows used in potential-flow theory.

The superposition of these elementary flows can be used to describe the potential flow around simple bodies. The flow around a rotating cylinder, a classic potential flow example, can, for instance, be simulated by superimposing a doublet and a vortex in uniform flow as shown in Figure E.6. [6] shows

that from this problem a key fluid dynamics relation can be obtained in the form of Equation E.11. This key aerodynamic relation, the Kutta-Joukowski theorem, shows that for potential flow the lift per unit span is directly related to the circulation around a body.

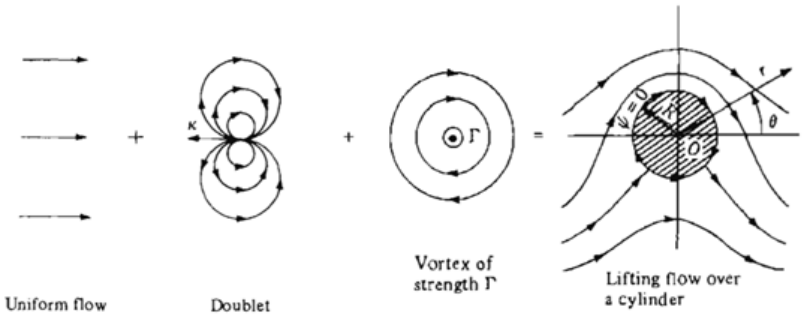


Figure E.6: Superposition of uniform flow, doublet flow, and vortex flow to obtain lifting flow over a circular cylinder [12].

$$L' = \rho_\infty V_\infty \Gamma_\infty \tag{E.11}$$

The theory can be extended to more complex geometries, such as airfoils, through thin airfoil theory. In this approach, the airfoil is represented by a bound vortex distribution along the chord, as depicted in Figure E.7. The strength of this vortex distribution $\gamma(x)$ is chosen such that the flow satisfies the no-penetration condition at the camber line and the Kutta condition at the trailing edge. The resulting circulation is then related to lift through the Kutta-Joukowski theorem. For a symmetric thin airfoil in attached, incompressible and inviscid flow, this results in the well-known linear relation between lift coefficient and angle of attack (Equation E.12).

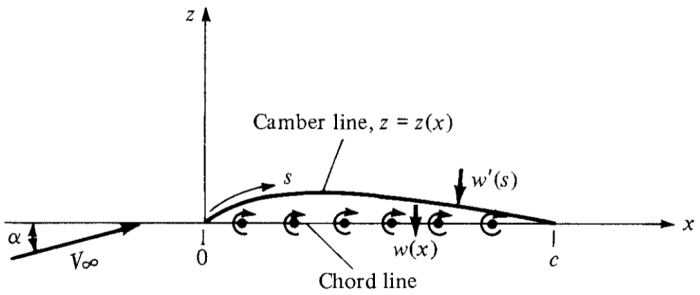


Figure E.7: Chord line vortex sheet [6]

$$C_l = 2\pi\alpha \tag{E.12}$$

where α is expressed in radians. Thin airfoil theory therefore provides a useful link between circulation, pressure difference, and lift generation. However, the theory is limited to thin airfoils at small angles of attack and attached-flow conditions. Viscous effects, boundary-layer growth, and flow separation are not captured.

Although potential flow theory provides a strong basis for describing the inviscid flow around airfoils, it does not capture all relevant flow phenomena. Appendix E.3 extends this theoretical framework by describing the viscous region of the flow field around an airfoil.

E.3. Boundary layer behaviour

Although the viscous region around an airfoil is relatively small, it has a substantial influence on the aerodynamic forces. This region, known as the boundary layer, is indicated by the grey region in Figure E.8. Within the boundary layer, viscosity plays an important role, particularly in the drag contribution. The fluid viscosity gives rise to skin-friction forces, which, together with the pressure forces, determine the total drag force. Despite the presence of viscous effects, Bernoulli's equation (Equation E.3) can still be used to determine the pressure forces at the airfoil surface, since the pressure is approximately constant along lines normal to the airfoil surface ($\frac{\delta p}{\delta y} = 0$).

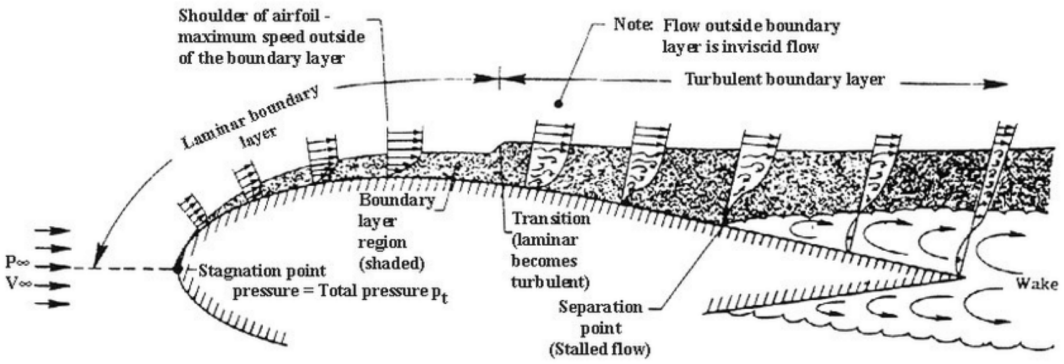


Figure E.8: Boundary layer propagation over an airfoil [31]

The boundary layer can be described by several parameters. The boundary layer thickness δ defines the distance from the surface to the inviscid region. A more mechanically interpretable measure to define this thickness is the displacement thickness introduced in [31], described by Equation E.13. It is a measure of the displacement of the streamlines outside the boundary layer due to the presence of the boundary layer. A third key parameter in boundary layer studies is the momentum thickness, expressed in Equation E.14. It describes the momentum flux deficit caused by the boundary layer relative to the undisturbed flow and therefore provides an indication of the boundary layer's susceptibility to separation. The shape factor is a parameter that combines both of these parameters and describes the fullness of the boundary layer by Equation E.15. Larger values indicate a less energetic near-wall region and are generally associated with an increased tendency toward separation.

$$\delta^*(x) = \int_0^\infty \left(1 - \frac{u}{U_\infty}\right) dy \tag{E.13}$$

$$\theta = \int_0^\infty \frac{u(y)}{U_\infty}\left(1 - \frac{u(y)}{U_\infty}\right) dy \tag{E.14}$$

$$H = \frac{\delta^*}{\theta}. \tag{E.15}$$

Another important boundary-layer quantity is the wall shear stress, which describes the tangential stress exerted by the flow on the airfoil surface. It is defined as

$$\tau_w = \mu \left.\frac{\partial u}{\partial y}\right|_{y=0} \tag{E.16}$$

where μ is the dynamic viscosity and $\partial u/\partial y$ is the velocity gradient normal to the wall. The wall shear stress is commonly expressed in non-dimensional form using the skin-friction coefficient,

$$C_f = \frac{\tau_w}{\frac{1}{2}\rho U_\infty^2}. \tag{E.17}$$

Wall shear stress is directly related to flow separation. Under an adverse pressure gradient, the near-wall velocity gradient decreases as the boundary layer loses momentum. Separation occurs when the wall shear stress becomes zero, corresponding to $C_f = 0$. Downstream of this point, reverse flow may occur close to the wall.

Within the boundary layer, different phenomena may occur. Generally, the boundary layer starts as laminar, growing in thickness along the airfoil. In some cases, the flow remains laminar along the full length of the body. In most cases, however, the flow transitions from laminar to turbulent, ultimately separating from the airfoil surfaces as illustrated in Figure E.8.

Transition. Transition occurs when the boundary layer changes from laminar to turbulent. It is often related to a critical local Reynolds number for a given geometry, although the exact transition location also depends on the pressure gradient, surface roughness, and free-stream turbulence intensity. If this critical value is known, the corresponding transition location x_{crit} can be estimated using Equation E.18. A turbulent boundary layer thickens faster than a laminar boundary layer because turbulent mixing increases momentum exchange within the boundary layer. As a result, high-momentum fluid from the outer part of the boundary layer is transported toward the wall, while low-momentum near-wall fluid is transported outward. Transition, including the associated velocity profiles, is depicted in Figure E.8.

$$Re_{x,crit} = \frac{\rho U_\infty x_{crit}}{\mu} \tag{E.18}$$

Separation. Separation occurs when the boundary layer is subjected to a sufficiently strong adverse pressure gradient. Figure E.3 shows the pressure distribution over an airfoil at different angles of attack. As the angle of attack increases, the pressure gradient over the upper surface becomes increasingly adverse, eventually causing the flow to separate as it can no longer overcome the rising pressure. Turbulent boundary layers are more resistant to separation, as momentum is transported toward the wall by turbulent mixing, energizing the near-wall flow. This is illustrated in Figure E.8, which shows separation in a turbulent boundary layer. Flow separation reduces pressure recovery over the aft portion of the airfoil, leading to a substantial increase in pressure drag. Therefore, maintaining attached flow is essential. As the angle of attack increases, separation occurs progressively earlier along the chord, ultimately leading to stall. At stall, the lift coefficient drops sharply.

High angles of attack are required to obtain high lift values. However, this also promotes flow separation, which increases drag and can ultimately lead to stall. Boundary layer suction offers a solution to this problem and is discussed further in Appendix E.4.

E.4. Boundary layer suction

Boundary layer suction (BLS) is one way of actively controlling boundary layer flow by removing low-momentum fluid from the near-wall region through slots in the surface. The principle was already demonstrated in Prandtl's boundary-layer work [27] and is further discussed in [19]. Suction can be used for laminar flow control by delaying transition, but in the present context, it is mainly considered as a separation-control method. Figure E.9 illustrates how BLS favourably alters the boundary layer velocity profile.

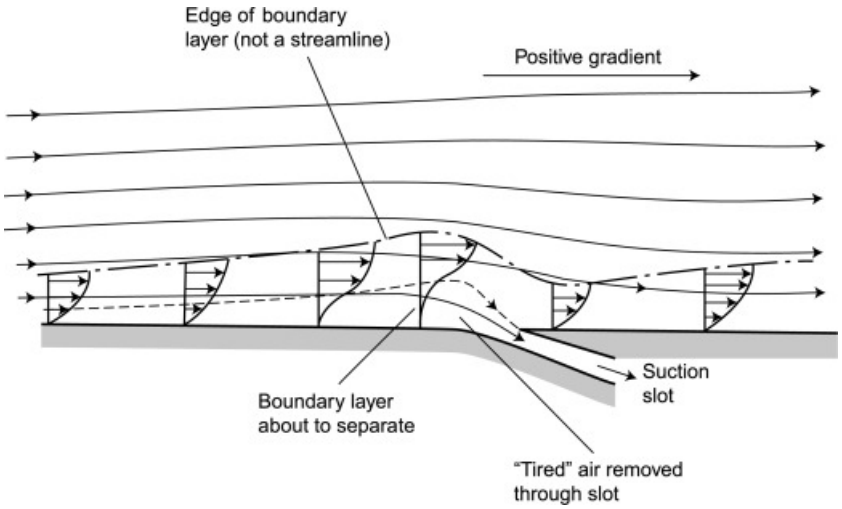


Figure E.9: Impact of BLS on boundary layer velocity profile [19]

By delaying flow separation, higher angles of attack can be reached before stall occurs, resulting in higher maximum lift values. A study performed on a NACA0012 deploying boundary suction [46] illustrates this in Figure E.10. For varying suction lengths and suction coefficients, the improvement in stall behaviour can be observed. Boundary layer suction can also reduce drag by suppressing or minimising laminar separation bubbles. For optimal performance, the suction location should be selected such that low-momentum fluid is removed shortly upstream of the separation point that would occur without suction.

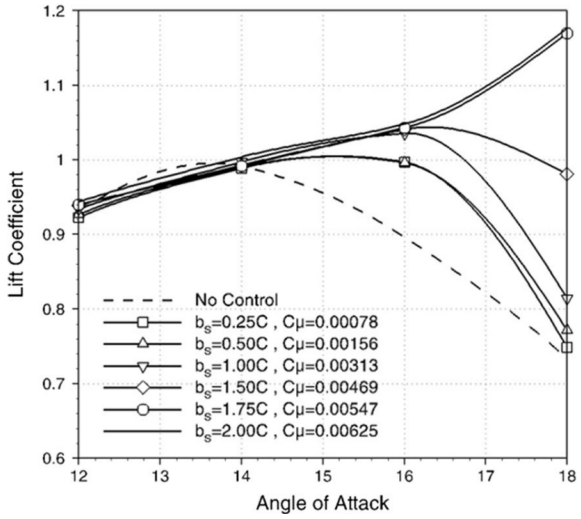


Figure E.10: Effect of suction on stall behaviour of a NACA0012 for different suction lengths [46]

A similar separation-control effect can be obtained by injecting air in the flow direction, which also increases the momentum of the boundary layer close to the surface.

The strength of suction is commonly expressed using a non-dimensional suction coefficient. For distributed suction over a defined suction surface, the coefficient can be written as in Equation E.19.

$$C_q = \frac{v_s}{U_\infty} = \frac{Q}{U_\infty S_{suc}}, \tag{E.19}$$

where v_s is the suction velocity normal to the surface, Q is the extracted volumetric flow rate, and S_{suc}

is the suction surface area. This definition describes the suction intensity relative to the external flow passing over the suction region.

Alternatively, a global suction coefficient can be defined using the total airfoil surface area following Equation E.20

$$C_q = \frac{Q}{U_\infty S}, \tag{E.20}$$

Here, S is the total reference surface area of the airfoil. Increasing the suction coefficient generally removes more low-momentum fluid from the near-wall region, therefore reducing displacement and momentum thickness, but also increases required suction power.